eman ta zabal zazu

Universidad del País Vasco

Euskal Herriko Unibertsitatea

Ab initio study of hydrogen based superconducting compounds at ambient pressure

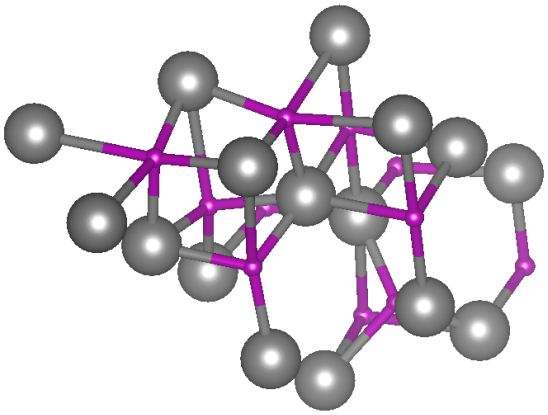

A thesis submitted to the
University of the Basque Country
to obtain the degree of
Doctor in Physics
by

Antonella Meninno

Supervisor: Dr. Ion Errea

To Salvatore

Contents

Resumen

La superconductividad es un fenómeno que ha sido uno de los principales temas de estudio en la física moderna. Es un fenómeno puramente cuántico, sin análogo en la física clásica, y en su interpretación más simple se caracteriza por una transición de fase en la que la resistencia de un material desaparece abruptamente bajo una temperatura crítica dependiente del material.

El desafío moderno en superconductividad (especialmente para aplicaciones prácticas) es encontrar ejemplos de superconductividad a alta temperatura. Un enfoque para aumentar la temperatura crítica superconductora a valores comparables con la temperatura ambiente es aumentar las presiones. Como ejemplos, en 2014 y 2015 se encontró que el H_3S a una presión de 155 GPa es superconductor a 203 K [Drozdov et al., 2015], y a 150 GPa el LaH_{10} se vuelve superconductor a 250 K [Drozdov et al., 2019, Somayazulu et al., 2019]. Desafortunadamente, las altas presiones requeridas para las altas temperaturas hacen que las aplicaciones prácticas de esos superconductores sean imposibles.

En esta tesis, nos enfocamos en estudiar candidatos a superconductividad a presión ambiental a altas temperaturas. Buscaremos candidatos entre los compuestos a base de hidrógeno, debido a observaciones recientes de superconductores en la clase de hidruros. Algunos ejemplos de tales "superhidruros" son los ya citados H_3S, con una T_c máxima de 203 K a 155 GPa y LaH_{10}, con $T_c = 250$ K a 150 GPa ; YH_9 [Snider et al., 2021, Kong et al., 2021], alcanzando una T_c al alrededor de 250 K a aproximadamente 200 GPa; y YH_6 [Kong et al., 2021, Semenok et al., 2020], con $T_c = 224$ K a 166 GPa. El desafío real es reducir la presión a la que se produce la superconductividad en los superhidruros, con el objetivo final de comprender si es posible una superconductividad a T_c alta y presión ambiental para este tipo de compuestos. Nos centraremos en materiales que pueden sintetizarse

y estudiarse experimentalmente y exploraremos los efectos de la dimensionalidad del sistema en el comportamiento superconductor.

El primer sistema que estudiamos es el hidruro de paladio (PdH). Este sistema es tridimensional y los átomos de paladio se organizan en una red cúbica centrada en las caras, en la que los átomos de hidrógeno pueden estar en una posición octaédrica o tetraédrica. La configuración energéticamente favorable es la completamente octaédrica (donde todos los hidrógenos están en configuraciones octaédricas) y en esta configuración tenemos $T_c = 9K$ [Worsham Jr et al., 1957, Errea et al., 2013, Rowe et al., 1974, Rowe et al., 1986, Kolesnikov et al., 1991, Sherman et al., 1977, Ross et al., 1998, Chowdhury and Ross, 1973]. En [Syed et al., 2016], el compuesto se estudió experimentalmente y se encontró una temperatura crítica al alrededor de 50 K a presión atmosferica con el compuesto en un estado metaestable. Nuestro objetivo es estudiar estados metaestables y reproducir este resultado computacionalmente. Nosotros investigamos la metaestabilidad de otras configuraciones, la mixta (donde los hidrógenos están en posiciones octaédricas y tetraédricas, con números variables) y la cual donde todos los atomos están en configuración tetraédrica. Todas esas configuraciones diferentes tienen diferentes propiedades superconductoras, que clasificamos en nuestro estudio. Abordamos el sistema usando técnicas que pueden incluir efectos anarmónicos, que han sido muy importantes en la literatura para predecir propiedades como el efecto isotópico inverso en este sistema [Eichler et al., 1975, Yussouff et al., 1995, Errea et al., 2013, Belov et al., 2015]. Este es nuestro proyecto más intensivo desde el punto de vista computacional, por lo que seleccionaremos un conjunto de estructuras para estudiarlas en profundidad y calcular la temperatura crítica.

Hemos demostrado con éxito la existencia de configuraciones metaestables, en las que los átomos de hidrógeno también pueden ocupar posiciones tetraédricas. También hemos subrayado la importancia de los efectos anarmónicos y cuánticos en la estabilización de esas estructuras. Este resultado enriquece las posibilidades de estudio de este compuesto, ya que se pueden analizar configuraciones diferentes al octaédrico completo desde una perspectiva teórica y experimental. Hemos analizado el efecto de esta variación en la ocupación sobre la temperatura crítica, mostrando que las estructuras con una configuración completamente octaédrica completa favorecen la superconductividad, y la ocupación tetraédrica la suprime. El compuesto con ocupación octaédrica presenta fonones menos enrgéticos con respecto a los compuestos que también tienen ocupación tetraédrica, y este es un

factor que contribuye a que la ocupación octaédrica mejore la temperatura crítica de superconductividad. En última instancia, la ausencia de superconductividad a alta temperatura puede explicarse por el débil carácter de hidrógeno de la densidad de estados en el nivel de Fermi. En el futuro, seguramente será interesante analizar más estructuras con configuraciones variadas.

El segundo sistema que analizamos es el boruro de hidrógeno (HB). Este sistema bidimensional es un superconductor prometedor debido a que su estructura es similar a la de MgB_2 (a partir del cual se puede sintetizar [Nishino et al., 2017]), en si mismo un superconductor de alta temperatura [Nagamatsu et al., 2001]. Nos centramos en HB debido al hecho de que se puede sintetizar, por lo que es un buen candidato para la verificación experimental de nuestros resultados. Los materiales 2D, en general, son más simples de estudiar computacionalmente que los materiales 3D, y HB proporciona un candidato ideal para el estudio, debido a su disponibilidad para fines experimentales. El procedimiento de hidrogenación mejora considerablemente la superconductividad mediada por fonones en muchos sistemas [Bekaert et al., 2019, Savini et al., 2010], por lo que este compuesto es un buen candidato para la superconductividad a alta temperatura a presión ambiental [Tateishi et al., 2019]. En HB, podemos estudiar el rol del hidrógeno en la superconductividad mediada por fonones, la importancia de la superficie de Fermi en el cálculo de la temperatura crítica y también explorar los efectos del dopaje por adición de electrones o campos eléctricos externos.

Hemos encontrado que, contrariamente a lo esperado, ni el boruro de hidrógeno no dopado ni el dopado muestran superconductividad a alta temperatura. Hemos explicado este resultado analizando el carácter de las bandas en el nivel de Fermi, mostrando que hay un carácter predominante de boro. El hidrógeno trabaja contra el acoplamiento electrón-fonón de los modos de boro, suprimiendo una importante contribución a la superconductividad. Hemos mostrando además que la baja concentración de hidrógeno en el nivel de Fermi es responsable de la ausencia de superconductividad. Como hemos estudiado exclusivamente la fase $Cmmm$, será importante para el futuro de este compuesto estudiar las propiedades superconductoras de otras fases.

Por último, estudiamos una cadena unidimensional de nueve anillos bencénicos, el nonaceno. Se ha descubierto que los compuestos orgánicos son buenos candidatos para la superconductividad a alta temperatura a presión ambiental [Kivelson and Chapman, 1983, Casula et al., 2011]. En los compuestos orgánicos podemos tener

dos mediadores para la superconductividad: el acoplamiento estándar de electrones y fonones y el ordenamiento magnético, y el estado fundamental del compuesto debe describirse con gran precisión antes de intentar distinguir entre los dos tipos de superconductividad. El nonaceno es un compuesto orgánico, en el que aún no está claro si la superconductividad está mediada por el acoplamiento electrón-fonón o por ordenamiento magnético. La principal dificultad en este estudio es la cuasi-degeneración del estado fundamental y el primer estado excitado: se requieren cálculos muy precisos para describir las propiedades del estado fundamental. Nuestro objetivo es calcular la función de onda y la energía del estado fundamental con una precisión que nos permita distinguir entre el estado fundamental y el primer estado excitado, y clasificar así sus propiedades.

Hemos construido una función de onda que describe el estado fundamental con una buena precisión, mostrando que los resultados obtenidos con una función de onda antiferromagnética JSD están muy cerca de los resultados obtenidos con una función de onda JPfaffiana. Esto implica que la cadena de nueve anillos tiene un comportamiento antiferromagnético. La presencia de magnetismo puede ser relevante en la superconductividad, ya que puede generar una superconductividad impulsada por la fluctuación de espín. Como la molécula de benceno tiene un comportamiento paramagnético, una posible dirección futura sería estudiar el comportamiento magnético de las cadenas intermedias, buscando un punto en el que este comportamiento cambie de paramagnético a antiferromagnético.

De nuestro trabajo, podemos sacar algunas conclusiones generales. El análisis de hidruro de paladio y boruro de hidrógeno muestra que se necesita un fuerte carácter de hidrógeno en las bandas en el nivel de Fermi para tener una temperatura crítica alta, una característica que no está presente en nuestros sistemas. También podemos señalar que los hidruros metálicos con átomos de H en los sitios intersticiales que hemos estudiado no son muy prometedores para la superconductividad a alta temperatura.

Los fonones de baja energía mejoran la temperatura crítica en este tipo de compuestos. Hemos tratado de crear las de condiciones para los fonones blandos estudiando y cambiando las características de nuestros sistemas. En particular, para el hidruro de paladio hemos modificado la posición de los átomos de hidrógeno, mientras que para el boruro de hidrógeno hemos usado dopaje, pero se podrían usar otros medios para lograr este fin.

El trabajo realizado en esta tesis es una contribución a la comprensión del rol del hidrógeno en la superconductividad, y constituye una base para futuros trabajos que amplíen los resultados obtenidos. El objetivo de nuestro trabajo es estudiar sistemas que sean capaces de alcanzar superconductividad a alta temperatura a presión ambiental. Los compuestos que hemos estudiado no tienen esta propiedad. Sin embargo, nuestros resultados pueden usarse para comprender qué factores son importantes para la superconductividad a alta temperatura y qué factores son perjudiciales para ella. Si bien no logramos obtener todos los resultados que esperábamos, debemos tener en cuenta que este es un campo muy desafiante, pero es un campo que vale la pena estudiar, ya que podría tener una enorme repercusión tanto desde el punto de vista científico como tecnológico.

Introduction

Superconductivity is a phenomenon that has been one of the main topics of study in modern physics. It is a purely quantum phenomenon, with no analogue in classical physics, and in its simplest interpretation is characterized by a phase transition in which the resistance of a material abruptly vanishes under a material-dependent critical temperature.

Historically, superconductivity was first observed in 1911 by Heike Kamerlingh Onnes, who observed the vanishing of the electrical resistance of mercury when its temperature dropped under 4.2 K. This discovery was followed by other examples of superconductive materials, with lead transitioning to a superconducting phase under 7 K (discovered in 1913) and niobium nitride under 16 K (discovered in 1941)*. In 1933, a breakthrough in the study of superconductivity happened with the discovery of the Meissner effect [Meissner and Ochsenfeld, 1933], which consists in the expulsion of magnetic lines by a superconductor once the critical temperature for superconductivity is reached. The Meissner effect was further studied in [London and London, 1935]. In this study a model was proposed to explain the exponential decay of a magnetic field inside the superconductor, where the internal magnetization shields the interior of a superconductor from an external magnetic field, provided that the external field is not too strong. In particular, the effect is distinguished from a theoretical material of infinite conductivity, as in the Meissner effect the magnetic field is properly expelled during the superconductive transition. One of the most famous examples of this effect is the experiment in which a stationary magnet is put over a superconductor not in the superconducting phase, and then the superconductor is cooled under the critical temperature: the expulsion of magnetic lines from the superconductor causes the stationary magnet to levitate.

*For a more complete history of superconductivity, we refer to [Van Delft and Kes, 2010].

From the theoretical point of view, the first major step towards an understanding of superconductivity came in 1950 from the phenomenological Ginzburg-Landau model [Landau and Ginzburg, 1950], combining the theory of second-order phase transitions with a non linear Schrödinger-like wave function equation to study various properties of superconducting systems. In the same period, in [Maxwell, 1950] and [Reynolds et al., 1950] a relation between the critical temperature and the isotopic mass was found, pointing to the importance of electron-phonon interactions in the description of superconductivity. A complete microscopic theory of superconductivity came in 1957 with the BCS model [Bardeen et al., 1957], where the superconducting currents were described as a superfluid of pairs of electrons interacting through phonon exchange (Cooper pairs). Notably, the Ginzburg-Landau model could be recovered from the BCS model near the critical temperature [Gor'kov, 1959]. Further advancements in computing the critical temperature of superconducting materials came in the empirical McMillan formula [McMillan, 1968] and in the description of superconductivity through a Green-function based approach in the Migdal-Eliashberg theory [Migdal, 1958, Eliashberg, 1960].

The modern challenge in superconductivity (especially for practical applications) is to find examples of high-temperature superconductivity. An approach to increase the superconducting critical temperature to values comparable with room temperature is to increase pressures. As examples, in 2014 and 2015 it was found that H_3S at a pressure of 155 GPa is superconductive at 203 K [Drozdov et al., 2015], and at 150 GPa LaH_{10} becomes superconductive at 250 K [Drozdov et al., 2019, Somayazulu et al., 2019]. Unfortunately, the high pressures required for those high temperatures make practical applications of those superconductors impossible.

In this thesis, we focus on studying candidates for ambient pressure superconductivity at high temperatures. We will look for candidates among hydrogen-based compounds, due to recent observations of superconductors in the class of hydrides. Some examples of such "superhydrides" are the already cited H_3S, with a maximum T_c of 203 K at 155 GPa and LaH_{10}, with $T_c = 250$ K at 150 GPa; YH_9 [Snider et al., 2021,Kong et al., 2021], reaching a T_c of around 250 K at approximately 200 GPa; and YH_6 [Kong et al., 2021, Semenok et al., 2020], with $T_c = 224$ K at 166 GPa. The actual challenge is to reduce the pressure at which superconductivity occurs in superhydrides, with the ultimate goal of understanding if high-T_c super-

conductivity is possible at ambient pressure for this type of compounds. We will focus on materials that can be synthesised and studied experimentally, and explore the effects of dimensionality of the system on the superconductive behaviour.

The first system that we study is palladium hydride (PdH). PdH is a three-dimensional system in which the palladium atoms arrange in a face-centred cubic (fcc) lattice, in which hydrogen atoms can be in an octahedral or tetrahedral position, according to the number of nearest Pd neighbours. The favourite configuration is the octahedral one (where all hydrogens are in octahedral configurations), and in its configuration we have $T_c = 9K$ [Worsham Jr et al., 1957, Errea et al., 2013, Rowe et al., 1974, Rowe et al., 1986, Kolesnikov et al., 1991, Sherman et al., 1977, Ross et al., 1998, Chowdhury and Ross, 1973]. In [Syed et al., 2016] the compound was studied experimentally, and a critical temperature of circa 50 K was found at ambient pressure with the compound in a metastable state. Our goal is to study metastable states and reproduce this result computationally. We investigate the metastability of other mixed configurations (where hydrogens are either in octahedral of tetrahedral positions, with varying numbers). Those different configurations all have different superconductive properties, that we classify in our study. We approach the system using techniques that can include anharmonic effects, that have been very important in literature to predict properties like the inverse isotope effect in this system [Eichler et al., 1975, Yussouff et al., 1995, Errea et al., 2013, Belov et al., 2015]. This is our most computationally intensive project, so we will select a set of structures to study in depth and compute their expected critical temperatures due to the electron-phonon coupling.

The second system that we analyse is hydrogen boride (HB). This two dimensional system is a promising superconductor due to its relation and similar structure to MgB_2 (from which it can be synthesised [Nishino et al., 2017]), which is a high temperature superconductor [Nagamatsu et al., 2001]. We focus on HB due to the fact that it can be synthesised, so it is a good candidate for experimental verification of our results. General 2D materials are simpler to study computationally than 3D materials, and HB provides an ideal candidate for study, due to its availability for experimental purposes. The procedure of hydrogenation strongly enhances phonon-mediated superconductivity [Bekaert et al., 2019, Savini et al., 2010], so this compound is a good candidate for high temperature superconductivity at ambient pressure [Tateishi et al., 2019]. In HB, we can study the role of hydrogen in phonon-mediated superconductivity, the importance of the Fermi

surface in computing the critical temperature and also explore the effects of doping by electron addition or external electric fields.

Lastly, we study a one-dimensional chain of nine benzene rings, the nonacene. Organic compounds have been found to be good candidates for high temperature superconductivity at ambient pressure [Kivelson and Chapman, 1983, Casula et al., 2011]. In organic compounds we can have two mediators for superconductivity: standard electron-phonon coupling and magnetic ordering, and the ground state of the compound has to be described with high precision before attempting to distinguish between the two types of superconductivity. Nonacene is an organic compound, in which it is not yet clear if superconductivity is mediated by electron-phonon coupling or magnetic ordering. The main difficulty in this study is the quasi-degeneracy of the ground state and first excited state: very precise computations are required in order to describe the properties of the ground state accurately. Our goal is to compute the ground state wave function and energy to a precision that allows us to distinguish between the ground state and the first excited state, and classify its properties.

The thesis is organised as follows. Chapter 1 introduces the fundamental theory that we use to describe the interactions between electrons and ions in the crystal, where we review well-established methods like the Born-Oppenheimer approximation, the study of electrons via the Kohn-Sham equations, the theory of phonons and interactions between electrons and phonons, and how they contribute to the computation of the critical temperature for superconductivity. Chapter 2 reviews the stochastic methods that we use for computing electronic and vibrational properties of the systems at an advanced level, needed for some of the applications in the thesis, describing the applications of Quantum Monte Carlo methods, the principles that we use to choose trial wave functions, and the Stochastic Self-Consistent Harmonic Approximation (SSCHA) method that we use to include anharmonic effects. Chapters 3, 4, 5 describe the study of the systems that we have introduced, and then we end the thesis with our conclusions and remarks for future directions of research.

Chapter 1

Fundamental theory of electrons and ions in crystals

The goal of this chapter is to introduce the problem of the interaction between ions and electrons in a crystal. In crystals, as a first approximation, electrons move in periodic potentials, giving rise to energy bands that they occupy. Beyond this approximation, the crystal structure itself can vibrate, and the modes of these vibrations are denoted as phonons. The system of electrons and ions can then be described through a system of particles, electrons in energy bands and phonons, together with their interactions. The Born-Oppenheimer theory provides an excellent framework to describe this system.

In this chapter, we will start by describing the Born-Oppenheimer approximation as a basis for the rest of the chapter. The next step will be introducing the various tools that are used to deal with the electronic problem, as density functional theory and pseudopotentials. Next, we will examine the other half of the problem, the problem of the vibrations of the ions forming the crystal. We will see how this gives rise to a phonon system, and introduce the tool of density functional perturbation theory that can be used to make phonon computations feasible. Lastly, we will describe interactions between electrons and phonons, and why going beyond the harmonic level can be very important in the work of this thesis.

1.1 Born-Oppenheimer approximation

The Born-Oppenheimer approximation [Born and Heisenberg, 1985] is fundamental in modern condensed matter physics. The goal of this approximation is to describe the motion of a system of electrons and ions, using as the approximation parameter the ratio between the mass of the electrons and the ions, which is small (10^{-4} for the hydrogen atom). The Hamiltonian for the problem is

$$\begin{aligned} H =& \sum_{i=1}^{N_e} \frac{\boldsymbol{p}_i^2}{2} + \sum_{I=1}^{N_{ion}} \frac{\boldsymbol{P}_I^2}{2M_I} - \sum_{i,I=1}^{N_e,N_{ion}} \frac{Z_I}{|\boldsymbol{r}_i - \boldsymbol{R}_I|} + \\ &+ \frac{1}{2} \sum_{i,j=1,i\neq j}^{N_e} \frac{1}{|\boldsymbol{r}_i - \boldsymbol{r}_j|} + \frac{1}{2} \sum_{I,J=1,I\neq J}^{N_{ion}} \frac{Z_I Z_J}{|\boldsymbol{R}_I - \boldsymbol{R}_J|}, \end{aligned} \tag{1.1.1}$$

where M_I are the masses of the ions, Z_I are their charges, N_e and N_{ion} indicate respectively the number of electrons and ions in the system. The first two terms are the kinetic terms for electrons and ions (with $\boldsymbol{p}_i$ the electron momenta and $\boldsymbol{P}_I$ the ions momenta), the third term is the Coulomb attraction between the electrons at positions $\boldsymbol{r}_i$ and the ions at positions $\boldsymbol{R}_I$, while the last two terms are the Coulomb repulsion between electrons and the repulsion between ions. We are using atomic units in which $m = e = \hbar = 4\pi\epsilon_0 = k_B = 1$ (where m and e are the electron mass and charge). In this context, we write a standard wavefunction as

$$\psi(\boldsymbol{r}, \boldsymbol{R}) = \langle \boldsymbol{r}, \boldsymbol{R} | \psi \rangle \,, \tag{1.1.2}$$

where $\boldsymbol{R}$ collectively indicates all the ionic coordinates $\boldsymbol{R}_I$ and $\boldsymbol{r}$ collectively indicates all the electron coordinates $\boldsymbol{r}_i$.

In the Hamiltonian (1.1.1) we can immediately see an appropriate parameter for expansion. As stated, due to the difference of mass between the lightest ion and the electron, we can always take m/M_I to be very small. At zero order in those parameters, we can assume that the ions are fixed in $\boldsymbol{R}$, positions that can be taken as parameters. We can then solve the electronic problem with the ions fixed:

$$H_{el} = \sum_{i=1}^{N_e} \frac{\boldsymbol{p}_i^2}{2} + \frac{1}{2} \sum_{i,j=1,i\neq j}^{N_e} \frac{1}{|\boldsymbol{r}_i - \boldsymbol{r}_j|} - \sum_{i,I=1}^{N_e,N_{ion}} \frac{Z_I}{|\boldsymbol{r}_i - \boldsymbol{R}_I|} + \frac{1}{2} \sum_{I,J=1,I\neq J}^{N_{ion}} \frac{Z_I Z_J}{|\boldsymbol{R}_I - \boldsymbol{R}_J|}. \tag{1.1.3}$$

H_{el} contains the kinetic terms for electrons, the ion-electron interactions (that affect the motion of both ions and electrons, but due to the mass difference the electrons are more affected by this potential) and the interactions between ions, which at this level of approximation are constant. The energy levels of the electron problem are defined as the eigenvalues of the operator H_{el}:

$$H_{el}\psi_\alpha^{el}(\boldsymbol{r},\boldsymbol{R}) = E_\alpha^{el}(\boldsymbol{R})\psi_\alpha^{el}(\boldsymbol{r},\boldsymbol{R}). \tag{1.1.4}$$

Here $E_\alpha^{el}(\boldsymbol{R})$ are the energy levels of the electronic Hamiltonian, indexed by α, depending on the ions positions $\boldsymbol{R}$ parametrically, and ψ_α^{el} are the corresponding wavefunctions. The Born-Oppenheimer approximation consists in approximating the wavefunctions for the original Hamiltonian H as

$$\Psi_{\alpha\beta}(\boldsymbol{r},\boldsymbol{R}) = \chi_\beta(\boldsymbol{R})\psi_\alpha^{el}(\boldsymbol{r},\boldsymbol{R}), \tag{1.1.5}$$

where χ_β acts as a wavefunction for the ionic part only. In this approximation the electronic wavefunctions are determined independently of the ionic wavefunctions (apart from the dependency on $\boldsymbol{R}$, taken as parameters). The next step is now to understand how to determine appropriate energy levels for the ionic problem.

Consider the action of the Hamiltonian operator H on the wavefunction $\Psi_{\alpha\beta}(\boldsymbol{r},\boldsymbol{R})$. The first step is to integrate out the electron coordinates and write an eigenvalue equation in terms of the eigenvalues $E_{\alpha\beta}$, which are the eigenvalues of the full Hamiltonian (1.1.1):

$$\begin{aligned}&\int \mathrm{d}\boldsymbol{r}\ (\psi_\alpha^{el})^*(\boldsymbol{r},\boldsymbol{R})H\psi_\alpha^{el}(\boldsymbol{r},\boldsymbol{R})\chi_\beta(\boldsymbol{R}) = \\ &= \left(\sum_{I=1}^{N_{ion}} \frac{\boldsymbol{P}_I^2}{2M_I} + E_\alpha^{el}(\boldsymbol{R}) + \Delta H_\alpha\right)\chi_\beta(\boldsymbol{R}) = E_{\alpha\beta}\chi_\beta(\boldsymbol{R}).\end{aligned} \tag{1.1.6}$$

Here we have defined the operator ΔH_α as

$$\begin{aligned}\Delta H_\alpha =& \sum_{I=1}^{N_{ion}} \frac{1}{2M_I}\int \mathrm{d}\boldsymbol{r}\ (\psi_\alpha^{el}(\boldsymbol{r},\boldsymbol{R}))^*\boldsymbol{P}_I^2\psi_\alpha^{el}(\boldsymbol{r},\boldsymbol{R}) + \\ &+ \sum_{I=1}^{N_{ion}} \frac{1}{M_I}\int \mathrm{d}\boldsymbol{r}\ (\psi_\alpha^{el}(\boldsymbol{r},\boldsymbol{R}))^*\boldsymbol{P}_I\psi_\alpha^{el}(\boldsymbol{r},\boldsymbol{R})\boldsymbol{P}_I.\end{aligned} \tag{1.1.7}$$

This operator comes from acting with the kinetic term of the ions on the electronic part of the wavefunction: the first part of the sum is an operator proportional to identity, while the second part is an operator proportional to $\boldsymbol{P}_I$.

The term ΔH_α is the term that can be shown to be negligible with respect to the other terms [Grimwall, 1980]. An usual simplification is the adiabatic approximation, where we drop the α term from the electron energy and we use the ground state instead, as we can assume the ionic fluctuations do not excite electron states [Grimwall, 1980]. This allows us to completely decouple the ionic and electronic Hamiltonian: the wavefunction $\chi_\beta(\boldsymbol{R})$ will be determined by the eigenvalue equation

$$\left(\sum_{I=1}^{N_{ion}} \frac{\boldsymbol{P}_I^2}{2M_I} + E^{el}(\boldsymbol{R})\right) \chi_\beta(\boldsymbol{R}) = E_\beta \chi_\beta(\boldsymbol{R}), \tag{1.1.8}$$

where all dependency on the particular electron state has been dropped. We have finally obtained a prescription to get both the electronic part (that is solved through electronic band theory) and the ionic part (using the approximation procedure we described) for the approximate wavefunction. It is convenient to define

$$H_{ion,BO} = \sum_{I=1}^{N_{ion}} \frac{\boldsymbol{P}_I^2}{2M_I} + E^{el}(\boldsymbol{R}) : \tag{1.1.9}$$

here we see that the eigenvalues $E^{el}(\boldsymbol{R})$ of the electronic problem become the potential for the ionic problem. Due to this, $E^{el}(\boldsymbol{R})$ is usually called the Born-Oppenheimer potential.

The total eigenfunctions $\Psi_{\alpha\beta}(\boldsymbol{r}, \boldsymbol{R}) = \chi_\beta(\boldsymbol{R})\psi_\alpha^{el}(\boldsymbol{r}, \boldsymbol{R})$ will be an orthonormal set, with the product

$$\langle \Psi_{\alpha'\beta'} | \Psi_{\alpha\beta} \rangle = \delta_{\alpha\alpha'}\delta_{\beta\beta'}. \tag{1.1.10}$$

This procedure provides an excellent approximation for the scope of our work: in this framework, we can separate the electron and phonon problems and study their properties independently [Waller, 1956]. Nevertheless, the interaction Hamiltonian ΔH_α cannot be completely neglected. Its main contribution is to describe interactions between phonon and electron systems, and as we will see in the rest of this work, those will be crucial to understand the phenomenon of superconductivity mediated by the electron-phonon interaction.

1.2 The electronic problem

We have seen that the Born-Oppenheimer adiabatic approximation allows us to effectively decouple the electronic and ionic problems. Once this is done, the two problems can be studied separately. In this section, our goal is to explore the tools that can be used to solve the electronic problem.

There is a plethora of methods that can be used to attack the electronic problem (one of the most popular examples is the Hartree-Fock method). In this chapter, we will focus on describing the method of Density Functional Theory (DFT) while in chapter 2 we will describe Quantum Monte Carlo (QMC) methods. For an overview on the most popular methods, the reader can consult [Grosso and Parravicini, 2013].

1.2.1 Density functional theory

We first recall the form of the electronic Hamiltonian H_{el}:

$$H_{el} = \sum_{i=1}^{N_e} \frac{\boldsymbol{p}_i^2}{2} - \sum_{i,I=1}^{N_e,N_{ion}} \frac{Z_I}{|\boldsymbol{r}_i - \boldsymbol{R}_I|} + \frac{1}{2} \sum_{i,j=1,i\neq j}^{N_e} \frac{1}{|\boldsymbol{r}_i - \boldsymbol{r}_j|} + \frac{1}{2} \sum_{I,J=1,I\neq J}^{N_{ion}} \frac{Z_I Z_J}{|\boldsymbol{R}_I - \boldsymbol{R}_J|}. \tag{1.2.1}$$

As stated, the ions are fixed, so the last term is a constant. In the next computations we will omit this term, and reintroduce it at the end of the calculation.

Due to the adiabatic approximation, we can treat the ions positions $\boldsymbol{R}_I$ as fixed parameters: upon quantization, they will not become operators. The interaction potential is composed by two elements: the ion-electron interaction, that is convenient to write as

$$V_{el,ion} = -\sum_{i=1,I=1}^{N_e,N_{ion}} \frac{Z_I}{|\boldsymbol{r}_i - \boldsymbol{R}_I|} = \sum_{i=1}^{N_e} V_{ext}(\boldsymbol{r}_i), \tag{1.2.2}$$

and the electron-electron interaction

$$V_{el,el} = \frac{1}{2} \sum_{i,j=1,i\neq j}^{N_e} \frac{1}{|\boldsymbol{r}_i - \boldsymbol{r}_j|}. \tag{1.2.3}$$

The kinetic term and the electron-electron interaction constitute the internal part of the Hamiltonian, H_{int}, while the electron-ion term constitutes the external part V_{ext}, the potential under which the system of electrons moves.

Ideally, one would find an electron wavefunction $\psi^{el}(\boldsymbol{r}, \boldsymbol{R})$ for the ground state of the system (on which we focus from now on). In practice, such a wavefunction is very difficult to find. An alternative way is provided by the Hohenberg-Kohn theorem [Hohenberg and Kohn, 1964] stating that for non degenerate ground states (on which we focus) there exists a one-to-one correspondence between the ground state density (that we define shortly) of the system and the external potential V_{ext}. If we assume that the other terms are fixed, the external potential then fixes the Hamiltonian uniquely. This way, the object of study becomes the external potential, and variational principles can be written in order to compute it.

The ground state density can be computed from the ground state vector $\left|\psi^{el}_{\boldsymbol{R}}\right\rangle$*: it is defined as

$$n(\boldsymbol{x}, \boldsymbol{R}) = \left\langle \psi^{el}_{\boldsymbol{R}} \right| \sum_{i=1}^{N_e} \delta(\boldsymbol{x} - \boldsymbol{r}_i) \left| \psi^{el}_{\boldsymbol{R}} \right\rangle, \tag{1.2.4}$$

and depends on the space coordinate $\boldsymbol{x}$ and on the ion coordinates $\boldsymbol{R}$ as parameters. The ground state energy becomes then a functional of the ground state density. This allows us to make the identification

$$E^{el}[v_{ext}](\boldsymbol{R}) = \left\langle \psi^{el}_{\boldsymbol{R}} \right| H^{el} \left| \psi^{el}_{\boldsymbol{R}} \right\rangle \leftrightarrow E^{el}[n](\boldsymbol{R}). \tag{1.2.5}$$

In an obvious way, we can split the ground state energy into contributions from kinetic energy, electron-ion interaction and electron-electron interaction as

$$E^{el}[n](\boldsymbol{R}) = T[n](\boldsymbol{R}) + E_{el,el}[n](\boldsymbol{R}) + E_{el,ion}[n](\boldsymbol{R}). \tag{1.2.6}$$

This is the starting point for the DFT method.

The electron-ion energy functional can be written as

$$E_{el,ion}[n](\boldsymbol{R}) = \left\langle \psi^{el}_{\boldsymbol{R}} \right| V_{el,ion} \left| \psi^{el}_{\boldsymbol{R}} \right\rangle = \int \mathrm{d}\boldsymbol{x}\, n(\boldsymbol{x}, \boldsymbol{R}) V_{ext}(\boldsymbol{x}). \tag{1.2.7}$$

Unfortunately, the electron-electron interaction cannot be written in such a simple form, due to the fact that the interaction is made of two body interactions. In

*For clarity, in writing ket states in which $\boldsymbol{R}$ is a parameter we will place $\boldsymbol{R}$ in the subscript.

principle, the energy is given by

$$E_{el,el}[n](\boldsymbol{R}) = \left\langle \psi^{el}_{\boldsymbol{R}} \right| V_{el,el} \left| \psi^{el}_{\boldsymbol{R}} \right\rangle . \tag{1.2.8}$$

As stated, writing such a functional is hard. As an approximation, we can suppose that $\left|\psi^{el}_{\boldsymbol{R}}\right\rangle$ is made of a Slater determinant of single-particle wavefunctions: in this case, the energy would be[†]

$$E_H[n](\boldsymbol{R}) = \frac{1}{2}\int\int \mathrm{d}\boldsymbol{x}\mathrm{d}\boldsymbol{x}' \frac{n(\boldsymbol{x},\boldsymbol{R})n(\boldsymbol{x}',\boldsymbol{R})}{|\boldsymbol{x}-\boldsymbol{x}'|}. \tag{1.2.9}$$

This approximation is often not sufficient, and we should consider the contribution that comes from the fact that the wavefunction is not a product of single-particle wavefunctions, but contains correlations between pairs of particles. Such a contribution is usually called $E_{xc}[n](\boldsymbol{R})$, the exchange-correlation contribution, and finding a form for this functional is an important step in setting up the particular model. In total, the electron-electron interaction can then be split into E_H and E_{xc} as

$$E_{el,el}[n](\boldsymbol{R}) = E_H[n](\boldsymbol{R}) + E_{xc}[n](\boldsymbol{R}). \tag{1.2.10}$$

There is a very important result [Hohenberg and Kohn, 1964, Gilbert, 1975] that states that we can construct any density describing a system of N_e particles from a single Slater determinant formed by single-particle wavefunctions and respecting the antisymmetric property. If $\phi_i(\boldsymbol{x},\boldsymbol{R})$ are the single-particle wavefunctions in the Slater determinant, the density is built as

$$n(\boldsymbol{x},\boldsymbol{R}) = \sum_{i=1}^{N_e} |\phi_i(\boldsymbol{x},\boldsymbol{R})|^2. \tag{1.2.11}$$

This is a very important result, because we can find a one particle formulation that allows us to describe the ground state of the system in terms of a one particle Schrödinger equation. Our goal is to minimize the functional $E^{el}[n](\boldsymbol{R})$, keeping appropriate normalization conditions for the wavefunctions $\phi_i(\boldsymbol{x},\boldsymbol{R})$. Introducing N_e Lagrange multipliers ϵ_i, this amounts to solving

$$\frac{\delta(E^{el}[n](\boldsymbol{R}) - \sum_{j=1}^{N_e}\epsilon_j(\int \mathrm{d}\boldsymbol{x}'|\phi_j(\boldsymbol{x},\boldsymbol{R})|^2 - 1))}{\delta\phi_i^*(\boldsymbol{x},\boldsymbol{R})} = 0. \tag{1.2.12}$$

[†]In principle, E_H also contains the electron self-interaction, due to the fact that the two fields can be evaluated at the same spatial coordinate in the integral.

In order to expand this expression, we note that

$$\left\langle \psi^{el}_{\boldsymbol{R}} \right| T \left| \psi^{el}_{\boldsymbol{R}} \right\rangle = -\frac{1}{2}\sum_{i=1}^{N_e} \int \mathrm{d}\boldsymbol{x}\, \phi_i^*(\boldsymbol{x},\boldsymbol{R})\nabla^2\phi_i(\boldsymbol{x},\boldsymbol{R}) = T[n](\boldsymbol{R}), \tag{1.2.13}$$

where we have used equation (1.2.11) to exchange the dependency from the single particle wavefunctions with the density dependency.

Expanding the potential term, the equation to solve becomes

$$\frac{\delta T[n](\boldsymbol{R})}{\delta\phi_i^*(\boldsymbol{x},\boldsymbol{R})} + (V_{ext}(\boldsymbol{x}) + V_H(\boldsymbol{x}) + V_{xc}(\boldsymbol{x}))\frac{\delta n(\boldsymbol{x},\boldsymbol{R})}{\delta\phi_i^*(\boldsymbol{x},\boldsymbol{R})} = \epsilon_i\phi_i(\boldsymbol{x},\boldsymbol{R}). \tag{1.2.14}$$

Here the kinetic term can be expanded as

$$\frac{\delta T[n](\boldsymbol{R})}{\delta\phi_i^*(\boldsymbol{x},\boldsymbol{R})} = -\frac{1}{2}\nabla^2\phi_i(\boldsymbol{x},\boldsymbol{R}), \tag{1.2.15}$$

and the potential terms are given by

$$V_{ext}(\boldsymbol{x},\boldsymbol{R}) = \frac{\delta E_{el,ion}[n](\boldsymbol{R})}{\delta n(\boldsymbol{x},\boldsymbol{R})}, \tag{1.2.16}$$

$$V_H(\boldsymbol{x},\boldsymbol{R}) = \frac{\delta E_H[n](\boldsymbol{R})}{\delta n(\boldsymbol{x},\boldsymbol{R})} = \int \mathrm{d}\boldsymbol{x}'\frac{n(\boldsymbol{x}',\boldsymbol{R})}{|\boldsymbol{x}-\boldsymbol{x}'|}, \tag{1.2.17}$$

$$V_{xc}(\boldsymbol{x},\boldsymbol{R}) = \frac{\delta E_{xc}[n](\boldsymbol{R})}{\delta n(\boldsymbol{x},\boldsymbol{R})}. \tag{1.2.18}$$

The sum of the three terms of the potential is defined to be the effective potential V_{eff}. We can finally rewrite (1.2.12) as[‡]

$$\left(-\frac{1}{2}\nabla^2 + V_{eff}(\boldsymbol{x})\right)\phi_i(\boldsymbol{x},\boldsymbol{R}) = \epsilon_i\phi_i(\boldsymbol{x},\boldsymbol{R}). \tag{1.2.19}$$

This is a one particle Schrodinger equation with effective Hamiltonian

$$H_{eff} = -\frac{1}{2}\nabla^2 + V_{eff}(\boldsymbol{x}). \tag{1.2.20}$$

We have succeeded in transforming the complicated electronic problem in a single particle quantum mechanical problem, paying the price of exchanging a precisely known potential with an effective potential for which the form is unknown.

[‡]The effective potential V_{eff} also has a parametric dependence on $\boldsymbol{R}$, that we are going to keep implicit in the following.

This procedure has brought us to the Kohn-Sham equations [Kohn and Sham, 1965]. The main problem with determining the effective potential is the exchange-correlation factor V_{xc}.

Assumptions have to be made on the exchange-correlation factor in order to define the Hamiltonian (1.2.20). The simplest assumption was already made in [Kohn and Sham, 1965], in which the authors tested the idea of using a local-density description for the exchange-correlation factor. This approach is named as the local-density approximation (LDA), and the energy term is written as

$$E_{xc}^{LDA}[n](\boldsymbol{R}) = \int \mathrm{d}\boldsymbol{x}\; n(\boldsymbol{x},\boldsymbol{R})\epsilon_{xc}^{hom}(n(\boldsymbol{x},\boldsymbol{R})). \tag{1.2.21}$$

The ϵ_{xc}^{hom} is an energy density that depends only on the density. This approximation is expected to work for solids that can be considered homogeneous, but is not very good at describing systems in which this assumption cannot be taken, as molecules. For such systems, an improvement called the generalized gradient approximation (GGA) was developed. The main idea is to consider a dependency of the energy density not only on the density $n(\boldsymbol{x},\boldsymbol{R})$, but also on its gradient $\nabla n(\boldsymbol{x},\boldsymbol{R})$. The most common GGA functional is the Perdew-Burke-Ernzerhof functional (PBE) [Perdew et al., 1996]. This functional splits into an exchange part and a correlation part. The exchange part is written as

$$E_{x}^{GGA}(\boldsymbol{R}) = \int \mathrm{d}\boldsymbol{x}\; n(\boldsymbol{x},\boldsymbol{R})\epsilon_x(r_s)F_x(n(\boldsymbol{x},\boldsymbol{R}),\nabla n(\boldsymbol{x},\boldsymbol{R})). \tag{1.2.22}$$

Here r_s is defined to be the radius occupied by each electron through the equation

$$\frac{\Omega}{N_e} = \frac{4}{3}\pi r_s^3, \tag{1.2.23}$$

with Ω the volume of the crystal and the exchange density $\epsilon_x(r_s)$ is a constant given by

$$\epsilon_x(r_s) = -\frac{0.4582}{r_s}, \tag{1.2.24}$$

with the function F given by

$$F_x(n(\boldsymbol{x},\boldsymbol{R}),\nabla n(\boldsymbol{x},\boldsymbol{R})) = 1.804 - \frac{0.804}{1+3.663s^2}. \tag{1.2.25}$$

The s term is a dimensionless gradient dependent on the density, its gradient and the Fermi momentum k_F as[§]

$$s = \frac{|\nabla n(\boldsymbol{x}, \boldsymbol{R})|}{2k_F n(\boldsymbol{x}, \boldsymbol{R})}. \tag{1.2.26}$$

The correlation term depends on a constant density $\epsilon_c^{hom}(r_s)$, parametrized in [Perdew and Wang, 1992]. The functional is

$$E_c^{GGA}[n](\boldsymbol{R}) = \int \mathrm{d}\boldsymbol{x}\, n(\boldsymbol{x}, \boldsymbol{R})(\epsilon_c^{hom}(r_s) + H(r_s, t)), \tag{1.2.27}$$

with

$$H(r_s, t) = \gamma \ln\left(1 + 0.215t^2\left(\frac{1 + At^2}{1 + At^2 + A^2t^4}\right)\right), \tag{1.2.28}$$

where $\gamma = 0.031091$, $t = sk_F/k_s$ (with $k_s = \sqrt{4k_F/\pi}$ the Thomas-Fermi screening wave number) and the factor A is

$$A = 0.215\left(\mathrm{e}^{\frac{\epsilon_c^{hom}(r_s)}{0.031}} - 1\right)^{-1}. \tag{1.2.29}$$

The total PBE functional is then the sum of the exchange and correlation terms.

1.2.2 Crystal periodicity and plane waves

Due to the lattice periodicity in a solid, the effective potential V_{eff} will have the same periodicity of the lattice. Namely, given a lattice vector $\boldsymbol{T}$, the effective potential will have the property

$$V_{eff}(\boldsymbol{x}) = V_{eff}(\boldsymbol{x} + \boldsymbol{T}). \tag{1.2.30}$$

We can then solve the Kohn-Sham equation (1.2.20) using the Bloch theorem [Bloch, 1929]: the wavefunction is indexed by a momentum $\boldsymbol{k}$ and a band index n, and is of the form

$$\phi_{n,\boldsymbol{k}}(\boldsymbol{x}, \boldsymbol{R}) = u_{n,\boldsymbol{k}}(\boldsymbol{x}, \boldsymbol{R})\mathrm{e}^{\mathrm{i}\boldsymbol{k}\cdot\boldsymbol{x}}, \tag{1.2.31}$$

[§]The Fermi momentum k_F is defined in terms of the Fermi energy ϵ_F. The Fermi energy is the highest energy level occupied by an electron, while the Fermi momentum is the momentum associated to the Fermi energy, $\sqrt{2\epsilon_F}$.

where the function u is periodic in $\boldsymbol{x}$ with the lattice periodicity. We can restrict the momentum $\boldsymbol{k}$ in the first Brillouin zone (1BZ), and apply boundary conditions on the wavefunction such as the 1BZ is composed by N_c distinct vectors, where N_c is the number of unit cells in the system.

The first step in solving a Schrödinger equation consists in choosing an appropriate basis. We use the plane wave basis

$$\langle \boldsymbol{x}|\boldsymbol{q}\rangle = \frac{1}{\sqrt{\Omega}} \mathrm{e}^{\mathrm{i}\boldsymbol{q}\cdot\boldsymbol{x}}, \tag{1.2.32}$$

where we recall that the normalization factor Ω is the volume of the whole crystal, $\Omega = N_c \Omega_{cell}$, with Ω_{cell} the volume of a single cell. This basis is used to expand $u_{n,\boldsymbol{k}}$ as

$$u_{n,\boldsymbol{k}}(\boldsymbol{x}, \boldsymbol{R}) = \sum_{\boldsymbol{q}} c_{n,\boldsymbol{k}+\boldsymbol{q}} \mathrm{e}^{\mathrm{i}\boldsymbol{q}\cdot\boldsymbol{x}}. \tag{1.2.33}$$

with $c_{n,\boldsymbol{k}+\boldsymbol{q}}$ complex coefficients. In order to have periodicity, we must have

$$u_{n,\boldsymbol{k}}(\boldsymbol{x}+\boldsymbol{T}, \boldsymbol{R}) = u_{n,\boldsymbol{k}}(\boldsymbol{x}, \boldsymbol{R}) \implies \exp\left(\mathrm{i}\boldsymbol{q}\cdot\boldsymbol{T}\right) = 1. \tag{1.2.34}$$

This restricts the number of possible momenta $\boldsymbol{q}$, and the momenta with this property are in the reciprocal lattice. Any Kohn-Sham state $\phi_{n,\boldsymbol{k}}$ will then be written as

$$\phi_{n,\boldsymbol{k}}(\boldsymbol{x}, \boldsymbol{R}) = \sum_{\boldsymbol{G}} c_{n,\boldsymbol{k}+\boldsymbol{G}} \mathrm{e}^{\mathrm{i}(\boldsymbol{k}+\boldsymbol{G})\cdot x}, \tag{1.2.35}$$

where the sum is extended over all reciprocal lattice vectors. As this sum is infinite, for numerical computations a cutoff on the energy is usually imposed, and this cutoff has to be taken larger for localized states.

The eigenvalues of the effective Hamiltonian are written as

$$H_{eff}\left|\phi_{n,\boldsymbol{k}}\right\rangle = \epsilon_{n,\boldsymbol{k}}\left|\phi_{n,\boldsymbol{k}}\right\rangle, \tag{1.2.36}$$

so the eigenvalues have to be found at each point of the 1BZ, and the different levels will form the energy bands. Lastly, the electron density $n(\boldsymbol{x}, \boldsymbol{R})$ is described here as

$$n(\boldsymbol{x}, \boldsymbol{R}) = \sum_{n} \sum_{\boldsymbol{k}\in 1\mathrm{BZ}} f_{n,\boldsymbol{k}} |\phi_{n,\boldsymbol{k}}(\boldsymbol{x}, \boldsymbol{R})|^2, \tag{1.2.37}$$

with $f_{n,\boldsymbol{k}}$ the Fermi-Dirac distribution of Fermi energy ϵ_F given by

$$f_{n,\boldsymbol{k}} = \frac{1}{\mathrm{e}^{\beta(\epsilon_{n,\boldsymbol{k}}-\epsilon_F)}+1}, \tag{1.2.38}$$

with $\beta = 1/T$ the reciprocal temperature. We further define the Fermi surface as the collection of $\boldsymbol{k}$ for which $\epsilon_{n,\boldsymbol{k}} = \epsilon_F$ for some n. A last important definition is the density of states (DOS) per unit cell at energy ϵ, given by

$$N(\epsilon) = \frac{1}{N_c}\sum_{\boldsymbol{k}\in 1BZ}\sum_{n}\delta(\epsilon-\epsilon_{n,\boldsymbol{k}}). \tag{1.2.39}$$

In particular, the DOS at the Fermi level $N(\epsilon_F)$ will play a very important role.

Lastly, as stated, the first Brillouin zone is composed of N_c vectors, so the sum is over a finite number of terms. Still, N_c is a large number, and for practical computation we will use smaller grids, called Monkhorst-Pack grids [Monkhorst and Pack, 1976]. We will do this whenever we have to numerically compute a sum over the first Brillouin zone.

1.2.3 Pseudopotentials

After having established a method to deal with the electron problem, we need a method to lower the computational resources needed in order to perform the necessary computations. The method that we will present is the pseudopotential method, that practically reduces the number of dynamical electrons by "freezing" the highly localised ones.

In solids, we can group the electrons in two groups: core and valence electrons. The core electrons are the ones that are most bound to the nuclei, and are highly localised, needing high cutoff on the energy to be described (due to the fact that localised states need notable contributions from large momenta to be described appropriately). The behaviour of the core electrons is not much influenced by what happens outside of their particular atoms, so we can "repackage" them together with the ions, substituting them with a screening potential that keeps the valence electrons away from the ion and adding this term in the potential term of (1.2.20). Each electron frozen in this way reduces the degrees of freedom of the system. On the other hand, valence electrons are not localised, and they are the main

source of interactions between the different ions in a solid. The pseudopotential method allows us to discard the degrees of freedom that do not contribute in the interactions between atoms in a solid, and to focus on the valence electrons that are more important for our scope.

In the description of pseudopotentials, a core radius r_c is often chosen to signify a distance from the ions in which the localised electrons stand. The simplest example of a pseudopotential is the Ashcroft potential [Ashcroft, 1966], where the potential is assumed to be 0 inside r_c and $-Z/r$ outside, with Z the charge of the ion. This potential is too simple for our scope, as the freezing of core electrons should introduce nonlocal interaction terms between the core and valence electrons that have to be taken into account. In this subsection, we will describe the principles between the choice of a pseudopotential.

First, we will describe norm conserving pseudopotentials [Hamann et al., 1979]. The first step is to select an electron configuration, i.e. choose the electrons that will be considered as valence electrons. In order to understand the requirements for the pseudopotentials, we distinguish between pseudo wave functions ϕ_i^{ps} (where the index i runs from 1 to the number of valence electrons) and all electrons wave functions ϕ_i (the ones that we obtain from (1.2.20) keeping all the electrons unfrozen). Satisfactory pseudopotentials have the following properties: the pseudo eigenvalues and the all electrons eigenvalues must be as close as possible, the two different types of wavefunctions have to agree outside the core radius r_c that has to be chosen, logarithmic derivatives of the two kinds of wavefunctions must agree at r_c and, lastly, the norms must agree inside r_c:

$$\int_0^{r_c} \mathrm{d}r\, r^2 |\phi_i^{ps}(r, \boldsymbol{R})|^2 = \int_0^{r_c} \mathrm{d}r\, r^2 |\phi_i(r, \boldsymbol{R})|^2, \tag{1.2.40}$$

where in the last integration we have used the spherical coordinate r for $\boldsymbol{x}$.

Pseudopotentials are usually split in a local and a non local part. As an example, in [Kleinman and Bylander, 1982] the pseudopotential is written as

$$V^{ps}(\boldsymbol{x}, \boldsymbol{x}') = V_{loc}^{ps}(\boldsymbol{x}) + V_{sl}(\boldsymbol{x}, \boldsymbol{x}'), \tag{1.2.41}$$

where the first part is local and the second non local.

Norm conserving pseudopotentials yield accurate results, at the cost of pro-

ducing wavefunctions that are not very smooth[¶]. Losing smoothness in the wavefunction has a computational cost, so it would be preferable to find ways to smoothen such result by using different pseudopotentials. In [Vanderbilt, 1990] the ultrasoft pseudopotentials were introduced, that we analyse now.

Ultrasoft pseudopotentials aim to mantain the norm conservation condition (1.2.40) without sacrificing too much smoothness. First, we introduce

$$Q_{ij}(\boldsymbol{x},\boldsymbol{R}) = \phi_i(\boldsymbol{x},\boldsymbol{R})\phi_j(\boldsymbol{x},\boldsymbol{R}) - \phi_i^{ps}(\boldsymbol{x},\boldsymbol{R})\phi_j^{ps}(\boldsymbol{x},\boldsymbol{R}), \tag{1.2.42}$$

that measures the deviation of the pseudopotential wavefunction from the all electron wavefunction (thus measuring nonlocality). For perfect norm conservation, the integral of Q_{ij} is zero inside r_c, but the introduction of this factor allows us to measure the loss of norm conservation and strike a balance between this loss and the gain in smoothness. Due to the loss in the norm conservation, we have a loss in the valence charge in the core. This can be remedied in the following way. First, introduce projectors $|\beta_i\rangle$ depending on the ionic position, and then redefine the charge density as

$$n(\boldsymbol{x},\boldsymbol{R}) = \sum_{n=1}^{N_v}\sum_{\boldsymbol{k}\in 1\mathrm{BZ}} f_{n\boldsymbol{k}}\left(|\phi_{n\boldsymbol{k}}(\boldsymbol{x},\boldsymbol{R})|^2 + \sum_{ij} Q_{ij}(\boldsymbol{x},\boldsymbol{R})\,\langle\phi_{n\boldsymbol{k}}^{ps}|\beta_j\rangle\,\langle\beta_i|\phi_{n\boldsymbol{k}}^{ps}\rangle\right), \tag{1.2.43}$$

with $f_{n\boldsymbol{k}}$ coefficients that can be tuned to restore the correct amount of charge (the first sum is done over the N_v valence electrons, as expected in the pseudopotential method). The functions Q_{ij} are known as augmentation functions, due to their use as functions that can restore the charge density to the correct levels. Lastly, in this formalism, the orthogonality condition between pseudo wave functions is

$$\langle\phi_{n\boldsymbol{k}}|\,S\,|\phi_{n'\boldsymbol{k}}\rangle = \delta_{nn'}, \qquad S = 1 + \sum_{i,j=1}^{N_v} Q_{ij}\,|\beta_i\rangle\,\langle\beta_j|\,. \tag{1.2.44}$$

This formalism allows us to cut the energy that is required to describe the wavefunction, at the cost of introducing further complication in the formalism itself.

[¶]Here by "smooth" we do not intend the mathematical definition, but a more practical one: smooth wavefunctions are wavefunctions whose derivatives are not too large, meaning that the number of momenta that are needed to describe the wavefunction accurately is not too large.

1.3 Lattice dynamics of crystals

The Born-Oppenheimer method allows us to separate the electronic and ionic problem. As a first approximation, we can consider the ions frozen in place, as their masses are very large with respect to the electron masses. This comes at the cost of losing lots of interesting physical phenomena that can be explained only when we allow the ions to move. In this section we aim to go beyond the frozen ions approximation, introducing the basics of phonons and their dynamics in a crystal.

In a lattice, ions can be identified by coordinates that can be written in terms of the translation vectors. We first need to introduce some terminology. Here we will assume that the unit cell is composed by n_b ions, that are at the positions $\boldsymbol{d}_\nu$. Letters from the middle of the Greek alphabet will index those ions, so we have $\nu = 1, ..., n_b$. Letters from the beginning of the Greek alphabet will index the particular spatial coordinate, so we will have symbols like α ranging over $x, y.z$ (or equivalently $1, 2, 3$)[‖]. Lastly, we will use Latin lowercase letters to indicate the particular cells we are referring to (as $a = 1, ..., N_c$). We will often suppress the limits of summations for the sake of brevity. With this terminology, the ν-th ion at rest in the $n-$th cell has coordinate $\boldsymbol{T}_n + \boldsymbol{d}_\nu$, where $\boldsymbol{T}_n$ is a lattice vector. We want to introduce small displacements from the equilibrium positions, and we will indicate them as $\boldsymbol{u}_{n\nu}$. Under those assumptions, we can write more in generality the position of a displaced ion as $\boldsymbol{T}_n + \boldsymbol{d}_\nu + \boldsymbol{u}_{n\nu}$. We will indicate as $\boldsymbol{R}_0 + \boldsymbol{u}$ the collective coordinates in which the $I-$th atom is displaced by the displacement $\boldsymbol{u}_{n\nu}$, according to its cell n and the position ν of its representative in the unit cell. From (1.1.9), we see that the ions move in the potential defined by $E^{el}(\boldsymbol{R})$. We use the notation $\boldsymbol{R}_0$ to stress that the equilibrium configuration $\boldsymbol{u} = 0$ is the configuration at which the energy E^{el} is minimized.

With deformations, the energy of the lattice changes. We can assume that those changes will be small, so we can write the perturbed energy as

$$E^{el}(\boldsymbol{R}_0 + \boldsymbol{u}) = E^{el}(\boldsymbol{R}_0) + \frac{1}{2} \sum_{n\nu\alpha, n'\nu'\alpha'} \Phi_{n\nu\alpha,n'\nu'\alpha'} u_{n\nu\alpha} u_{n'\nu'\alpha'}. \tag{1.3.1}$$

[‖] Alternatively, we will indicate Cartesian vectors in bold, as in the last sections.

The matrix Φ is called the force constants matrix, and is given by

$$\Phi_{n\nu\alpha,n'\nu'\alpha'} = \left[\frac{\partial^2 E^{el}(\boldsymbol{R}_0+\boldsymbol{u})}{\partial u_{n\nu\alpha}\partial u_{n'\nu'\alpha'}}\right]_{\boldsymbol{u}=0}. \tag{1.3.2}$$

This matrix has to be positive definite in order to have $E^{el}(\boldsymbol{R}_0)$ as a minimum. Furthermore, we have the property

$$\Phi_{n\nu\alpha,n'\nu'\alpha'} = \Phi_{m\nu\alpha,m'\nu'\alpha'} \tag{1.3.3}$$

if $\boldsymbol{T}_n - \boldsymbol{T}_{n'} = \boldsymbol{T}_m - \boldsymbol{T}_{m'}$. This is due to lattice periodicity, as only the distance between cells is important. Under a full translation of the crystal the energy must be invariant: from this, we have the property

$$\sum_{n'\nu'} \Phi_{n\nu\alpha,n'\nu'\alpha'} = 0. \tag{1.3.4}$$

Lastly, due to its definition through partial derivatives, the matrix is symmetric under the exchange of its indexes (the first three with the last three).

The system (1.3.1) is a system of independent harmonic oscillators. Its classical equations of motion are simply given by

$$M_\nu \ddot{u}_{n\nu\alpha} = -\sum_{n'\nu'\alpha'} \Phi_{n\nu\alpha,n'\nu'\alpha'} u_{n'\nu'\alpha'}, \tag{1.3.5}$$

where the dots indicate derivation with respect to time. Solutions to this system are in the form

$$\boldsymbol{u}_{n\nu} = \frac{1}{\sqrt{M_\nu}} \boldsymbol{A}_\nu(\boldsymbol{q},\omega) \mathrm{e}^{\mathrm{i}(\boldsymbol{q}\cdot\boldsymbol{T}_n - \omega t)}, \tag{1.3.6}$$

with the vectors $\boldsymbol{A}_\nu$ being called polarization vectors of the system and M_ν is the mass of the atom in the ν position in the unit cell. Non zero solutions are obtained by plugging this form in equation (1.3.5):

$$-M_\nu \omega^2 A_{\nu\alpha} = -\sum_{n'\nu'\alpha'} \frac{\Phi_{n\nu\alpha,n'\nu'\alpha'}}{\sqrt{M_\nu M_{\nu'}}} \mathrm{e}^{-\mathrm{i}\boldsymbol{q}(\boldsymbol{T}_n - \boldsymbol{T}_{n'})} A_{\nu'\alpha'}. \tag{1.3.7}$$

This eigenvalue equation admits non zero solutions if and only if the determinant of

$$D_{\nu\alpha,\nu'\alpha'}(\boldsymbol{q}) - \omega^2 \delta_{\alpha,\alpha'}\delta_{\nu,\nu'} \tag{1.3.8}$$

is zero, with

$$D_{\nu\alpha,\nu'\alpha'}(\boldsymbol{q}) = \sum_{\boldsymbol{n}'} \frac{\Phi_{0\nu\alpha,n'\nu'\alpha'}}{\sqrt{M_\nu M_{\nu'}}} \mathrm{e}^{\mathrm{i}\boldsymbol{q}\cdot\boldsymbol{T}_{n'}} \tag{1.3.9}$$

being the dynamical matrix in momentum space**. The eigenvalues of the secular equation are indexed by and index p and are functions of $\boldsymbol{q}$, so they are written as $\omega_p(\boldsymbol{q})$, with the index p running from 0 to $3n_b$. We index the polarization vectors in a similar way. In order to univocally define the polarization vectors, we impose the normalization condition

$$\sum_{\nu\alpha} A^*_{\nu\alpha}(\boldsymbol{q},p) A_{\nu\alpha}(\boldsymbol{q},p') = \delta_{p,p'}. \tag{1.3.10}$$

A last important property of the classical theory comes from the sum rule (1.3.4). In the limit $\boldsymbol{q} \to 0$ we have

$$\sum_{\nu'} D_{\nu\alpha,\nu'\alpha'}(\boldsymbol{q}=0) = 0. \tag{1.3.11}$$

This implies that in the long wavelength limit there are three frequencies that vanish, corresponding to overall translations of the solid. The phonon modes that vanish at zero are denoted as acoustic modes, while the others are called optical modes.

The quantum theory corresponding to those harmonic oscillations is straightforward to obtain, and the excited states in this quantum theory are called phonons. For the quantization we have to take the kinetic energy into account, so the total Hamiltonian in momentum space is††

$$H_{ion} = \sum_{\substack{\nu\alpha \\ \boldsymbol{q}\in 1\mathrm{BZ}}} \frac{1}{2M_\nu} P_{\nu\alpha}(-\boldsymbol{q}) P_{\nu\alpha}(\boldsymbol{q}) + \frac{1}{2} \sum_{\substack{\nu\alpha,\nu'\alpha' \\ \boldsymbol{q}\in 1\mathrm{BZ}}} \Phi_{\nu\alpha,\nu'\alpha'}(\boldsymbol{q}) u_{\nu\alpha}(\boldsymbol{q}) u_{\nu'\alpha'}(-\boldsymbol{q}) + E^{el}(\boldsymbol{R}_0). \tag{1.3.13}$$

**Here we have used the periodicity property to set the first index to 0.

††For the Fourier transform of the coordinate, we have

$$u_{\nu\alpha}(\boldsymbol{q}) = \frac{1}{\sqrt{N_c}} \sum_n \mathrm{e}^{\mathrm{i}\boldsymbol{q}\cdot\boldsymbol{T}_n} u_{n\nu\alpha}, \tag{1.3.12}$$

so we trade the n index for a $\boldsymbol{q}$ dependency.

We can now proceed to the diagonalization of the Hamiltonian. The usual ladder operators are defined through

$$u_{\nu\alpha}(\boldsymbol{q}) = \sum_p \frac{1}{\sqrt{2M_\nu \omega_p(\boldsymbol{q})}} A_{\nu\alpha}(\boldsymbol{q}, p) \left(b_{p\boldsymbol{q}} + b^\dagger_{p\boldsymbol{q}}\right), \tag{1.3.14}$$

$$P_{\nu\alpha}(\boldsymbol{q}) = -\mathrm{i} \sum_p \sqrt{\frac{M_\nu \omega_p(\boldsymbol{q})}{2}} A_{\nu\alpha}(\boldsymbol{q}, p) \left(b_{p\boldsymbol{q}} - b^\dagger_{p\boldsymbol{q}}\right). \tag{1.3.15}$$

The ladder operators $b_{p\boldsymbol{q}}$ and $b^\dagger_{p\boldsymbol{q}}$, respectively, destroy and create phonon states with momenta $\boldsymbol{q}$ and frequency $\omega_p(\boldsymbol{q})$, obeying the algebra

$$[b_{p\boldsymbol{q}}, b^\dagger_{p'\boldsymbol{q}'}] = \delta_{pp'}\delta_{\boldsymbol{q}\boldsymbol{q}'}, \tag{1.3.16}$$

and all the other commutators vanish. The final quantum Hamiltonian for phonons is then

$$H_{ion} = E^{el}(\boldsymbol{R}_0) + \sum_p \sum_{\boldsymbol{q}\in 1\mathrm{BZ}} \omega_p(\boldsymbol{q}) \left(b^\dagger_{p\boldsymbol{q}} b_{p\boldsymbol{q}} + \frac{1}{2}\right). \tag{1.3.17}$$

1.4 Density functional perturbation theory

From a purely theoretical point of view, there is no problem in defining the dynamical matrix of a crystal and computing the phonon spectrum. On the other hand, from a computational point of view this can be very complicated. Density functional perturbation theory (DFPT) provides an excellent framework in which the lattice displacements are studied through their effects on the DFT density $n(\boldsymbol{x}, \boldsymbol{R}_0)$.

The first step in computing the dynamical matrix is computing the energy of the system as

$$E^{el}(\boldsymbol{R}_0) = \left\langle \psi^{el}_{\boldsymbol{R}_0} \right| H_e \left| \psi^{el}_{\boldsymbol{R}_0} \right\rangle, \tag{1.4.1}$$

In order to compute the dynamical matrix, we have to take two derivatives of the energy with respect to the displacements.

The first derivative can be taken by using the Hellmann-Feynman theorem [Hellmann et al., 1937, Feynman, 1939]. The derivative is

$$\frac{\partial E^{el}(\boldsymbol{R}_0 + \boldsymbol{u})}{\partial u_{n\nu\alpha}} = \frac{\partial V_{ion,ion}}{\partial u_{n\nu\alpha}} + \int \mathrm{d}\boldsymbol{x}\, n(\boldsymbol{x}, \boldsymbol{R}_0) \frac{\partial V_{ext}(\boldsymbol{x})}{\partial u_{n\nu\alpha}}, \tag{1.4.2}$$

where $V_{ion,ion}$ is the Coulomb interaction between phonons and we have used DFT in order to write the derivative of the V_{ext} part of $\left\langle \psi^{el}_{\boldsymbol{R}_0} \right| H_e \left| \psi^{el}_{\boldsymbol{R}_0} \right\rangle$ as an integration involving the density function. The second derivative is now straightforward, and we can perform the evaluation at zero displacement

$$\begin{aligned}\left[\frac{\partial E(\boldsymbol{R}_0+\boldsymbol{u})}{\partial u_{n\nu\alpha}\partial u_{n'\nu'\alpha'}}\right]_0 &= \int \mathrm{d}\boldsymbol{x}\left[\frac{\partial n(\boldsymbol{x},\boldsymbol{R}_0)}{\partial u_{n'\nu'\alpha'}}\right]_{\boldsymbol{u}=0}\left[\frac{\partial V_{ext}(\boldsymbol{x})}{\partial u_{n\nu\alpha}}\right]_{\boldsymbol{u}=0} + \\ &+ \int \mathrm{d}\boldsymbol{x}\, n(\boldsymbol{x},\boldsymbol{R}_0)\left[\frac{\partial^2 V_{ext}(\boldsymbol{x})}{\partial u_{n'\nu'\alpha'}\partial u_{n\nu\alpha}}\right]_{\boldsymbol{u}=0} + \left[\frac{\partial^2 V_{ion,ion}(\boldsymbol{x})}{\partial u_{n'\nu'\alpha'}\partial u_{n\nu\alpha}}\right]_{\boldsymbol{u}=0}.\end{aligned} \tag{1.4.3}$$

The computation of this second derivative is very demanding at a computational level due to the presence of the derivative of the electron density with respect to the ion displacements. The DFPT method provides an alternative way of performing this computation, by providing an alternative self-consistent set of equations derived from perturbation theory. Its main idea is to study the change of Kohn-Sham levels and wavefunctions when the density is perturbed in a certain way. As in perturbation theory, the idea is to perturb the functions and operators from the equilibrium position as

$$H_{eff} \to H_{eff} + \Delta H_{eff}, \tag{1.4.4}$$

$$\epsilon_{n,\boldsymbol{k}} \to \epsilon_{n,\boldsymbol{k}} + \Delta\epsilon_{n,\boldsymbol{k}}, \tag{1.4.5}$$

$$|\phi_{n,\boldsymbol{k}}\rangle \to |\phi_{n,\boldsymbol{k}}\rangle + |\Delta\phi_{n,\boldsymbol{k}}\rangle\,, \tag{1.4.6}$$

$$n(\boldsymbol{x},\boldsymbol{R}_0) \to n(\boldsymbol{x},\boldsymbol{R}_0) + \Delta n(\boldsymbol{x},\boldsymbol{R}_0). \tag{1.4.7}$$

The quantities with the Δ are the objects of study, and they are determined through [Sternheimer, 1954]

$$(H_{eff} - \epsilon_{n,\boldsymbol{k}})\,|\Delta\phi_{n,\boldsymbol{k}}\rangle = -(\Delta H_{eff} - \Delta\epsilon_{n,\boldsymbol{k}})\,|\phi_{n,\boldsymbol{k}}\rangle\,, \tag{1.4.8}$$

which is the perturbed eigenvalue problem at linear order,

$$\Delta n(\boldsymbol{x},\boldsymbol{R}_0) = 2\,\mathrm{Re}\sum_n \sum_{\boldsymbol{k}\in 1\mathrm{BZ}} f_{n,\boldsymbol{k}}\phi^*_{n,\boldsymbol{k}}(\boldsymbol{x},\boldsymbol{R}_0)\Delta\phi_{n,\boldsymbol{k}}(\boldsymbol{x},\boldsymbol{R}_0), \tag{1.4.9}$$

where $f_{n,\boldsymbol{k}}$ are the Fermi-Dirac distributions in (1.2.38) determined through the unperturbed Kohn-Sham levels, and the Hamiltonian changes as

$$\Delta H_{eff}(\boldsymbol{x}) = \Delta V_{ext}(\boldsymbol{x}) + \int \mathrm{d}\boldsymbol{x}'\left(\frac{1}{|\boldsymbol{x}-\boldsymbol{x}'|} + f^{xc}(\boldsymbol{x},\boldsymbol{x}')\right)\Delta n(\boldsymbol{x}',\boldsymbol{R}_0), \tag{1.4.10}$$

and the factor f^{xc} is defined as the exchange-correlation term in function of the density as

$$f^{xc}(\boldsymbol{x}, \boldsymbol{x}') = \frac{\delta V_{xc}(\boldsymbol{x})}{\delta n(\boldsymbol{x}', \boldsymbol{R}_0)}. \tag{1.4.11}$$

The goal of the formalism is to obtain the variation $\Delta n(\boldsymbol{x}, \boldsymbol{R}_0)$ self-consistently, from which the derivative $\partial n(\boldsymbol{x}, \boldsymbol{R}_0)/\partial u_{n\nu\alpha}$ can be obtained. The advantage of this procedure is that it can be done to compute the dynamical matrix (1.3.13) at each value of $\boldsymbol{q}$ separately. Thus, DFPT is a very useful tool in computing the dynamical matrix of the system and avoid supercell approaches.

1.5 Electron-phonon interaction

After having studied the electronic system and the phonon system separately, we now turn to the interaction between electrons and phonons. In (1.1.7), we have introduced a term that couples the ion momenta with the electronic wavefunctions, but in the rest of the discussion we have chosen to neglect its effect. For the study of superconductivity this term turns out to be fundamental.

The procedure begins with an approximation. (1.1.7) is made of a sum of two terms. The former is made by second derivatives of the electron wavefunctions in terms of the ionic coordinates (and, as a consequence, the ionic displacements), while the second term only has first derivatives. In a linear approximation, it is safe to neglect the first term. We rewrite the electron-phonon interaction as

$$\Delta H_\alpha = \sum_I \frac{1}{M_I} \left[\boldsymbol{P}_I\right]_e \boldsymbol{P}_I, \tag{1.5.1}$$

where we have already turned to operator formalism and $\left[P_I\right]_e$ is the average over electron states[‡‡]. We can use second quantization by quantizing the Kohn-Sham energy levels, introducing creation and annihilation operators $c^\dagger_{n\boldsymbol{k}}$ and $c_{n\boldsymbol{k}}$, which create and destroy electrons in a Kohn-Sham state $|\phi_{n\boldsymbol{k}}\rangle$[§§]. The operator $\left[P_I\right]_e$ is

[‡‡]In this section, we will alternate between using the index I running over all ions, and a pair of indexes n, ν running over all translational cells and the atoms in the first cell respectively as was done when computing the phonon modes.

[§§]Due to the fact that the operators $c^\dagger_{n\boldsymbol{k}}$ and $c_{n\boldsymbol{k}}$ create and destroy electrons, we impose anticommutation relations: $\{c_{n\boldsymbol{k}}, c^\dagger_{n'\boldsymbol{k}'}\} = \delta_{nn'}\delta_{\boldsymbol{k}\boldsymbol{k}'}$, and all other anticommutators vanish.

in this formalism

$$[\boldsymbol{P}_I]_e = \sum_{n,n'} \sum_{\boldsymbol{k},\boldsymbol{k}'\in 1\mathrm{BZ}} c^\dagger_{n'\boldsymbol{k}'} c_{n\boldsymbol{k}} \langle \phi_{n'\boldsymbol{k}'} | P_I | \phi_{n\boldsymbol{k}} \rangle . \tag{1.5.2}$$

Using perturbation theory as in the DFPT method, it is easy to prove that

$$\langle \phi_{n'\boldsymbol{k}'} | \boldsymbol{P}_I | \phi_{n\boldsymbol{k}} \rangle = -\mathrm{i} \frac{\langle \phi_{n'\boldsymbol{k}'} | \frac{\partial H_{eff}}{\partial u_{I\alpha}} | \phi_{n\boldsymbol{k}} \rangle}{\epsilon_{n\boldsymbol{k}} - \epsilon_{n'\boldsymbol{k}'}}. \tag{1.5.3}$$

The unaveraged momentum in (1.5.1) can be expressed in terms of creation and destruction operators for phonons. The final Hamiltonian is then written as

$$\begin{aligned} H_{el-ph} = &- \sum_m \sum_\nu \frac{1}{M_\nu} \sum_\alpha \sum_{n,n'} \sum_{\boldsymbol{k},\boldsymbol{k}'\in 1\mathrm{BZ}} c^\dagger_{n'\boldsymbol{k}'} c_{n\boldsymbol{k}} \frac{\langle \phi_{n'\boldsymbol{k}'} | \frac{\partial H_{eff}}{\partial u_{m\nu\alpha}} | \phi_{n\boldsymbol{k}} \rangle}{\epsilon_{n\boldsymbol{k}} - \epsilon_{n'\boldsymbol{k}'}} \times \\ &\times \frac{1}{\sqrt{N_c}} \sum_p \sum_{\boldsymbol{q}\in 1\mathrm{BZ}} \mathrm{e}^{\mathrm{i}\boldsymbol{q}\cdot\boldsymbol{T}_m} \sqrt{\frac{M_\nu \omega_p(\boldsymbol{q})}{2}} A_{\nu\alpha}(\boldsymbol{q}, p) \left(b_{p\boldsymbol{q}} - b^\dagger_{p(-\boldsymbol{q})} \right). \end{aligned} \tag{1.5.4}$$

This interaction term is a sum of terms containing two electron operators and one phonon operator: this is interpreted in second quantization as a process in which an electron absorbs or emits a phonon, conserving momentum and energy. This Hamiltonian is generally grouped as

$$H_{el-ph} = \frac{1}{\sqrt{N_c}} \sum_p \sum_{\boldsymbol{q}\in 1\mathrm{BZ}} \sum_{n,n'} \sum_{\boldsymbol{k},\boldsymbol{k}\in 1\mathrm{BZ}} g^p_{n'\boldsymbol{k}+\boldsymbol{q},n\boldsymbol{k}} c^\dagger_{n'\boldsymbol{k}+\boldsymbol{q}} c_{n\boldsymbol{k}} \left(b_{p\boldsymbol{q}} + b^\dagger_{p(-\boldsymbol{q})} \right), \tag{1.5.5}$$

where the term g is denoted as the electron-phonon coupling function, given by

$$g^p_{n'\boldsymbol{k}+\boldsymbol{q},n\boldsymbol{k}} = \sum_m \sum_\nu \mathrm{e}^{\mathrm{i}\boldsymbol{q}\cdot\boldsymbol{T}_m} \frac{1}{\sqrt{2M_\nu \omega_p(\boldsymbol{q})}} \sum_\alpha \langle \phi_{n'\boldsymbol{k}+\boldsymbol{q}} | \frac{\partial H_{eff}}{\partial u_{m\nu\alpha}} A_{\nu\alpha}(\boldsymbol{q}, p) | \phi_{n\boldsymbol{k}} \rangle. \tag{1.5.6}$$

This will be a very important object to study superconductivity mediated by the electron-phonon interaction. We can now use the Migdal-Eliashberg theory [Migdal, 1958, Eliashberg, 1960] in order to describe the critical temperature for superconductivity. Describing the theory is out of the scope of the present thesis: we will show the results that are used in our work, referring to the review [Giustino, 2017a] for a more in depth examination of those topics.

The main quantity of interest in the theory is the Eliashberg function

$$\alpha^2 F_{nn'}(\boldsymbol{k}, \boldsymbol{k}+\boldsymbol{q}, \omega) = N(\epsilon_F) \sum_p \left| g^p_{n'\boldsymbol{k}+\boldsymbol{q},n\boldsymbol{k}} \right|^2 \delta(\omega - \omega_p(\boldsymbol{q})), \tag{1.5.7}$$

where $N(\epsilon_F)$ is the density of states at the Fermi energy

$$N(\epsilon_F) = \frac{1}{N_c}\sum_{n\boldsymbol{k}} \delta(\epsilon_{n\boldsymbol{k}} - \epsilon_F), \tag{1.5.8}$$

with ϵ_F the Fermi energy and δ the Dirac delta. This quantity is used to compute the effective electron phonon coupling

$$\begin{aligned}\lambda_n(\boldsymbol{k}) = \frac{1}{N_c}\frac{1}{N(\epsilon_F)}\sum_{\boldsymbol{q}\in 1\mathrm{BZ}}\sum_{n'}\int_0^\infty \mathrm{d}\omega' \alpha^2 F_{nn'}(\boldsymbol{k},\boldsymbol{k}+\boldsymbol{q},\omega')\times \\ \times\left[\frac{f_{n'\boldsymbol{k}+\boldsymbol{q}}}{(\omega'-\epsilon_{n'\boldsymbol{k}+\boldsymbol{q}})}+\frac{1-f_{n'\boldsymbol{k}+\boldsymbol{q}}}{(\omega'+\epsilon_{n'\boldsymbol{k}+\boldsymbol{q}})}\right],\end{aligned} \tag{1.5.9}$$

which measures how much the $n-$th Kohn-Sham level with wave number $\boldsymbol{k}$ is affected by the electron-phonon coupling. We can assume that the distributions in (1.5.9) are peaked at ϵ_F and then take averages. We redefine as electron-phonon coupling and Eliashberg function the averages of (1.5.8) and (1.5.9) on the Fermi surface:

$$\lambda = \frac{1}{N(\epsilon_F)N_c}\sum_n\sum_{\boldsymbol{k}\in 1\mathrm{BZ}}\lambda_n(\boldsymbol{k},\omega)\delta(\epsilon_{n\boldsymbol{k}}-\epsilon_F), \tag{1.5.10}$$

$$\alpha^2F(\omega) = \frac{1}{N(\epsilon_F)^2N_c^2}\sum_{n,n'}\sum_{\boldsymbol{k},\boldsymbol{q}\in 1\mathrm{BZ}}\alpha^2F_{nn'}(\boldsymbol{k},\boldsymbol{k}+\boldsymbol{q},\omega)\delta(\epsilon_{n\boldsymbol{k}}-\epsilon_F)\delta(\epsilon_{n'\boldsymbol{k}+\boldsymbol{q}}-\epsilon_F) \tag{1.5.11}$$

The Eliashberg function can then be simplified as

$$\begin{aligned}\alpha^2F(\omega) =& \frac{1}{N(\epsilon_F)N_c^2}\sum_{n,n'}\sum_{\boldsymbol{k},\boldsymbol{q}\in 1\mathrm{BZ}}\sum_p \left|g^p_{n'\boldsymbol{k}+\boldsymbol{q},n\boldsymbol{k}}\right|^2\times \\ &\times\delta(\omega-\omega_p(\boldsymbol{q}))\delta(\epsilon_{n\boldsymbol{k}}-\epsilon_F)\delta(\epsilon_{n'\boldsymbol{k}+\boldsymbol{q}}-\epsilon_F),\end{aligned} \tag{1.5.12}$$

allowing the computation of the electron-phonon coupling constant as

$$\lambda = 2\int_0^\infty \mathrm{d}\omega\frac{\alpha^2F(\omega)}{\omega}. \tag{1.5.13}$$

We will also plot the contributions to λ from frequencies below ω, defined as

$$\lambda(\omega) = 2\int_0^\omega \mathrm{d}\omega'\frac{\alpha^2F(\omega')}{\omega'}. \tag{1.5.14}$$

A quantity that is often computed in literature is the electron-phonon coupling contribution to the phonon linewidth, defined as

$$\gamma_p(\boldsymbol{k}) = \frac{2\pi\omega_p(\boldsymbol{k})}{N_c}\sum_{nn'}\sum_{\boldsymbol{q}\in 1\mathrm{BZ}}\left|g^p_{n'\boldsymbol{k}+\boldsymbol{q},n\boldsymbol{q}}\right|^2\delta(\epsilon_{n'\boldsymbol{k}+\boldsymbol{q}}-\epsilon_F)\delta(\epsilon_{n\boldsymbol{q}}-\epsilon_F), \tag{1.5.15}$$

and in terms of this quantity the Eliashberg function can be written as

$$\alpha^2F(\omega) = \frac{1}{2\pi N(\epsilon_F)N_c}\sum_{p\boldsymbol{k}}\frac{\gamma_p(\boldsymbol{k})}{\omega_p(\boldsymbol{k})}\delta(\omega-\omega_p(\boldsymbol{k})). \tag{1.5.16}$$

This is an alternative formula equivalent to (1.5.12), that we will use in some applications.

For superconductivity, the parameter λ is very effective in calculating the critical temperature T_c below which the system is in a superconducting state. The approach to computing the critical temperature passes through solving the Eliashberg equations [Allen and Mitrović, 1983], but in this thesis we will take a simpler approach. We will compute the critical temperature through the McMillan equation [McMillan, 1968] that reads

$$T_c = \frac{\omega_{log}}{1.2}\exp\left(-\frac{1.04(1+\lambda)}{\lambda-\mu^*(1+0.62\lambda)}\right), \tag{1.5.17}$$

where ω_{log} is the logarithmic frequency average

$$\omega_{log} = \exp\left(\frac{2}{\lambda}\int_0^\infty \mathrm{d}\omega\frac{\alpha^2F(\omega)}{\omega}\ln\omega\right), \tag{1.5.18}$$

and μ^*, which is called the effective Coulomb potential, measures the effective electronic Coulomb repulsion and is a numerical value of order 0.1. This equation has been tested experimentally with good results [Carbotte, 1990]. We will also use the Allen-Dynes correction [Allen and Dynes, 1975]. For this equation, we define

$$\langle\omega^2\rangle = \frac{2}{\lambda}\int_0^\infty \mathrm{d}\omega\,\alpha^2F(\omega)\omega, \tag{1.5.19}$$

$$\Lambda_1 = 2.46(1+3.8\mu^*), \quad \Lambda_2 = 1.82(1+6.3\mu^*)\frac{\sqrt{\langle\omega^2\rangle}}{\omega_{log}}, \tag{1.5.20}$$

$$f_1 = \left[1+\left(\frac{\lambda}{\Lambda_1}\right)^{\frac{3}{2}}\right]^{\frac{1}{3}}, \quad f_2 = 1+\frac{\left(\sqrt{\langle\omega^2\rangle}/\omega_{log}-1\right)\lambda^2}{\lambda^2+\Lambda_2^2}. \tag{1.5.21}$$

The Allen-Dynes correction is then

$$T_c = \frac{f_1 f_2 \omega_{log}}{1.2} \exp\left(-\frac{1.04(1+\lambda)}{\lambda - \mu^*(1+0.62\lambda)}\right). \tag{1.5.22}$$

1.6 Beyond the harmonic approximation: the anharmonic effects

When studying the phonon system, we have approximated the energy (1.3.1) to second order in the displacements. While this approximation is the basis to define phonon systems, for our purposes it is not sufficient to only consider the harmonic Hamiltonian (1.3.17), which describes a system of non interacting phonons.

The procedure to introduce anharmonic contributions starts from including further derivatives in (1.3.1): as an example, the third order approximation reads

$$\begin{aligned} E^{el}(\boldsymbol{R}_0 + \boldsymbol{u}) = E^{el}(\boldsymbol{R}_0) + \frac{1}{2} \sum_{n\nu\alpha, n'\nu'\alpha'} \Phi_{n\nu\alpha,n'\nu'\alpha'} u_{n\nu\alpha} u_{n'\nu'\alpha'} + \\ + \frac{1}{3!} \sum_{n\nu\alpha,n'\nu'\alpha',n''\nu''\alpha''} \Phi_{n\nu\alpha,n'\nu'\alpha',n''\nu''\alpha''} u_{n\nu\alpha} u_{n'\nu'\alpha'} u_{n''\nu''\alpha''}, \end{aligned} \tag{1.6.1}$$

where

$$\Phi_{n\nu\alpha,n'\nu'\alpha',n''\nu''\alpha''} = \left[\frac{\partial^3 E(\boldsymbol{R}_0 + \boldsymbol{u})}{\partial u_{n\nu\alpha} \partial u_{n'\nu'\alpha'} \partial u_{n''\nu''\alpha''}}\right]_{\boldsymbol{u}=0}. \tag{1.6.2}$$

Even with the introduction of the third order term, the quantization procedure follows the same steps: in particular, the phonon displacements are still expressed in terms of creation and destruction operators as

$$u_{\nu\alpha}(\boldsymbol{q}) = \sum_p \frac{1}{\sqrt{2M_\nu \omega_p(\boldsymbol{q})}} A_{\nu\alpha}(\boldsymbol{q}, p) \left(b_{p\boldsymbol{q}} + b^\dagger_{p\boldsymbol{q}}\right), \tag{1.6.3}$$

$$\tag{1.6.4}$$

where as before $u_{\nu\alpha}(\boldsymbol{q})$ is defined from a Fourier transformation procedure, and the polarization vectors $A_{\nu\alpha}$ and the phonon frequencies $\omega_p(\boldsymbol{q})$ are obtained by diagonalizing the classical harmonic Hamiltonian, neglecting the higher order term. The

quantization procedure is then perturbative in nature: after using the harmonic Hamiltonian to characterize the non interacting phonon system, we introduce interactions between phonons through higher terms in the approximation of $E(\{\boldsymbol{u}_{n\nu}\})$. It can be shown that higher order terms have similar properties to (1.3.3) and (1.3.4), and as a consequence they describe phonon interactions in which the total energy and momentum are always conserved. Phonons are no longer well-defined quasiparticles, and perturbation theory has to be employed. As a consequence, the phonon frequencies of the system are changed and phonons acquire a finite lifetime. For more details on this part, the reader can consult [Paulatto et al., 2015].

Anharmonic contributions will be fundamental in our work in order to get the correct properties of some systems. As an example, [Grosso and Parravicini, 2013] explains how anharmonic effects can be used to introduce phenomena as melting, which make a stable structure unstable with a sufficient high temperature. In our study, we will observe the opposite situation: we will see how the introduction of anharmonic effects can effectively stabilize a structure, by turning an unstable harmonic system where phonon frequencies can be imaginary into a stable system in which all phonon frequencies are real. This requires a non perturbative approach that will be explained in Chapter 2.

Chapter 2

Stochastic methods for advanced calculations of electronic and vibrational properties

In the previous chapter we have illustrated the electronic problem and we have given some methods to attack it, approximating the electronic Hamiltonian. Furthermore, we have treated the problem of lattice vibrations and studied the phonon Hamiltonian, and the interactions between electrons and phonons. In this chapter we use stochastic methods to go beyond the approximations of Chapter 1 to treat the electronic and phonon problems.

In this chapter we will discuss Quantum Monte Carlo and SSCHA methods, which will be used to perform a significant part of the computations of the thesis. Both are based on stochastic methods.

We will start with a discussion of sampling in stochastic processes. The procedure of sampling is fundamental in our numerical methods, as it allows us to perform integrals numerically, by direct evaluation of the integrand at various points sampled from a probability distribution.

Next, we will discuss Quantum Monte Carlo methods, focusing on Variational Monte Carlo and Diffusion Monte Carlo. These will be our way to solve the electronic problem in strongly correlated systems where DFT may not be enough,

and will be useful in obtaining the ground state for the electronic part. As we will see, these methods rely on the choice of trial wavefunctions, and we will discuss in the successive section how to choose those trial wavefunctions in order to have good results with minimal computational cost.

Lastly, we will discuss the ionic part of the problem, with the self-consistent harmonic approximation (SCHA) and its stochastic implementation (SSCHA). This powerful technique allows us to obtain phonon bands for the system, including anharmonic effects that are out of reach of the classical methods based on the harmonic analysis described in Chapter 1.

2.1 Stochastic processes and sampling

The basis of all Quantum Monte Carlo (QMC) as well as SSCHA methods is the concept of stochastic sampling of a Hilbert space, which in principle is infinite dimensional. The Hilbert space represents the states for a system of N particles, whose positions are collectively described by a $3N$-dimensional vector $\boldsymbol{x}$. We will start this section with an example, understanding how to generate configurations for a simple one-dimensional system of a single particle, entirely described by the single real variable x. We will use iterative methods, in which we will denote as x_i the value of the coordinate at the $i-$th iteration. Throughout this first section, it will be possible to substitute the single coordinate iteration x with the analogue $3N$-dimensional vector $\boldsymbol{x}_i$: we choose to work in a one dimensional space for ease of explanation.

We will show more sophisticated sampling examples in the next section. For now, we analyse how to use random sequences in evaluating an integral of the form

$$I = \int_0^1 F(x)\mathrm{d}x, \tag{2.1.1}$$

where $F(x)$ is a known function. By defining a probability function $P(x)$ in the

interval $[0,1]$ that is close to $F(x)$*, we can rewrite the integral as

$$I = \int_0^1 \frac{F(x)}{P(x)} P(x) \mathrm{d}x. \tag{2.1.2}$$

If we can generate a sequence of N numbers x_i that is distributed according to $P(x)$, we can approximate the integral as

$$I \simeq \frac{1}{N} \sum_{i=1}^{N} \frac{F(x_i)}{P(x_i)} \pm \frac{\sigma}{\sqrt{N}}, \tag{2.1.3}$$

where the variance σ can be estimated through

$$\sigma^2 = \frac{1}{N-1} \sum_{i=1}^{N} \left(\frac{F(x_i)}{P(x_i)} - \left(\frac{1}{N} \sum_{j=1}^{N} \frac{F(x_j)}{P(x_j)} \right) \right)^2. \tag{2.1.4}$$

The variance measures the statistical fluctuations. For $P(x)$ as close as possible to $F(x)$, the variance tends to vanish. The difficulty in this procedure is to obtain sequences x_i distributed according to the probability $P(x)$: the procedure of building such sequences is called "sampling the distribution", and is the most concerning practical problem when performing Monte Carlo integrations.

We now introduce a pseudo-random process that can be used to sample a probability distribution $P(x)$, the process of Markov chains. The procedure requires a function G and a set of pseudo random numbers, that we denote as ξ_i, and gives as output a sequence x_i. We assume that the function only depends on two variables, and x_{i+1} only depends on the previous value x_i and the previous pseudo random number ξ_i as

$$x_{i+1} = G(x_i, \xi_i). \tag{2.1.5}$$

A very popular example of a Markov chain is the random walk, where ξ_i are restricted to be ± 1 and the function G is a simple sum: $x_{i+1} = x_n + \xi_n$. This can be useful to generate sequences that can be interpreted as positions of particles on a line. After a sequence is generated, we can check if the sequence is effectively distributed according to $P(x)$. In order to do that, we first define a distribution

*In equation (2.1.4), we can clarify what we mean by "close" by minimizing the variance. For now, we can assume that $P(x)$ is a probability distribution that is peaked where $F(x)$ is peaked.

function $P_i(x)$ that gives the probability distribution of x when the sequence has taken i iterations. Our goal is to have $P_i(x)$ approaching $P(x)$ for a large number of iterations: in order to do that, we can avoid accepting every outcome of the random walk, but instead control our outcome through an algorithm. We now propose a typical algorithm that is widely used [Becca and Sorella, 2017], the Metropolis algorithm.

At each step of the Metropolis algorithm starts from a given configuration and then makes a move. The move is then evaluated, and accepted or rejected according to a specific probability distribution. If the move is accepted, then the new point is added to the sequence and another move can be made, while if the move is rejected then we restart by proposing another movement from the previous point. To do so, we can build a conditional probability $\omega(x|x')$ that represents the possibility for getting to x from x' in a single move: we want to build this probability in order to satisfy the detailed balance condition

$$\omega(x'|x)P(x) = \omega(x|x')P(x') \tag{2.1.6}$$

This is not necessary but very convenient. In fact, it guarantees that the probability approximation P_i stays stable when we approach the goal probability $P(x)$, as

$$P_{i+1}(x) = \sum_{x'} \omega(x|x')P(x') = P(x)\sum_{x'} \omega(x'|x) = P(x) \tag{2.1.7}$$

if P_i has already reached the desired probability, $P(x) = 1$[†]. The rest of this section will be dedicated to illustrate how to build such a function.

First, we split ω in two pieces:

$$\omega(x'|x) = T(x'|x)A(x'|x), \tag{2.1.8}$$

where T is called the trial probability and can be chosen (we always choose it to be symmetric, $T(x|x') = T(x'|x)$) and A is denoted as acceptance probability. We can define A as

$$A(x'|x) = \min\Big\{1, \frac{P(x')T(x|x')}{P(x)T(x'|x)}\Big\} = \min\Big\{1, \frac{P(x')}{P(x)}\Big\}. \tag{2.1.9}$$

[†]In the third equality, we have used a normalization condition for ω: $\sum_{x'} \omega(x'|x) = 1$, as the probability to get anywhere from x is obviously 1.

Intuitively, A always accepts the move to x' if x' is more probable than x, and rejects it otherwise. ω now satisfies the detailed balance, as if $P(x') > P(x)$, then $A(x'|x) = 1$ and $A(x|x') = P(x)/P(x')$, implying

$$\omega(x|x')P(x') = T(x|x')A(x|x')P(x') = T(x'|x)A(x'|x)P(x) = \omega(x'|x)P(x). \tag{2.1.10}$$

Detailed balance holds, so we can generate numbers according to the probability distribution $P(x)$.

With all those tools, we now describe the Metropolis algorithm as follows:

- In the first step, we generate a configuration x' starting from an already known configuration x_i (if there is no already known configuration we take one number arbitrarily and start from there), according to $T(x'|x_n)$.

- Successively, we look at the acceptance: if $A(x'|x) = 1$ we always accept the move, while if not, we generate a random number $\eta \in [0, 1)$ distributed uniformly, and accept the move if $\eta < A(x'|x)$, reject it otherwise. If we accept, we take $x_{i+1} = x'$, if we reject we restart from the beginning. Successive iterations of the algorithms will generate a series distributed according to P_i, approaching P for large number of iterations. We have thus sampled the distribution.

2.2 Quantum Monte Carlo methods

In this section, we describe the application of Monte Carlo methods to the electronic problem in quantum mechanics, in particular to the computation of integrals appearing in the calculation of physical expectation values. Those methods will be useful for solving the electronic problem for strongly correlated systems. We will encounter two main methods: the Variational Monte Carlo (VMC) and the Diffusion Monte Carlo (DMC). We will conclude this section with an analysis of the errors that arise from this method.

The general problem is to compute $3N$-dimensional integrals (where N is the

number of variables, collectively indicated as $\boldsymbol{r}$ in this section)

$$\langle O \rangle = \frac{\int (\psi^{el}(\boldsymbol{r}, \boldsymbol{R}))^* O \psi^{el}(\boldsymbol{r}, \boldsymbol{R}) \mathrm{d}r}{\int (\psi^{el}(\boldsymbol{r}, \boldsymbol{R}))^* \psi^{el}(\boldsymbol{r}, \boldsymbol{R}) \mathrm{d}\boldsymbol{r}}, \tag{2.2.1}$$

where O is an observable and $\psi^{el}(\boldsymbol{r}, \boldsymbol{R})$ is an electronic wave function with fixed ion coordinates $\boldsymbol{R}$, and we will specify how to choose it. In our case, we will always take O to be the Hamiltonian of the system. In particular, we will choose O to be the electronic Hamiltonian (1.2.20).

2.2.1 Variational Monte Carlo

Averages through sampling

The VMC method is based on the variational principle, that is based on the fact that the energy levels are bound from below, and aims to compute the ground state and energy of the system. In this method, we use a trial wave function $\psi_T(\boldsymbol{r})$ in place of the electron wave function $\psi^{el}(\boldsymbol{r}, \boldsymbol{R})$ to estimate the ground state energy. This wavefunction can be expanded in terms of the (unknown) eigenfunctions of the Hamiltonian $\psi_i(\boldsymbol{r})$ as

$$\psi_T(\boldsymbol{r}) = \sum_i c_i \psi_i(\boldsymbol{r}), \tag{2.2.2}$$

in terms of complex coefficients c_i normalized as $\sum_i |c_i|^2 = 1$. The energy levels are given by $H_{el}\psi_i = E_i \psi_i$. The average of the energy on the wavefunction is

$$E_T = \langle \psi_T | H_{el} | \psi_T \rangle = \sum_{i,j} c_i^* c_j \langle \psi_i | H_{el} | \psi_j \rangle = \sum_i |c_i|^2 E_i. \tag{2.2.3}$$

As the energies are bound from below, there is an eigenvalue that is smaller than all others, E_0. Due to the fact that $|c_i|^2 < 1$, this implies that

$$E_T \geq E_0, \tag{2.2.4}$$

with the equality valid if and only if ψ_T is actually the ground state of the system. The VMC method then always provides an energy that is larger than the ground state energy of the system.

Due to the fact that we do not know the eigenvalues and eigenfunctions of the system, we have to find practical ways to compute the energy. Our goal is to compute the energy average E_T on a test wavefunction, and then optimize the wavefunction to improve the result. We start by showing how to compute E_T. Given a trial wavefunction ψ_T that we assume to know (usually through an ansatz), its energy can be computed as

$$E_T = \frac{\int (\psi_T(\boldsymbol{r}))^* H_{el} \psi_T(\boldsymbol{r}) \mathrm{d}\boldsymbol{r}}{\int (\psi_T(\boldsymbol{r}'))^* \psi_T(\boldsymbol{r}') \mathrm{d}\boldsymbol{r}'}. \tag{2.2.5}$$

We can manipulate this expression in order to use Monte Carlo methods to compute the integral. We divide and multiply in the integral in the numerator by $\psi_T(\boldsymbol{r})$, and then we insert the integral in the denominator inside the numerator. This gives us

$$E_T = \int \frac{|\psi_T(\boldsymbol{r})|^2}{\int |\psi_T(\boldsymbol{r}')|^2 \mathrm{d}\boldsymbol{r}'} \psi_T^{-1}(\boldsymbol{r}) H_{el} \psi_T(\boldsymbol{r}) \mathrm{d}\boldsymbol{r}. \tag{2.2.6}$$

We first note that

$$P(\boldsymbol{r}) = \frac{|\psi_T(\boldsymbol{r})|^2}{\int |\psi_T(\boldsymbol{r}')|^2 \mathrm{d}\boldsymbol{r}'} \tag{2.2.7}$$

is a non negative, normalized function[‡], so we can use it as a probability. Then (2.2.6) can be computed as the average of the so-called local energy

$$E_L(\boldsymbol{r}) = \psi_T^{-1}(\boldsymbol{r}) H_{el} \psi_T(\boldsymbol{r}), \tag{2.2.8}$$

with the probability $P(\boldsymbol{r})$ as the distribution for the average. This can be done through the Monte Carlo method: we sample a set of M points $\boldsymbol{r}_m$ from the probability distribution $P(\boldsymbol{r})$, and then compute the average $\langle E_L \rangle$ as

$$\langle E_L \rangle \sim \frac{1}{M} \sum_{m=1}^{M} E_L(\boldsymbol{r}_m). \tag{2.2.9}$$

The sampled points $\boldsymbol{r}_m$ are called walkers. In the limit $M \to \infty$ the average $\langle E_L \rangle$ tends to the energy E_T, and for finite M we have variance

$$\frac{\sigma^2}{M} \sim \frac{1}{M(M-1)} \sum_{m=1}^{M} (E_L(\boldsymbol{r}_m) - \langle E_L \rangle)^2. \tag{2.2.10}$$

[‡]While from the theoretical step this passage is trivial, from a computational point of view we will have to ensure that $P(\boldsymbol{r})$ remains positive and normalized during the optimization procedure.

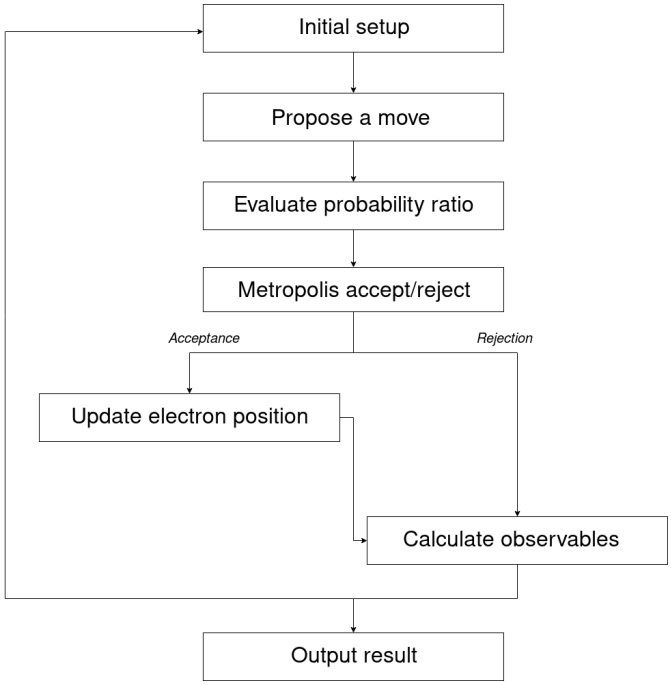

Figure 2.1: Acceptance-rejection Metropolis algorithm to generate samplings used to compute Monte Carlo averages.

Due to the fact that the trial energy E_T is the output of the method, we rename it as the ground-state VMC energy, E_0^{VMC}. We will use this terminology from now on.

For the sampling, we use the Markov chain with the Metropolis algorithm that we delineated in section 2.1. We choose a transition function $T(\boldsymbol{r}'|\boldsymbol{r})$ as the probability of the move from $\boldsymbol{r}$ to $\boldsymbol{r}'$, and use as acceptance

$$A(\boldsymbol{r}'|\boldsymbol{r}) = \min\left(1, \frac{T(\boldsymbol{r}'|\boldsymbol{r})P(\boldsymbol{r}')}{T(\boldsymbol{r}|\boldsymbol{r}')P(\boldsymbol{r})}\right) \tag{2.2.11}$$

In this procedure, T needs not be symmetric in its arguments. As shown, this procedure guarantees the detailed balance condition for $P(\boldsymbol{r})$ that reads

$$A(\boldsymbol{r}'|\boldsymbol{r})T(\boldsymbol{r}'|\boldsymbol{r})P(\boldsymbol{r}) = A(\boldsymbol{r}|\boldsymbol{r}')T(\boldsymbol{r}|\boldsymbol{r}')P(\boldsymbol{r}'). \tag{2.2.12}$$

We can then generate the samplings using the acceptance/rejection algorithm. We schematize this procedure in figure 2.1.

Optimization of the wavefunction

Until now, we have discussed the computation of averages assuming knowledge of the trial wavefunction ψ_T. This procedure is very ansatz dependent, as the choice of the wavefunction greatly affects the result. We now wish to go beyond the choice of an ansatz, discussing a method through which we can optimize our ansatz and improve our result. The optimization procedure relies on a set of parameters collectively denoted as $\{\alpha\}$. In this procedure, we can choose two quantities to optimize:

- we can choose to minimize the trial energy E_0^{VMC} (as the VMC energy is always greater than the true ground state energy), expressed in terms of the local energy as

$$E_0^{VMC}(\{\alpha\}) = \frac{\int |\psi_T(\boldsymbol{r}, \{\alpha\})|^2 E_L(\boldsymbol{r}, \{\alpha\}) \mathrm{d}\boldsymbol{r}}{\int |\psi_T(\boldsymbol{r}', \{\alpha\})|^2 \mathrm{d}\boldsymbol{r}'}, \tag{2.2.13}$$

  where $E_L(\boldsymbol{r}, \{\alpha\})$ has been defined in (2.2.8), adding the variational parameters $\{\alpha\}$ to the trial wave function,

- or we can minimize the energy variance, expressed as

$$\sigma^2(\{\alpha\}) = \frac{\int |\psi_T(\boldsymbol{r}, \{\alpha\})|^2 [E_L(\boldsymbol{r}, \{\alpha\}) - E_0^{VMC}(\{\alpha\})]^2 \mathrm{d}\boldsymbol{r}}{\int |\psi_T(\boldsymbol{r}', \{\alpha\})|^2 \mathrm{d}\boldsymbol{r}'}. \tag{2.2.14}$$

Note that all relevant quantities now have an explicit dependence on the parameters $\{\alpha\}$. The optimization of the variance has a distinct advantage with respect to the optimization of the energy: the variance is always bound from below by 0, while the bound for the energy is unknown (and the target of the computation). This approach has been introduced in [Umrigar et al., 1988], and further explored in [Filippi and Umrigar, 1996] and [Umrigar et al., 2007]. We will explore both methods. For our exposition, we will follow [Becca and Sorella, 2017]. In the rest of the exposition we will assume the trial wave function to be real, as will be common in practice.

Regarding the variance optimization, we can start from a known set of initial parameters $\{\alpha_0\}$, and rewrite the variance as

$$\sigma^2(\{\alpha\}) = \frac{\int \psi_T^2(\boldsymbol{r}, \{\alpha_0\}) w(\boldsymbol{r}, \{\alpha\}) [E_L(\boldsymbol{r}, \{\alpha\}) - E_0^{VMC}(\{\alpha\})]^2 \mathrm{d}\boldsymbol{r}}{\int \psi_T^2(\boldsymbol{r}', \{\alpha_0\}) w(\boldsymbol{r}, \{\alpha\}) \mathrm{d}\boldsymbol{r}'}, \tag{2.2.15}$$

where the additional factor $w(\boldsymbol{r},\{\alpha\})$ measures the difference of the configuration $\{\alpha\}$ from the initial configuration $\{\alpha_0\}$, and is written as

$$w(\boldsymbol{r},\{\alpha\}) = \frac{\psi_T^2(\boldsymbol{r},\{\alpha\})}{\psi_T^2(\boldsymbol{r},\{\alpha_0\})}. \tag{2.2.16}$$

We now sample a number M of walkers $\boldsymbol{r}_m$ starting from the probability distribution associated to $\psi_T(\boldsymbol{r},\{\alpha_0\})$ and compute this variance as

$$\sigma^2(\{\alpha\}) \sim \frac{\sum_{m=1}^{M} w(\boldsymbol{r}_m,\{\alpha\})[E_L(\boldsymbol{r}_m,\{\alpha\}) - E_0^{VMC}(\{\alpha\})]^2}{\sum_{m=1}^{M} w(\boldsymbol{r}_m,\{\alpha\})}. \tag{2.2.17}$$

Adjusting the parameters $\{\alpha\}$ in order to obtain an eigenstate of the energy, we obtain zero variance [Foulkes et al., 2001]. The aim then is to select parameters in order to minimize the quantity $\sigma^2(\{\alpha\})$ with respect to the parameters. This can be done using many numerical methods.

Regarding the energy optimization, the standard technique is to define energy derivatives as

$$f_k(\{\alpha\}) = -\frac{\partial E_0^{VMC}(\{\alpha\})}{\partial \alpha_k} = -\frac{\partial}{\partial \alpha_k}\frac{\langle\psi_T(\{\boldsymbol{\alpha}\})|\, H_{el}\, |\psi_T(\{\boldsymbol{\alpha}\})\rangle}{\langle\psi_T(\{\boldsymbol{\alpha}\}|\psi_T(\{\boldsymbol{\alpha}\}\rangle} \tag{2.2.18}$$

and then set those derivatives to 0 to find a stationary point for the energy. Under a variation $\delta\alpha$ of the $k-$th parameter, the trial wavefunction changes as

$$\psi_T(\boldsymbol{r},\{\alpha\}) \to \psi_T(\boldsymbol{r},\{\alpha\}) + \delta\alpha_k \frac{\partial \psi_T(\boldsymbol{r},\{\alpha\})}{\partial \alpha_k} + o(\delta\alpha_k^2). \tag{2.2.19}$$

In order to compute the derivatives of the energy f_k, we first define

$$O_k(\boldsymbol{r},\{\alpha\}) = \frac{1}{\psi_T(\boldsymbol{r},\{\alpha\})}\frac{\partial \psi_T(\boldsymbol{r},\{\alpha\})}{\partial \alpha_k}. \tag{2.2.20}$$

Then we define

$$|v_0(\{\alpha\})\rangle = \frac{|\psi_T(\{\alpha\})\rangle}{||\psi_T(\{\alpha\})||}, \tag{2.2.21}$$

$$\overline{O_k} = \langle v_0(\{\alpha\})|\, O_k\, |v_0(\{\alpha\})\rangle\,, \tag{2.2.22}$$

$$|v_k(\{\alpha\})\rangle = (O_k - \overline{O_k})\, |v_0(\{\alpha\})\rangle\,. \tag{2.2.23}$$

We note that the states $|v_k\rangle$ are orthogonal to $|v_0\rangle$, but not orthonormal in general[§]. Under the variation of the parameters, we have

$$|\psi_T(\{\alpha+\delta\alpha_k\})\rangle = (1+\delta\alpha_k O_k)\,|\psi_T\rangle\,. \tag{2.2.24}$$

By standard Taylor expansion in $\delta\alpha_k$, we can see that the norm of $|\psi_T\rangle$ changes as

$$\frac{1}{||\psi_T(\{\alpha+\delta\alpha_k\})||} = \frac{1}{||\psi_T||}(1-\delta\alpha_k\overline{O_k}). \tag{2.2.25}$$

The vector $|v_0\rangle$ then changes as

$$|v_0(\{\alpha+\delta\alpha_k\})\rangle = |v_0\rangle + \delta\alpha_k(O_k-\overline{O_k})\,|v_0\rangle = |v_0\rangle + \delta\alpha_k\,|v_k\rangle\,. \tag{2.2.26}$$

Now we can compute the variation of the energy:

$$\begin{aligned}\frac{\partial E_0^{VMC}}{\partial\alpha_k} &= \lim_{\delta\alpha_k\to 0}\frac{\langle v_0(\{\alpha+\delta\alpha_k\})|\,H_{el}\,|v_0(\{\alpha+\delta\alpha_k\})\rangle - \langle v_0|\,H_{el}\,|v_0\rangle}{\delta\alpha_k} = \\ &= 2\frac{\langle\psi_T|\,H_{el}(O_k-\overline{O_k})\,|\psi_T\rangle}{\langle\psi_T|\psi_T\rangle}.\end{aligned} \tag{2.2.27}$$

We can now insert a completeness relation to finally obtain

$$\begin{aligned}f_k &= -2\frac{\sum_{\boldsymbol{r}}\langle\psi_T|\,H^{el}\,|\boldsymbol{r}\rangle\,\langle\boldsymbol{r}|\,(O_k-\overline{O_k})\,|\psi_T\rangle}{\sum_{\boldsymbol{r}'}\langle\psi_T|\boldsymbol{r}'\rangle\,\langle\boldsymbol{r}'|\psi_T\rangle} = \\ &= -2\frac{\sum_{\boldsymbol{r}}E_L(\boldsymbol{r})(O_k-\overline{O_k})|\psi_T(\boldsymbol{r})|^2}{\sum_{\boldsymbol{r}'}|\psi_T(\boldsymbol{r}')|^2}.\end{aligned} \tag{2.2.28}$$

The last quantity can be computed using a sampling procedure from $\psi_T(\boldsymbol{r},\{\alpha\})$. Sampling M walkers $\boldsymbol{r}_m$, we finally obtain

$$f_k = -\frac{2}{M}\sum_{m=1}^{M}E_L(\boldsymbol{r}_m,\{\alpha\})(O_k(\boldsymbol{r}_m)-\overline{O_k}),\quad \overline{O}_k = \sum_{m=1}^{M}O_k(\boldsymbol{r}_m). \tag{2.2.29}$$

This concludes the derivation of the energy derivatives. The computed derivatives can now be used to look for a configuration of the parameters with f_k as near to 0 as possible.

[§]We will sometimes suppress the $\{\alpha\}$ dependence for brevity: unless explicitly stated, the absence of parameters is to be interpreted as evaluating the parameters at the configuration $\{\alpha\}$. Furthermore, we will denote the parameters under the variation of the $k-$th component by $\{\alpha+\delta\alpha_k\}$.

Lastly, we introduce a method to find a minimizing configuration, the method of steepest descent [Press et al., 2007]. Intuitively, this method instructs us to choose variations along the derivatives to follow the steepest descent path. By defining a small positive constant Δ, we take as variation

$$\delta\alpha_k = \Delta f_k. \tag{2.2.30}$$

In this way, the energy will change as (up to second order in Δ)

$$E_0^{VMC}(\{\alpha+\delta\alpha_k\}) - E_0^{VMC}(\{\alpha\}) = \sum_k \frac{\partial E_0^{VMC}}{\partial\alpha_k}\delta\alpha_k = -\delta\sum_k f_k^2 \leq 0. \tag{2.2.31}$$

The energy after variation will always be smaller than the energy before, so we approach a minimum of the energy. We have to pay attention to the fact that even if the parameter variation is small, the variation of the wavefunction can still be large: we need to find a quantity that measures this change in order to control it. For this, we introduce

$$\delta s^2 = \left|\left|\left|v_0(\{\alpha+\delta\alpha_k\})\right\rangle - \left|v_0(\{\alpha\})\right\rangle\right|\right|^2. \tag{2.2.32}$$

Using the known variation (2.2.26) we obtain that δs^2 is of order $\delta\alpha_k^2$, as

$$\delta s^2 = \sum_{k,k'}\left(\frac{\langle v_k|v_{k'}\rangle + \langle v_{k'}|v_k\rangle}{2}\right)\delta\alpha_k\delta\alpha_{k'} = \sum_{k,k'} S_{k,k'}\delta\alpha_k\delta\alpha_{k'}. \tag{2.2.33}$$

We can now use the approach of stochastic reconfiguration [Sorella, 2001]. Here we fix the value of δs^2 by using a Lagrange multiplier μ to minimize

$$\delta E_0^{VMC} + \mu\delta s^2 = -\sum_k f_k\delta\alpha_k + \mu\sum_{k,k'} S_{k,k'}\delta\alpha_k\delta\alpha_{k'}: \tag{2.2.34}$$

minimizing with respect to the variation, we obtain

$$\sum_{k'} S_{k,k'}\delta\alpha_{k'} = \frac{f_k}{2\mu}. \tag{2.2.35}$$

S is strictly positive definite, so it can be inverted in order to give $\delta\alpha_k$ in terms of f_k keeping the variation δs^2 under control, in terms of a Lagrange multiplier μ that we usually identify as $1/2\mu = \Delta$ to recover the earlier example. The matrix $S_{k,k'}$ can be computed by sampling, as

$$S_{k,k'} = \frac{1}{M}\sum_{m=1}^{M}(O_k(\boldsymbol{r}_m) - \overline{O_k})(O_{k'}(\boldsymbol{r}_m) - \overline{O_{k'}}). \tag{2.2.36}$$

We can now summarize the procedure: starting with a $\psi_T(\boldsymbol{r},\{\alpha\})$, the optimization procedure consists in

1. compute the f_k through the sampling procedure using (2.2.29);
2. if the forces are compatible with zero we already are at a minimum, else continue the algorithm;
3. decide a small step Δ;
4. using the sampling, compute the matrix S from (2.2.36);
5. invert the matrix S and use (2.2.34) to compute the $\delta\alpha$, also using $\Delta = 1/2\mu$;
6. recalculate the wave function ψ_T with the new parameters, and compute the f_k with the new parameters. If the f_k are compatible with zero we stop, else restart from the third point.

2.2.2 Diffusion Monte Carlo

Diffusion Monte Carlo (DMC) is a projective method that aims to compute the ground state energy of the system. This method connects the projection method with the statistical approach [Foulkes et al., 2001, Ceperley and Alder, 1980]. We will follow the exposition from [Foulkes et al., 2001].

The method starts from the Schrödinger equation in imaginary time

$$-\partial_\tau \Phi(\boldsymbol{r}, \tau) = (H_{el} - E_T)\Phi(\boldsymbol{r}, \tau), \tag{2.2.37}$$

where E_T is an energy offset to be fixed. From a boundary condition at time τ, the solution to this equation can be expressed as

$$\Phi(\boldsymbol{r}, \tau' + \tau) = \int G(\boldsymbol{r}|\boldsymbol{r}', \tau)\Phi(\boldsymbol{r}', \tau')\mathrm{d}\boldsymbol{r}', \tag{2.2.38}$$

where the function G is the Green function, given by

$$G(\boldsymbol{r}|\boldsymbol{r}', \tau) = \langle \boldsymbol{r}| \exp\left(-\tau(H_{el} - E_T)\right) |\boldsymbol{r}'\rangle , \tag{2.2.39}$$

solving the differential equation (2.2.37) with boundary condition $G(\boldsymbol{r}|\boldsymbol{r}', 0) = \delta(\boldsymbol{r} - \boldsymbol{r}')$. The eigenstates $|\Phi_i\rangle$ of the Hamiltonian can be used to decompose the time evolution operator as

$$\exp\left(-\tau H_{el}\right) = \sum_i \exp(-\tau(H_{el} - E_T)) |\Phi_i\rangle \langle\Phi_i| , \tag{2.2.40}$$

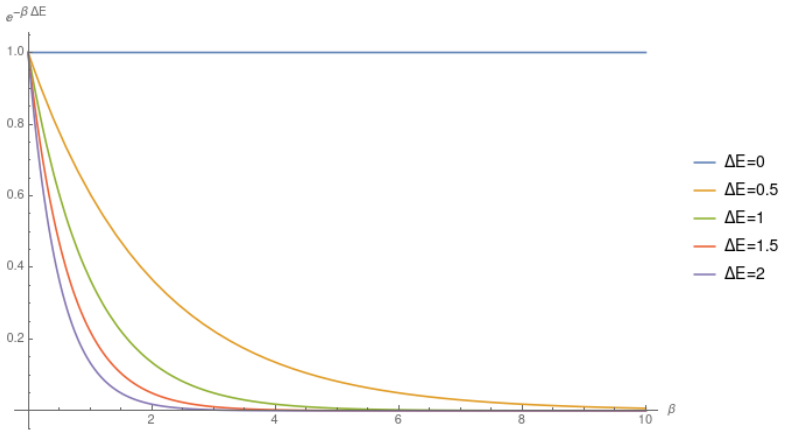

Figure 2.2: Limit for $\tau \to \infty$ of $\mathrm{e}^{-\tau\Delta E}$: all contributions with $\Delta E > 0$ are removed, and we are only left with the ground state for which $\Delta E = 0$. In the plot we have used arbitrary units for the energy.

so the Green function becomes

$$G(\boldsymbol{r}|\boldsymbol{r}',\tau) = \sum_i \Phi_i(\boldsymbol{r})\mathrm{e}^{-\tau(E_i - E_T)}\Phi_i^*(\boldsymbol{r}'). \tag{2.2.41}$$

At $\tau = 0$, the orthonormality condition of G is ensured by the completeness of the eigenvalues of the Hamiltonian. Assuming that the energy is bound from below and the energy minimum is E_0, we choose $E_T = E_0$. In the limit $\tau \to \infty$, all exponentials tend to zero for all i except $i = 0$: the contribution from the ground state is the only one surviving the limit. We illustrate this situation in figure 2.2.

As an example for the method, take a system of N free electrons in three dimensions. The imaginary time Schrödinger equation is

$$\partial_\tau \Phi(\boldsymbol{r},\tau) = \frac{1}{2}\sum_{i=1}^{N} \nabla_i^2 \Phi(\boldsymbol{r},\tau). \tag{2.2.42}$$

The Green function can be computed easily in this case: it is given by the Gaussian

$$G_F(\boldsymbol{r}|\boldsymbol{r}',\tau) = \frac{1}{(2\pi\tau)^{\frac{3N}{2}}} \exp\left(-\frac{|\boldsymbol{r}-\boldsymbol{r}'|^2}{2\tau}\right). \tag{2.2.43}$$

By substituting the wavefunction with a set of Dirac deltas peaked at some starting configurations, we can see this motion as a Brownian motion, in which the particles

diffuse from a set of starting conditions $\boldsymbol{R}_i$ at time 0. The correspondence is

$$\Phi(\boldsymbol{r}, 0) = \sum_{i=1}^{N} \delta(\boldsymbol{r} - \boldsymbol{R}_i), \tag{2.2.44}$$

and the evolved system is

$$\Phi(\boldsymbol{r}, \tau) = \sum_{i=1}^{N} G(\boldsymbol{r}|\boldsymbol{R}_i, \tau). \tag{2.2.45}$$

We can apply this to our sampling algorithm: we start from a configuration of Dirac deltas centred at points sampled from a probability distribution associated to a wavefunction, and then we can sample the evolved wavefunction in order to obtain a new distribution of particles. If we reach stabilization, the algorithm has successfully provided an approximation to the ground state wavefunction.

Obviously, in systems of interest we have a potential V. Computing the Green function of an interacting system is difficult in general, but by taking small time steps we can use a linear approximation. The full Green function can be obtained approximatively from the free Green function G_F as

$$G(\boldsymbol{r}|\boldsymbol{r}', \tau) = G_F(\boldsymbol{r}|\boldsymbol{r}', \tau) \underbrace{\exp\left(-\tau(V(\boldsymbol{r}) + V(\boldsymbol{r}') - 2E_T)/2\right)}_{P}. \tag{2.2.46}$$

The P factor incorporates the potential, and if the potential is large with respect to the ground state energy then the configuration is unlikely. P can be used to avoid unlikely configurations using an algorithm from [Reynolds et al., 1982]: after sampling of a new configuration starting from an initial configuration, if $P \geq 1$ the configuration can be unlikely, and we reject it with probability $1 - P$. If $P > 1$, we can take another sampling. This procedure is illustrated in figure 2.3 for a harmonic oscillator.

This procedure has a problem: we have assumed Φ to be a probability density function, but as real wavefunctions can be positive or negative, we can incur in issues whenever the wavefunction switches sign. As the nodes of the wavefunction can change during the procedure, we cannot simply switch the signs whenever it is negative. We need a more powerful method, that is provided by the fixed node approximation.

In the fixed node approximation, we make an ansatz on the nodes of the wavefunction and keep them fixed during the diffusion. Once we do that, we can divide

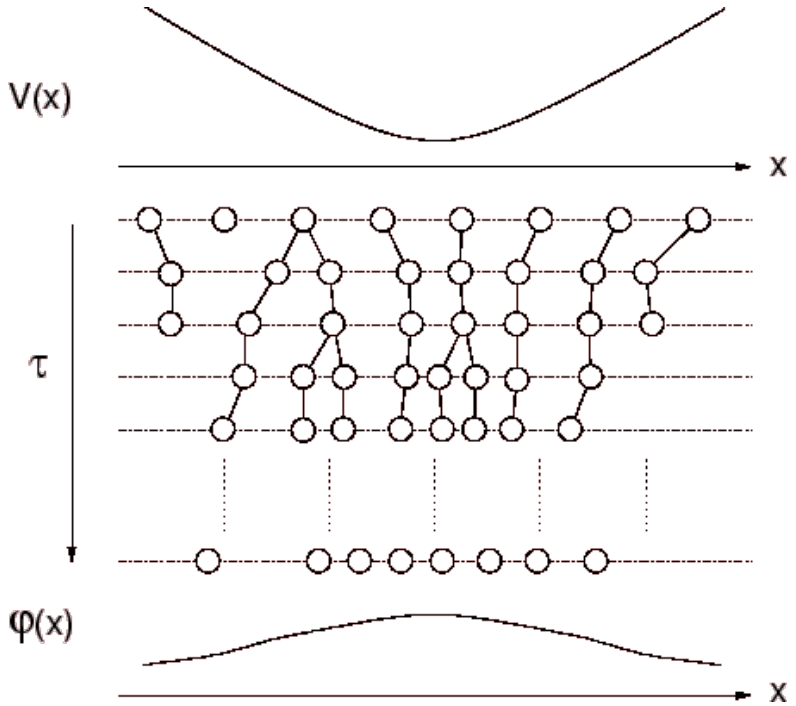

Figure 2.3: Evolution of walkers for DMC method for the harmonic oscillator. In the various vertical steps we are performing a step of our diffusion and sampling algorithm. With the diffusion, the walkers concentrate in positions where the wavefunction is peaked. At convergence, we obtain a good approximation of the ground state wave function of the harmonic oscillator. The image has been taken from [Foulkes et al., 2001].

the space of configurations in positive regions (where we use Φ as a probability density) and negative regions (where we use $-\Phi$). We keep walkers in their region of origin, not allowing them to go from positive to negative regions and vice versa, and we regulate E_T to keep the number of walkers approximatively constant. As the electron wavefunctions are antisymmetric, obvious zeroes happen whenever two walkers coincide: this is in general not sufficient to get all possible nodes, and we usually employ trial node surfaces (surfaces in the configuration space where the wavefunction vanishes), in particular we can use trial wavefunctions obtained from optimization procedure. In what follows, we will call pockets the disconnected regions of space that are limited by the nodal surface.

We now take a known trial wavefunction Φ_T to define the nodal surface. In each pocket v^α, we can find an eigenfunction for the Hamiltonian through the

described method, as there are no nodes in the pocket. We call this eigenfunction Φ_0^α, that vanishes outside of the pocket v^α. Inside the pocket, it solves

$$H_{el}\Phi_0^\alpha = E_0^\alpha \Phi_0^\alpha + \delta^\alpha, \tag{2.2.47}$$

where the constant δ^α accounts for the fact that Φ_0^α does not vanish at the borders of the pocket, but falls to 0 discontinuously. According to [Reynolds et al., 1982, Moskowitz et al., 1982], the energy E_0^α is always greater than the ground state energy E_0, giving an estimation by excess of the ground state energy in every pocket. When the trial nodal surface approaches the nodal surface of the real ground state, E_0^α approaches the ground state energy. The choice of a good trial wavefunction is then very important.

There is a last problem to solve with this procedure. The quantity P defined in (2.2.46) fluctuates wildly, which can give numerical instabilities. A method has been developed to account for this problem, the method of importance sampling [Reynolds et al., 1982, Ceperley and Kalos, 1979, Grimm and Storer, 1971]. Using the trial wavefunction Φ_T, we define $f(\boldsymbol{r},\tau) = \Phi(\boldsymbol{r},\tau)\Phi_T(\boldsymbol{r})$, which solves

$$-\partial_\tau f(\boldsymbol{r},\tau) = -\frac{1}{2}\nabla^2 f(\boldsymbol{r},\tau) + \nabla\cdot[\boldsymbol{v}_D(\boldsymbol{r})f(\boldsymbol{r},\tau)] + [E_L(\boldsymbol{r}) - E_T]f(\boldsymbol{r},\tau), \tag{2.2.48}$$

with

$$\boldsymbol{v}_D(\boldsymbol{r}) = \Phi_T(\boldsymbol{r})\nabla^{-1}\Phi_T(\boldsymbol{r}), \quad E_L(\boldsymbol{r}) = \Phi_T(\boldsymbol{r})^{-1}H_{el}\Phi_T(\boldsymbol{r}). \tag{2.2.49}$$

Here E_L is the familiar local energy, $\boldsymbol{v}_D$ is a new quantity, denoted as drift velocity. The Green function for (2.2.48) $\tilde{G}$ is related to the ordinary Green function G as

$$\tilde{G}(\boldsymbol{r}|\boldsymbol{r}',\tau) = \Phi_T(\boldsymbol{r})G(\boldsymbol{r}|\boldsymbol{r}',\tau)\Phi_T(\boldsymbol{r})^{-1}. \tag{2.2.50}$$

In the limit $t \to 0$, $\tilde{G}$ can be approximated as [Foulkes et al., 2001]

$$\tilde{G}(\boldsymbol{r}|\boldsymbol{r}',\tau) \sim G_d(\boldsymbol{r}|\boldsymbol{r}',\tau)G_b(\boldsymbol{r}|\boldsymbol{r}',\tau), \tag{2.2.51}$$

with

$$\begin{aligned} G_d(\boldsymbol{r}|\boldsymbol{r}',\tau) &= (2\pi t)^{-3N/2}\exp\left(-\frac{|\boldsymbol{r}-\boldsymbol{r}'-\tau\boldsymbol{v}_D(\boldsymbol{r}')|^2}{2t}\right), \\ G_b(\boldsymbol{r}|\boldsymbol{r}',\tau) &= \exp(-\tau(E_L(\boldsymbol{r}) + E_L(\boldsymbol{r}') - 2E_T)/2). \end{aligned} \tag{2.2.52}$$

G_d is a deformation of the free particle Green function that accounts for the drift velocity, while G_b plays the role of another P factor. Using this Green function, we obtain a higher density of walkers where $|\Phi_T|$ is increasing due to the drift velocity. When the trial wavefunction is chosen appropriately, the local energy fluctuates less than the potential V, and due to the additional drift velocity term there is little probability for the walkers to cross the nodal surface. The downside of the method is that small steps of τ are required, so the computational cost grows. We can further improve the method by using an acceptance-rejection mechanism due to [Reynolds et al., 1982,Ceperley et al., 1981]. As the Green function satisfies the detailed balance

$$\tilde{G}(\boldsymbol{r}|\boldsymbol{r}',\tau)\Phi_T(\boldsymbol{r}')^2 = \tilde{G}(\boldsymbol{r}'|\boldsymbol{r},\tau)\Phi_T(\boldsymbol{r})^2 \tag{2.2.53}$$

and G_b is symmetric under the $\boldsymbol{r} \leftrightarrow \boldsymbol{r}'$ exchange, we can define an acceptance

$$A(\boldsymbol{r}|\boldsymbol{r}') = \min\left(1, \frac{\tilde{G}(\boldsymbol{r}|\boldsymbol{r}',\tau)\Phi_T(\boldsymbol{r}')^2}{\tilde{G}(\boldsymbol{r}'|\boldsymbol{r},\tau)\Phi_T(\boldsymbol{r})^2}\right). \tag{2.2.54}$$

With this acceptance procedure the problematic configurations are discarded, and convergence is improved.

Lattice-Regularized Diffusion Monte Carlo

In applications to periodic systems, it is advantageous to use a modification of the DMC method, called Lattice-Regularized Diffusion Monte Carlo (LRDMC) [Casula et al., 2005]. For our exposition, we will follow [Becca and Sorella, 2017].

In LRDMC, we use a finite mesh with a lattice space: due to the fact that in most applications we have a spatial cutoff indicating the size of the system, this transforms the problem on the continuum in a discrete problem, with a finite number of lattice points. First, we introduce the approximated Laplacian ∇_a^2, acting on a function g as

$$\begin{aligned}\nabla_a^2 g(x,y,z) =& \frac{1}{a^2}(g(x+a,y,z)+g(x-a,y,z)-2g(x,y,z))+\\ &+\frac{1}{a^2}(g(x,y+a,z)+g(x,y-a,z)-2g(x,y,z))+\\ &+\frac{1}{a^2}(g(x,y,z+a)+g(x,y,z-a)-2g(x,y,z)).\end{aligned} \tag{2.2.55}$$

Here a is the parameter that indicates the finite lattice spacing, i.e. the minimum distance between two lattice sites. This deformed Laplacian goes to the standard Laplacian Δ^2 for $a \to 0$, the continuum limit.

We rewrite for convenience the Hamiltonian for a standard electronic problem, with electrons at coordinates $\boldsymbol{r}_i$ and ions at fixed coordinates $\boldsymbol{R}_I$. The Hamiltonian is given by (1.2.1), where we assume the ion-ion interaction to be constant and do not include it:

$$H_{el} = \sum_{i=1}^{N_e} \frac{\boldsymbol{p}_i^2}{2} - \sum_{i,I=1}^{N_e,N_{ion}} \frac{Z_I}{|\boldsymbol{r}_i - \boldsymbol{R}_I|} + \frac{1}{2} \sum_{i,j=1,i\neq j}^{N_e} \frac{1}{|\boldsymbol{r}_i - \boldsymbol{r}_j|}. \tag{2.2.56}$$

On the lattice, we perform quantization in a different way. Denoting as $\nabla^2_{a,i}$ the deformed Laplacian for the coordinate $\boldsymbol{r}_i$, we substitute $\boldsymbol{p}_i^2 \to -\nabla^2_{a,i}$. Furthermore, we modify the electron-ion interaction: in order to rule out unbounded negative energies, we cut the interaction off below a certain range as

$$\frac{1}{|\boldsymbol{r}_i - \boldsymbol{R}_I|} \to \frac{1}{\max(|\boldsymbol{r}_i - \boldsymbol{R}_i|, a)}. \tag{2.2.57}$$

The quantized deformed Hamiltonian is then

$$H_{el,a} = -\sum_{i=1}^{N_e} \frac{\nabla^2_{a,i}}{2} - \sum_{i,I=1}^{N_e,N_{ion}} \frac{Z_I}{\max(|\boldsymbol{r}_i - \boldsymbol{R}_i|, a)} + \frac{1}{2} \sum_{i,j=1,i\neq j}^{N_e} \frac{1}{|\boldsymbol{r}_i - \boldsymbol{r}_j|}. \tag{2.2.58}$$

The regularization of the potential brings an error no larger than $o(a^2)$, as the region where the potential has been modified has volume of order a^3 and the modification is of order a^{-1}.

We can employ fixed-node techniques with this Hamiltonian, using the advantage of lattice regularization that allows us to write a finite number of matrix elements for the Hamiltonian, and then recover the original problem in the limit $a \to 0$. While in theory this procedure is straightforward, in actual practice the error is large, and a very small value of a is needed for convergence. We will now show how to improve convergence with an alternative method.

In this method, we build an alternative Hamiltonian $\mathcal{H}^a$, whose kinetic term is still the modified Laplacian $\nabla_{i,a}$, but we modify the potential in order to have

$$\frac{\langle \boldsymbol{r}_i | \, H_{el} \, | \psi_T \rangle}{\langle \boldsymbol{r}_i | \psi_T \rangle} = \frac{\langle \boldsymbol{r}_i | \, \mathcal{H}^a \, | \psi_T \rangle}{\langle \boldsymbol{r}_i | \psi_T \rangle}. \tag{2.2.59}$$

We are here requiring that the local energy computed with the standard Hamiltonian has to be equal to the local energy computed with the modified Hamiltonian, using the trial wavefunction ψ_T (as the computation is made on a discrete, finite lattice, there is only a finite number of such matrix elements). If we denote as $V(\boldsymbol{r})$ the potential of (2.2.56), what we are doing is defining the potential of $\mathcal{H}^a$ as

$$\tilde{V}^a(\boldsymbol{r}) = V(\boldsymbol{r}) + \frac{(\nabla_a^2 - \nabla)\psi_T(\boldsymbol{r})}{2\psi_T(\boldsymbol{r})}. \tag{2.2.60}$$

This modified potential correctly goes to the unmodified potential for $a \to 0$. This was proposed in [Casula et al., 2005], giving very stable computations for bosonic systems. Unfortunately, in the case at hand, we can still have unbound ground state energies, but we can regularize this in the following way: focusing on the electron-ion interaction (that is responsible for the unbound ground state energy), that we define as in (1.2.2), we first replace the potential $V_{ext}(\boldsymbol{r}_i)$ as in (2.2.60),

$$\tilde{V}_{ext}^a(\boldsymbol{r}_i) = V_{ext}(\boldsymbol{r}_i) - \frac{(\nabla_{a,i}^2 - \nabla_i)\psi_T(\boldsymbol{r})}{2\psi_T(\boldsymbol{r})}, \tag{2.2.61}$$

and then we redefine the $V_{ext}(\boldsymbol{r}_i)$ inside $\tilde{V}_{ext}^a(\boldsymbol{r}_i)$ as

$$V_{ext}^a(\boldsymbol{r}_i) = -\sum_{I=1}^{N_{ion}} \frac{Z_I}{\max(|\boldsymbol{r}_i - \boldsymbol{R}_I|, a)}, \tag{2.2.62}$$

and taking the final potential to be

$$\tilde{V}_{ext}^{a,\min} = \min\left(V_{ext}^a, \tilde{V}_{ext}^a\right). \tag{2.2.63}$$

With this potential, we can avoid the problem of unbound ground state and use lattice computations that are more stable. The final Hamiltonian that is used in LRDMC is then

$$H_{el,a} = -\sum_{i=1}^{N_e} \frac{\nabla_{a,i}^2}{2} + \tilde{V}_{ext}^{a,min} + \frac{1}{2}\sum_{i,j=1,i\neq j}^{N_e} \frac{1}{|\boldsymbol{r}_i - \boldsymbol{r}_j|}. \tag{2.2.64}$$

2.3 Trial wavefunctions

In the previous section, we have seen that the Quantum Monte Carlo methods heavily rely on the choice of an initial ansatz. With a good ansatz, we can improve

the results and obtain a good result at a lower computational cost. For this reason, trial wavefunctions have been extensively studied in literature. In this section, we will introduce the trial wavefunctions that we use in our work.

2.3.1 Basis sets: atomic and molecular orbitals

The first important distinction to make is between atomic and molecular orbitals. From an intuitive point of view, atomic orbitals are wavefunctions centred on particular nuclei of the lattice, and describe electrons bound to a particular lattice site, while molecular orbitals are linear combinations of atomic orbitals, describing electrons distributed on the lattice.

For atomic orbitals centred at a position $\boldsymbol{R}_I$, we have to specify their total angular momentum l and the projection on an axis, m. Examples of such orbitals are the Slater and Gaussian orbitals, defined as

$$\phi^{\text{Gaussian}}_{l,\pm|m|,I}(\mathbf{r},\xi) \propto |\mathbf{r}-\mathbf{R}_I|^l \mathrm{e}^{-\xi|\mathbf{r}-\mathbf{R}_I|^2}[Y_{l,m,I}(\Omega) \pm Y_{l,-m,I}(\Omega)]; \tag{2.3.1}$$

$$\phi^{\text{Slater}}_{l,\pm|m|,I}(\mathbf{r},\xi) \propto |\mathbf{r}-\mathbf{R}_I|^l \mathrm{e}^{-\xi|\mathbf{r}-\mathbf{R}_I|}[Y_{l,m,I}(\Omega) \pm Y_{l,-m,I}(\Omega)], \tag{2.3.2}$$

with $Y_{l,m,I}$ spherical harmonics centred at a particular $\boldsymbol{R}_I$, and Ω collectively indicating angular spherical coordinates centred at $\boldsymbol{R}_I$. Here ξ is a parameter that can be used for variations. A generic atomic orbital is then written as

$$\phi_I(\boldsymbol{x},\xi) = \sum_{l,m} c_{l,m,I}\phi^X_{l,m,I}(\boldsymbol{x},\xi), \tag{2.3.3}$$

where X is a label for the type of radial wavefunction that we use. The coefficients c are other parameters that can be used for variations. In practical applications, some parameters are fixed by requiring certain shapes for the atomic orbitals, and the variation happens at the molecular level.

Molecular orbitals are linear combinations of atomic orbitals centred around different nuclei, which describe electrons shared by the whole lattice. Mixing atomic orbitals of determined shapes will give greater variational freedom to our system, while keeping the properties of the system under control. For an easy example, consider a set of two normalized atomic orbitals $|\phi_1\rangle$ and $|\phi_2\rangle$, centred around $\boldsymbol{R}_1$ and $\boldsymbol{R}_2$ respectively. Generalization to an arbitrary number of orbitals

is obvious. The different orbitals will have an overlap, that we denote as $S_{12} = \langle\phi_1|\phi_2\rangle$. We can make a pair of normalized molecular orbitals as

$$|\psi_1\rangle = \frac{1}{\sqrt{1+t^2+2tS_{12}}}(|\phi_1\rangle + t\,|\phi_2\rangle), \tag{2.3.4}$$

$$|\psi_2\rangle = \frac{1}{\sqrt{1+u^2-2uS_{12}}}(|\phi_2\rangle - u\,|\phi_1\rangle). \tag{2.3.5}$$

Here t and u are variational parameters, but with a constraint: in order to have orthogonal wavefunctions, we have to impose

$$u = \frac{t+S_{12}}{1+tS_{12}}. \tag{2.3.6}$$

In the general case, we will have a large number N of atomic orbitals, which we can mix with an $N\times N$ matrix of coefficients that can be used as variational coefficients. Those coefficients are not all independent, as many are fixed by conditions of orthonormality.

2.3.2 Jastrow factor

In writing a trial wavefunction, singularities can often be encountered. When pairs of electrons become very near or an electron gets very near to a nucleus, large numbers appear in the computation, introducing various numerical difficulties. A method to avoid those large numbers is to manually fix the values for the wavefunction around singularities, using prefactors called Jastrow factors to impose the so-called cusp conditions. In this subsection, we will first introduce the cusp conditions and then show how to use Jastrow factors to impose the cusp conditions and smoothen computations significantly. Cusp conditions were studied in [Kato, 1957], which we follow for the exposition.

There are three types of singularities that are encountered in a typical electronic problem: singularities where an electron approaches a nucleus, singularities where two electrons of same spin are very near, and singularities where two electrons of opposite spin are very near[¶]. These three cases will need different treatments.

[¶]As spins for two particles are in superposition, by "opposite spin" we mean a singlet spin state that is antisymmetric under spin exchange, while by "same spin" we mean a triplet state that is symmetric under spin exchange.

- For an electron-nucleus singularity, where an electron at position $\boldsymbol{r}_i$ approaches a nucleus at position $\boldsymbol{R}_I$, the Hamiltonian can be written in terms of the variable $r_{iI} = |\boldsymbol{r}_i - \boldsymbol{R}_I|$ as

$$\left(-\frac{1}{2}\nabla_i^2 - \frac{Z_I}{r_{iI}} + ...\right)\psi = E\psi. \tag{2.3.7}$$

  Here we consider only the terms describing the motion of the electron and the interaction with the nucleus. In terms of the spherical coordinate r_{iI}, we have to eliminate the singularity $1/r_{iI}$: this can be done by imposing the wavefunction condition

$$\frac{\psi'(r_{iI})}{\psi(r_{iI})} \to -Z_I, \tag{2.3.8}$$

  for $r_{iI} \to 0$.

- For electrons of opposite spin, the orbital part of the wavefunction has to be symmetric under the exchange of $\boldsymbol{r}_i$ with $\boldsymbol{r}_j$. In terms of the variable $r_{ij} = |\boldsymbol{r}_i - \boldsymbol{r}_j|$, the relevant part of the Hamiltonian is

$$\left(-\nabla_i^2 - \nabla_j^2 + \frac{1}{2}r_{ij} + ...\right)\psi = E\psi. \tag{2.3.9}$$

  The singularity is similar to the previous case, so the condition is

$$\frac{\psi'(r_{ij})}{\psi(r_{ij})} \to \frac{1}{2}, \tag{2.3.10}$$

  where the 1/2 factor comes from the fact that both electrons move, so we have to use the reduced mass of the system.

- Lastly, in the case where the two electrons have same spin, the wavefunction has to be antisymmetric upon coordinate exchange. This is similar to the previous case, with an additional factor of 1/2:

$$\frac{\psi'(r_{ij})}{\psi(r_{ij})} \to \frac{1}{4}. \tag{2.3.11}$$

  This case can actually be neglected, due to the Pauli exclusion principle that impedes electrons of same spin to occupy the same spot, creating a repulsive force that makes the configuration unlikely [Casula and Sorella, 2003].

The cusp conditions are implemented by splitting the trial wave function multiplicatively in two parts. The Jastrow factor is a factor only containing orbital coordinates that is symmetric under their exchange, so it can be multiplied to an antisymmetric wavefunction in order to make the total wavefunction antisymmetric under coordinate exchange. The total trial wavefunction is written as

$$\psi_T(\boldsymbol{r}) = J(\boldsymbol{r})\Phi_T(\boldsymbol{r}), \tag{2.3.12}$$

where we will study possibilities for Φ_T in the next subsection and J is the Jastrow factor, written as

$$J(\boldsymbol{r}) = \exp\left(\sum_{i<j} u(\boldsymbol{r}_i, \boldsymbol{r}_j)\right), \tag{2.3.13}$$

where the function u is symmetric. This function is written as

$$u(\boldsymbol{r}, \boldsymbol{r}') = \frac{u_{ei}(\boldsymbol{r}) + u_{ei}(\boldsymbol{r}')}{N_e - 1} + u_{ee}(\boldsymbol{r}, \boldsymbol{r}'), \tag{2.3.14}$$

with the factor $N_e - 1$ for normalization, to have

$$\sum_{i<j} \frac{u_{ei}(\boldsymbol{r}_i) + u_{ei}(\boldsymbol{r}_j)}{N_e - 1} = \sum_i u_{ei}(\boldsymbol{r}_i). \tag{2.3.15}$$

The factor u_{ei} imposes electron-nucleus cusp conditions, while u_{ee} imposes electron-electron cusp conditions. They can be written in terms of the atomic orbitals as

$$u_{ei}(\mathbf{r}) = u_{ei}^{\text{cusp}}(\mathbf{r}) + \sum_I s_I \phi_I(\mathbf{r}), \tag{2.3.16}$$

$$u_{ee}(\mathbf{r}, \mathbf{r}') = u_{ee}^{\text{cusp}}(\mathbf{r}, \mathbf{r}') + \sum_{I,J} u_{I,J}\phi_I(\mathbf{r})\phi_J(\mathbf{r}'). \tag{2.3.17}$$

The terms labelled with cusp give the cusp conditions, and are written as

$$u_{ei}^{\text{cusp}}(\mathbf{r}) = -\sum_I \frac{Z_I|\mathbf{r} - \mathbf{R}_I|}{1 + \sqrt{2Z_I}b_{ei}}, \tag{2.3.18}$$

$$u_{ee}^{\text{cusp}}(\mathbf{r}, \mathbf{r}') = \frac{|\mathbf{r} - \mathbf{r}'|}{2(1 + b_{ee}|\mathbf{r} - \mathbf{r}'|)}. \tag{2.3.19}$$

It is easy to prove now that with those cusp terms the cusp conditions (2.3.8),(2.3.10) are met. The parameters s_I, $u_{I,J}$ (symmetric under $I \leftrightarrow J$ exchange), b_{ei} and b_{ee} are all variational parameters, not affecting the computation of the cusp conditions, and can be left free during the optimization.

2.3.3 The antisymmetrical part

Having understood how to incorporate cusp conditions in order to remove problematic configurations, we can now proceed to the last point, determining forms for the antisymmetrical part $\Phi_T(\boldsymbol{r})$. In what follows, we will have to consider both spatial and orbital coordinates, so we will indicate with $\boldsymbol{r}_i$ and χ_i the position and spin variable of the $i-$th particle, but we will keep indicating with $\boldsymbol{r}$ the set of all possible orbital and spin coordinates of the system. The first possibility for $\Phi_T(\boldsymbol{r})$ is a Slater determinant: we first pick N_e atomic orbitals ϕ_I, and define the Slater wavefunction as

$$\Phi_T(\boldsymbol{r}) = \frac{1}{\sqrt{N_e!}} \det \begin{pmatrix} \phi_1(\boldsymbol{r}_1)\chi_1 & \dots & \phi_{N_e}(\boldsymbol{r}_1)\chi_1 \\ \vdots & \dots & \vdots \\ \phi_1(\boldsymbol{r}_{N_e})\chi_{N_e} & \dots & \phi_{N_e}(\boldsymbol{r}_{N_e})\chi_{N_e} \end{pmatrix}. \tag{2.3.20}$$

This wavefunction is explicitly antisymmetric under coordinate exchange due to the determinant. This wavefunction has the advantage of allowing any spin configuration, due to the fact that the χ_i can be chosen arbitrarily, but does not describe situations in which electrons are strongly correlated due to the fact that it heavily employs single-particle orbitals, and the only possible optimization consists in choosing different orbitals.

In order to go around this limitation, we introduce the antisymmetrical geminal power (AGP) wavefunction, in which a pairing function f is defined for two electrons, and then a total determinant is taken. From now on, we will assume to have an even number of electrons in the system. In this approach, we define a pairing function

$$\begin{aligned} f(\boldsymbol{r}_1\chi_1, \boldsymbol{r}_2\chi_2) =& \frac{1}{\sqrt{2}}(|\uparrow\downarrow\rangle - |\downarrow\uparrow\rangle) f_+(\boldsymbol{r}_1, \boldsymbol{r}_2) + \\ &+ \frac{1}{\sqrt{2}}(|\uparrow\downarrow\rangle + |\downarrow\uparrow\rangle) f_-(\boldsymbol{r}_1, \boldsymbol{r}_2) + \\ &+ |\uparrow\uparrow\rangle\, f_\uparrow(\boldsymbol{r}_1, \boldsymbol{r}_2) + |\downarrow\downarrow\rangle\, f_\downarrow(\boldsymbol{r}_1, \boldsymbol{r}_2), \end{aligned} \tag{2.3.21}$$

where the orbital pairing functions $f_-, f_\uparrow, f_\downarrow$ are antisymmetric under exchange of arguments and f_+ is symmetric, to satisfy the Pauli principle. All those pairing functions can be expressed as quadratic combinations of molecular orbitals ϕ_μ (where the index μ runs over the number of chosen molecular orbitals) as

$$f_\sigma(\boldsymbol{r}, \boldsymbol{r}') = \sum_{\mu,\nu} M^{(\sigma)}_{\mu,\nu} \phi_\mu(\boldsymbol{r}) \phi_\nu(\boldsymbol{r}'). \tag{2.3.22}$$

The matrices $M^{(\sigma)}_{\mu,\nu}$ (with $\sigma = +, -, \uparrow, \downarrow$) are symmetric or antisymmetric according to the symmetry of f_σ. In the AGP case, we reduce to the singlet configuration, setting $f_- = f_\uparrow = f_\downarrow = 0$. We can then make a wavefunction by

$$\Phi_{\text{AGP}} = \det \begin{pmatrix} f_+(\boldsymbol{r}_1 \uparrow, \boldsymbol{r}_{\frac{N_e}{2}+1} \downarrow) & f_+(\boldsymbol{r}_1 \uparrow, \boldsymbol{r}_{\frac{N_e}{2}+2} \downarrow) & \dots & f_+(\boldsymbol{r}_1 \uparrow, \boldsymbol{r}_{N_e} \downarrow) \\ f_+(\boldsymbol{r}_2 \uparrow, \boldsymbol{r}_{\frac{N_e}{2}+1} \downarrow) & f_+(\boldsymbol{r}_2 \uparrow, \boldsymbol{r}_{\frac{N_e}{2}+2} \downarrow) & \dots & f_+(\boldsymbol{r}_2 \uparrow, \boldsymbol{r}_{N_e} \downarrow) \\ \vdots & \vdots & \ddots & \vdots \\ f_+(\boldsymbol{r}_{\frac{N_e}{2}} \uparrow, \boldsymbol{r}_{\frac{N_e}{2}+1} \downarrow) & f_+(\boldsymbol{r}_{\frac{N_e}{2}} \uparrow, \boldsymbol{r}_{\frac{N_e}{2}+2} \downarrow) & \dots & f_+(\boldsymbol{r}_{\frac{N_e}{2}} \uparrow, \boldsymbol{r}_{N_e} \downarrow) \end{pmatrix}. \tag{2.3.23}$$

Here we have set the first $N_e/2$ electrons to up spin and the second $N_e/2$ electrons to down spin. The resulting wavefunction depends on the variational parameters $M^{(+)}_{\mu,\nu}$, independent of the spin pairing. This wavefunction has a relatively low computational cost, but it is constrained as it only describes singlet pairings.

The most powerful pairing technique that allows all spins to be described is the Pfaffian wavefunction [Genovese et al., 2020]. This is obtained by turning on all possible pairings in (2.3.21). As in the Slater case, all possible spins are allowed, but we keep the predictive power of the paired electrons. This wavefunction can be used to describe systems with non zero magnetic momentum, that can be used as order parameter to distinguish magnetic phases. The disadvantage is obviously in the high computational cost. The Pfaffian wavefunction is defined by first building the $2n \times 2n$ antisymmetric matrix W given by

$$W = \begin{pmatrix} 0 & f(\boldsymbol{r}_1 \uparrow, \boldsymbol{r}_2 \uparrow) & \dots & f(\boldsymbol{r}_1 \uparrow, \boldsymbol{r}_{\frac{N_e}{2}+1} \downarrow) & \dots & f(\boldsymbol{r}_1 \uparrow, \boldsymbol{r}_{N_e} \downarrow) \\ f(\boldsymbol{r}_2 \uparrow, \boldsymbol{r}_1 \uparrow) & 0 & \dots & f(\boldsymbol{r}_2 \uparrow, \boldsymbol{r}_{\frac{N_e}{2}+1} \downarrow) & \dots & f(\boldsymbol{r}_2 \uparrow, \boldsymbol{r}_{N_e} \downarrow) \\ \vdots & \vdots & \ddots & \vdots & \ddots & \vdots \\ f(\boldsymbol{r}_{N_e} \downarrow, \boldsymbol{r}_1 \uparrow) & f(\boldsymbol{r}_{N_e} \downarrow, \boldsymbol{r}_2 \uparrow) & \dots & f(\boldsymbol{r}_{N_e} \downarrow, \boldsymbol{r}_{\frac{N_e}{2}+1} \downarrow) & \dots & 0 \end{pmatrix}. \tag{2.3.24}$$

We then compute the Pfaffian of the matrix as

$$\text{Pf}(W) = \sum_\alpha \text{sign}(\alpha) \sum_{k=1}^{\frac{N_e}{2}} W_{i_k, j_k}, \tag{2.3.25}$$

where all i_k and j_k are different, $i_k < j_k$ for each k, $i_1 < i_2 < ... < i_{N_e}$ and α are permutations of the pairs $\{(i_1, j_1), ..., (i_{N_e}, j_{N_e})\}$, with $\text{sign}(\alpha)$ indicating the

sign of the permutation. The Pfaffian of W is equal to the square root of the determinant of W, up to the sign. The Pfaffian wavefunction is then defined as

$$\Phi_{\text{Pfaffian}} = \text{Pf}(W). \tag{2.3.26}$$

As stated, this wavefunction is the most general pairwise wavefunction, with the downside of having a high computational cost.

2.4 SSCHA method and software

Up to now, we have described how to attack the electron problem, and in this section we treat the ion problem. We will introduce the Self-Consistent Harmonic Approximation (SCHA) and its stochastic implementation (SSCHA) [Errea et al., 2014, Errea et al., 2013], in order to go beyond the harmonic approximation and include anharmonic contributions in our computations of phonons. The use of this approach will allow us to introduce anharmonic effects in the computation of the phonon bands as well as in the atomic positions. In this section, we will mainly follow [Monacelli et al., 2021] and [Bianco et al., 2017].

In the Born-Oppenheimer approximation, the phonons computed at the harmonic level are non interacting quasiparticles, and if anharmonic effects are not strong, perturbation theory can be used to include them. This is not the case for the systems that we will study, so we need to develop an alternative approach.

In order to describe the SCHA, we start from the Born-Oppenheimer Hamiltonian for the ionic degrees of freedom, that we write here as

$$H_{ion,BO} = \sum_{I=1}^{N_{ion}} \frac{\boldsymbol{P}_I^2}{2M_I} + E^{el}(\boldsymbol{R}), \tag{2.4.1}$$

where $E^{el}(\boldsymbol{R})$ is the Born-Oppenheimer potential from the first chapter, including the ion-ion contribution and the electron-ion contribution. We drop here the subscript in $H_{ion,BO}$ for brevity: we will always refer to the BO Hamiltonian for ions with H in this subsection. We work at a fixed temperature T and define the density matrix of the system as (here $\beta = 1/T$, in units $k_B = 1$)

$$\rho = \mathrm{e}^{-\beta H} / \operatorname{tr}\left(\mathrm{e}^{-\beta H}\right), \tag{2.4.2}$$

so the free energy of the system can be computed as

$$F = \mathrm{tr}[\rho H] + \frac{1}{\beta}\,\mathrm{tr}[\rho \ln \rho]. \tag{2.4.3}$$

This quantity is often very complicated to compute. We can create a variational problem out of this definition, by defining the functional

$$\mathcal{F}[\tilde{\rho}] = \mathrm{tr}[\tilde{\rho} H] + \frac{1}{\beta}\,\mathrm{tr}[\tilde{\rho} \ln \tilde{\rho}], \tag{2.4.4}$$

where now $\tilde{\rho}$ can be an arbitrary matrix. We can then use the Gibbs-Bogoliubov (GB) variational principle [Isihara, 1968], which states that the true free energy of the system is the minimum value of (2.4.4): analogously to (2.2.4), we have

$$.\mathcal{F}[\tilde{\rho}] \geq F. \tag{2.4.5}$$

The problem has now become a variational problem, in which we will minimize (2.4.4) by using trial density matrices. This equation is analogous to equation (2.2.4) for the electrons, but defines a variational problem for the ions at any temperature, including quantum effects also at 0 K.

We will use lowercase indexes from the start of Latin alphabet as a and b to run over the number of ions and the three degrees of spatial freedom (so those indexes run from 1 to $3N_{ion}$). We define the trial harmonic Hamiltonian $\tilde{H}_{\mathcal{R},\mathbf{\Phi}}$ in terms of two sets of variational parameters: a vector $\mathcal{R}$ of dimension $3N_{ion}$ (called centroids) and a $3N_{ion} \times 3N_{ion}$ positive definite symmetric matrix Φ_{ab} (the force constants) as[‖]

$$\begin{aligned} \tilde{H}_{\mathcal{R},\mathbf{\Phi}} &= \sum_{a=1}^{3N_{ion}} \frac{P_a^2}{2M_a} + \tilde{E}^{el}_{\mathcal{R},\mathbf{\Phi}}, \\ \tilde{E}^{el}_{\mathcal{R},\mathbf{\Phi}} &= \frac{1}{2} \sum_{a,b=1}^{3N_{ion}} \Phi_{ab} (R - \mathcal{R})^a (R - \mathcal{R})^b. \end{aligned} \tag{2.4.6}$$

The density matrix of this harmonic system is given by

$$\tilde{\rho}_{\mathcal{R},\mathbf{\Phi}} = \mathrm{e}^{-\beta \tilde{H}_{\mathcal{R},\mathbf{\Phi}}} / \,\mathrm{tr}\Big(\mathrm{e}^{-\beta \tilde{H}_{\mathcal{R},\mathbf{\Phi}}}\Big). \tag{2.4.7}$$

[‖] We define M_a in such a way that it ignores the spatial coordinate: $M_a = M_I$ whenever a is indicating any coordinate describing the $I-$th nucleus.

We have substituted the difficult problem of computing the density matrix for a system with a complicated potential to the easier problem of computing the density matrix for an harmonic system, at the cost of introducing variational parameters. While some components of $\mathbf{\Phi}$ can be restricted by imposing the symmetries of the system, we will have a large number of parameters to vary. This is where the analogy of this method with VMC is evident, as we have traded the problem of computing complicated objects (wave functions in VMC and density matrix here) with the problem of computing variational parameters in order to minimize certain functions (trial energy or energy variance in VMC, free energy here). The difference with VMC is that here we are working with phonons, obtaining the quantities of interest for the ion problem.

With the density matrix, we can define the averages of operators as

$$\langle O \rangle_{\tilde{\rho}_{\mathcal{R},\mathbf{\Phi}}} = \mathrm{tr}(O\tilde{\rho}_{\mathcal{R},\mathbf{\Phi}}). \tag{2.4.8}$$

We will focus on operators that only depend on the position. For those, the averages can be taken in a simplified way. First, we define

$$\Gamma_{ab} = \sqrt{M_a M_b} \sum_p \frac{2\tilde{\omega}_p}{(1+2n_p)} \tilde{A}^a_p \tilde{A}^b_p, \tag{2.4.9}$$

where $\tilde{\omega}_p$ and $\tilde{A}^a_p$ are the eigenvalues and eigenvectors for the harmonic dynamical matrix $\Phi_{ab}/\sqrt{M_a M_b}$, and n_p is the Bose-Einstein occupation

$$n_p = \frac{1}{\mathrm{e}^{\beta\omega_p} - 1}. \tag{2.4.10}$$

Then we can define the Gaussian ionic probability distribution function $\tilde{\rho}_{\mathcal{R},\mathbf{\Phi}}$ as

$$\tilde{\rho}_{\mathcal{R},\mathbf{\Phi}}(\boldsymbol{R}) = \sqrt{\det\left\{\frac{\Gamma}{2\pi}\right\}} \exp\left(-\frac{1}{2}\sum_{ab}\Gamma_{ab}(R-\mathcal{R})^a(R-\mathcal{R})^b\right), \tag{2.4.11}$$

and finally the averages of operators that only depend on spatial coordinates are given by

$$\langle O \rangle_{\tilde{\rho}_{\mathcal{R},\mathbf{\Phi}}} = \int \mathrm{d}\boldsymbol{R}\, O(\boldsymbol{R})\tilde{\rho}_{\mathcal{R},\mathbf{\Phi}}(\boldsymbol{R}). \tag{2.4.12}$$

The parameters $\mathcal{R}$ are called centroids because (using (2.4.12))

$$\langle \boldsymbol{R} \rangle_{\tilde{\rho}_{\mathcal{R},\mathbf{\Phi}}} = \mathcal{R}, \tag{2.4.13}$$

so they indicate the average positions.

In the context of SCHA, the best estimate for the free energy is given by

$$F^{(s)} = \min_{\mathcal{R}}(\min_{\mathbf{\Phi}} \mathcal{F}[\tilde{\rho}_{\mathcal{R},\mathbf{\Phi}}]). \tag{2.4.14}$$

We have to make some definitions. First, we indicate as the SCHA matrix $\boldsymbol{f}(\mathcal{R})$ the matrix that minimizes $\mathcal{F}[\tilde{\rho}_{\mathcal{R},\mathbf{\Phi}}]$ with respect to $\mathbf{\Phi}$. Then, we define the centroid equilibrium position $\mathcal{R}_{eq}$ to be the configuration of centroids for which $\mathcal{F}[\tilde{\rho}_{\mathcal{R},\boldsymbol{f}(\mathcal{R})}]$ is minimized with respect to $\mathcal{R}$. The SCHA matrix $\boldsymbol{f}(\mathcal{R})$ satisfies the self-consistent equation

$$f_{ab}(\mathcal{R}) = \left\langle \frac{\partial^2 E^{el}}{\partial R^a \partial R^b} \right\rangle_{\tilde{\rho}_{\mathcal{R},\boldsymbol{f}(\mathcal{R})}}. \tag{2.4.15}$$

The matrix $f_{ab}(\mathcal{R})$ can be used to find the auxiliary phonons for the system. In particular, the eigenvalues ω_p and eigenvectors A_p^a of the matrix

$$D_{ab}^{(0)} = \frac{1}{\sqrt{M_a M_b}} f_{ab}(\mathcal{R}_{eq}) \tag{2.4.16}$$

will give us phonon frequencies that include anharmonic effects. By definition, the frequencies are positive.

We now give a way to check the stability of the system, by including another SCHA order in the computation of the second derivative of F with respect to the centroid positions. We will only cite the result, referencing to [Bianco et al., 2017] for proofs. The first derivative of $F^{(s)}$ is very intuitive:

$$\frac{\partial F^{(s)}}{\partial \mathcal{R}^a} = \left\langle \frac{\partial E^{el}}{\partial R^a} \right\rangle_{\tilde{\rho}_{\mathcal{R},\boldsymbol{f}(\mathcal{R})}}. \tag{2.4.17}$$

The zero of this derivative gives us a way to find the equilibrium centroids $\mathcal{R}_{eq}$. It is important to note that the equilibrium centroids are in general different from the equilibrium coordinates of the system computed through the minima of the Born-Oppenheimer energy surface and used in Quantum Monte Carlo problems, because they include lattice quantum anharmonic effects. Next, we define the SCHA tensor

$$\overset{(n)}{f}_{a_1 \dots a_n} = \left\langle \frac{\partial^n E^{el}}{\partial R^{a_1} \dots \partial R^{a_n}} \right\rangle_{\mathcal{R},\boldsymbol{f}(\mathcal{R})}. \tag{2.4.18}$$

Obviously, $\overset{(2)}{\boldsymbol{f}}$ coincides with $\boldsymbol{f}$.We define in terms of A_p^a and ω_p the functions

$$s(\omega_p, \omega_q) = \begin{cases} 2\left(\frac{2n_q+1}{2\omega_q} - \frac{\mathrm{d}n_q}{\mathrm{d}\omega_q}\right), & \text{if } \omega_p = \omega_q, \\ 2\left(\frac{n_p+n_q+1}{\omega_p+\omega_q} - \frac{n_p-n_q}{\omega_p-\omega_q}\right), & \text{if } \omega_p \neq \omega_q, \end{cases} \tag{2.4.19}$$

and

$$\Lambda^{abcd} = -\frac{1}{8}\sum_{p,q} \frac{s(\omega_p,\omega_q)}{\omega_p\omega_q} \frac{A_q^a}{\sqrt{M_a}} \frac{A_p^b}{\sqrt{M_b}} \frac{A_q^c}{\sqrt{M_c}} \frac{A_p^d}{\sqrt{M_d}}. \tag{2.4.20}$$

The second derivative of the free energy is then given in matrix form by

$$\frac{\partial^2 F^{(s)}}{\partial\mathcal{R}\partial\mathcal{R}} = \boldsymbol{f} + \overset{(3)}{\boldsymbol{f}}\,\boldsymbol{\Lambda}\left(\mathbf{1} - \overset{(4)}{\boldsymbol{f}}\,\boldsymbol{\Lambda}\right)^{-1}\overset{(3)}{\boldsymbol{f}}\,. \tag{2.4.21}$$

If we neglect the second term, we obtain the stable system of phonons that we started with. When evaluating this matrix at $\mathcal{R}_{eq}$, we obtain the dynamical matrix $D_{ab}^{(F)}$ given by

$$D_{ab}^{(F)} = \frac{1}{\sqrt{M_a M_b}}\left[\frac{\partial^2 F^{(s)}}{\partial\mathcal{R}^a\mathcal{R}^b}\right]_{\mathcal{R}=\mathcal{R}_{eq}}. \tag{2.4.22}$$

With this corrected dynamical matrix, we can finally obtain a stability condition: the system is stable if $D_{ab}^{(F)}$ is positive definite. The main difference with $D_{ab}^{(0)}$ is that $D_{ab}^{(F)}$ can have negative eigenvalues, while $D_{ab}^{(0)}$ cannot by construction. We stress that in our work we make use of the phonons obtained from $D_{ab}^{(0)}$: the computation of $D_{ab}^{(F)}$ will just be a verification of the stability of the structure.

Lastly, we come to the stochastic implementation of SCHA, called SSCHA. This method uses sampling techniques as those described in section 2.1 in order to compute the quantities of interest in SCHA. In a typical computation, we have to take averages of operators O that depend only on the position, making use of (2.4.12). We sample the space of configurations $\boldsymbol{R}$ obtaining a large number $N_{\mathcal{I}}$ of configurations $\boldsymbol{R}_{\mathcal{I}}$, where the sampling is done from an initial density matrix $\tilde{\rho}_{in}(\boldsymbol{R})$. Then, the average of an operator O according to a generic distribution probability $\tilde{\rho}_{\mathcal{R},\boldsymbol{\Phi}}$ is given by

$$\langle O\rangle_{\tilde{\rho}_{\mathcal{R},\boldsymbol{\Phi}}} \sim \frac{1}{N_{\mathcal{I}}}\sum_{\mathcal{J}=1}^{N_{\mathcal{I}}} \frac{\tilde{\rho}_{\mathcal{R},\boldsymbol{\Phi}}(\boldsymbol{R}_{\mathcal{J}})}{\tilde{\rho}_{in}(\boldsymbol{R}_{\mathcal{J}})} O(\boldsymbol{R}_{\mathcal{J}}). \tag{2.4.23}$$

The equality holds when $N_{\mathcal{I}}$ is infinite. We now apply this procedure to (2.4.21) given a SCHA density $\boldsymbol{f}$. We first compute the matrix $\boldsymbol{\Gamma}$ from the definition (2.4.9), denote $\boldsymbol{u} = \boldsymbol{R}_{\mathcal{I}} - \mathcal{R}$ from the sampling and define

$$\mathcal{C}_a = -\left[\frac{\partial E^{el}(\boldsymbol{R})}{\partial R^a}\right]_{\boldsymbol{R}=\boldsymbol{R}_{\mathcal{I}}} + \left\langle \frac{\partial E^{el}(\boldsymbol{R})}{\partial R^a} \right\rangle_{\tilde{\rho}_{\mathcal{R},\boldsymbol{f}}} + \sum_b f_{ab} u^b. \tag{2.4.24}$$

It can be shown [Bianco et al., 2017] that the tensors $\overset{(3)}{\boldsymbol{f}}$ and $\overset{(4)}{\boldsymbol{f}}$ can be computed as

$$\overset{(3)}{f}_{abc} = -\sum_{pq} \Gamma_{ap}\Gamma_{bq} \left\langle u^p u^q \mathcal{C}_c \right\rangle_{\tilde{\rho}_{\mathcal{R},\boldsymbol{f}}}, \tag{2.4.25}$$

$$\overset{(4)}{f}_{abcd} = -\sum_{pqr} \Gamma_{ap}\Gamma_{bq}\Gamma_{cr} \left\langle u^p u^q u^r \mathcal{C}_d \right\rangle_{\tilde{\rho}_{\mathcal{R},\boldsymbol{f}}}, \tag{2.4.26}$$

where the averages are taken with the sampling procedure. With those elements, (2.4.21) can be computed straightforwardly by calculating forces and energies in the $\boldsymbol{R}_{\mathcal{J}}$ configurations in supercells, and then the procedure of gradient descent minimization can be used to minimize the value of $F^{(s)}$.

Chapter 3

Tetrahedral occupations in Palladium Hydride compounds

The first compound that we study in this thesis is palladium hydride (PdH), a compound that has a central role in different scientific fields. PdH belongs to the class of metal hydrides, and some of them exhibit superconductivity at ambient pressure (PdH itself was studied in [Skoskiewicz, 1972,Stritzker and Buckel, 1972a, Schirber and Northrup, 1974,Schirber et al., 1984], and another important example is Th_4H_{15} [Satterthwaite and Toepke, 1970]), but the critical temperature is low, around 10 K. In a recent unconfirmed work, it was claimed that metastable phases of PdH grown with a fast-cooling technique yield a higher value of T_c, even reaching 60 K for the deuterium compound [Syed et al., 2016]. If this result is confirmed, PdH would become a first example of a high-T_c hydride at ambient pressure. One of the central goals of this chapter is to examine this claim from a computational point of view, by proving that those metastable states exist, studying their structure and their superconductive properties. We start by giving general information on the compound.

PdH was first studied in [Graham, 1869], and has been widely used for hydrogen storage, as films of Pd can absorb considerable quantities of H atoms [Alefeld and Völkl, 1978, Fukai, 2006, Lewis, 1967]. It is possible to build compounds with different values of the H/Pd ratio. Such compounds have been called PdH_x, where x indicates the H/Pd ratio. Studying PdH_x compounds at various values of x, in [Skoskiewicz, 1972] it was proven experimentally that PdH_x compound

has an observable transition to a superconductive phase at low temperature when x is above 0.80, and the critical temperature for superconductivity rises as x is increased. This shows an example of hydrogen based superconductivity enhancement, a behaviour that at the time of the cited article was only observed for Th_4H_{15}.

In PdH, palladium atoms arrange in a face centred cubic (fcc) lattice, where the hydrogen atoms can occupy tetrahedral or octahedral interstitial sites, and experimental evidence shows that the favourite configuration is the octahedral one. This experimental evidence is based on neutron diffraction experiments [Worsham Jr et al., 1957] and on the agreement of *ab initio* calculations [Errea et al., 2013] and experimental phonon spectra obtained with inelastic neutron scattering and Raman experiments [Rowe et al., 1974, Rowe et al., 1986, Kolesnikov et al., 1991, Sherman et al., 1977, Ross et al., 1998, Chowdhury and Ross, 1973]. In [Elsässer et al., 1991] the vibrational energies of the octahedral and tetrahedral configurations were studied using a simplified harmonic potential. The conclusion of the paper is that both octahedral and tetrahedral configurations are local energy minima, and the octahedral configuration is favoured with respect to the tetrahedral one. Due to the existence of an energy barrier, tetrahedral configurations are metastable, and there is experimental evidence for partial occupation in interstitial tetrahedral sites in the deuterite compound [Pitt and Gray, 2003, McLennan et al., 2008].

The arrangement of hydrogen atoms in PdH is fundamental in the claim of [Syed et al., 2016], as the claim is that the high-T_c structures obtained through fast cooling methods are metastable states, with partial or full tetrahedral occupation. The energetic comparison between different possible sites has not been performed fully including the lattice zero-point energy and anharmonic effects so far, which are very important for correctly describing this system [Errea et al., 2013]. In this chapter, we present for the first time *ab initio* structural relaxations of several PdH structures with mixed octahedral and tetrahedral site occupations with the inclusion of quantum lattice zero-point energy using the SSCHA formalism of section 2.4. We will explore metastable states and characterize them according to the number of octahedral and tetrahedral sites occupied, and compute T_c for a number of structures, comparing our results against [Syed et al., 2016].

3.1 Methods and computational details

In the present analysis we work always with the stoichiometric ratio $x = 1$. While other stoichiometries are certainly interesting, we study this particular ratio as it is the one that yields the highest T_c [Skoskiewicz, 1972, Stritzker and Buckel, 1972b, Schirber and Northrup, 1974, Schirber et al., 1984] and is the one that in principle yielded superconductivity above 50 K [Syed et al., 2016]. In order to study the energies of configurations with tetrahedral site occupation, we have constructed a $2 \times 2 \times 2$ supercell starting from the primitive fcc lattice, i.e. with 8 Pd atoms, and randomly place 8 hydrogen atoms between the octahedral and tetrahedral sites. We classify the structures by the number of occupied octahedral sites in the beginning. In any configuration, if n hydrogen atoms occupy octahedral sites (with n from 0 to 8), then $8-n$ hydrogen atoms occupy tetrahedral sites. Note that per Pd atom in the fcc lattice there is one octahedral site and 2 tetrahedral sites. The structure with full octahedral occupation, $n = 8$, has a space group $Fm\bar{3}m$ and all positions are fixed by symmetry. Configurations with partial or full tetrahedral occupation have a lower symmetry and, in most of the cases, atoms are no longer fixed to a specific lattice site and can thus relax. We have performed these relaxations both in the classical case, assuming that ions are classical objects and therefore adopt the positions given by the local minima of the Born-Oppenheimer energy surface $E^{el}(\mathbf{R})$, and in the quantum case within the SSCHA, which accounts for the quantum zero-point energy including anharmonicity at a non-perturbative level.

Classical structural relaxations on the Born-Oppenheimer energy surface were performed with DFT making use of the plane-waves Quantum ESPRESSO package [Giannozzi et al., 2009, Giannozzi et al., 2017]. The exchange-correlation functional was approximated with the Perdew-Burke-Ernzerhof (PBE) parametrization [Perdew et al., 1996]. Brillouin zone integrals in the DFT self-consistent calculations were performed with a $12\times12\times12$ **k**-point grid for the $2 \times 2 \times 2$ supercell containing 16 atoms. We used a kinetic energy cutoff for the wave functions of 55 Ry and of 550 Ry for the charge density. Projector-augmented wave pseudopotentials from the Quantum ESPRESSO library were used [Dal Corso, 2014], with 10 electrons in the valence for Pd.

SSCHA quantum anharmonic structural relaxations were performed on the same $2 \times 2 \times 2$ supercell with 16 atoms. The SSCHA minimization requires the

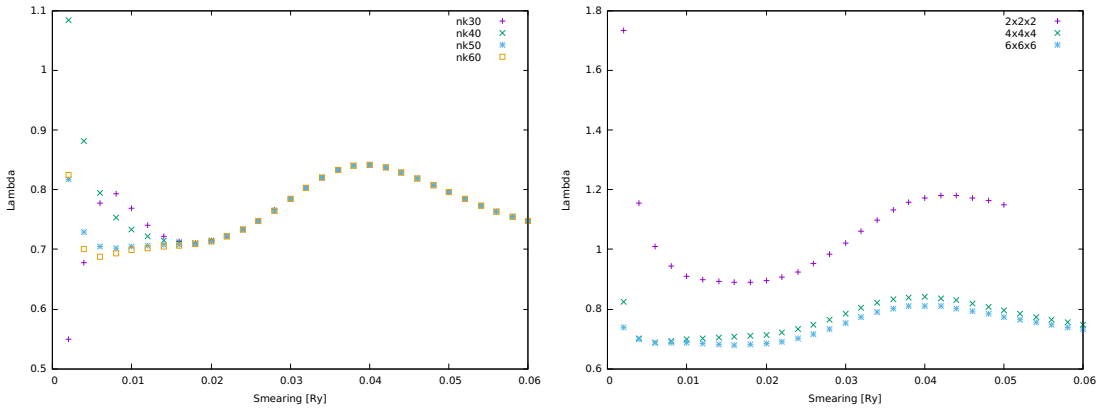

Figure 3.1: Verification of convergence by computing the electron-phonon coupling constant λ for various smearings for the full octahedral occupation system. In the figure on the left, we have used a 4×4×4 **q**-point grid for the primitive cell to compute λ, and we have compared results for $30\times30\times30$, $40\times40\times40$, $50\times50\times50$ and $60\times60\times60$ **k**-point grids. At smearing 0.01, the results obtained from the various **k**-grid are at reasonable convergence. On the right we have three various **q**-point grids for the primitive cells compared, with a $60\times60\times60$ **k**-grid: a $2\times2\times2$, a $4\times4\times4$ and a $6\times6\times6$. While the improvement from $2\times2\times2$ to $4\times4\times4$ is significant, the improvement from $4\times4\times4$ to $6\times6\times6$ is not significant enough at 0.01 Ry to justify its use. This justifies our use of a $4\times4\times4$ **q**-point grid for the primitive unit cell (or, equivalently, a $2\times2\times2$ grid for the supercell).

calculation of atomic forces on different random configurations generated according to $\tilde{\rho}_{\boldsymbol{\mathcal{R}},\boldsymbol{\Phi}}$, as defined in section 2.4. These forces were calculated *ab initio* with DFT, with the same parameters used for the classical relaxations. Due to the reduced symmetry of many of the structures analyzed, a large number of random configurations were needed to converge the SSCHA minimization, in the order of 10000 per compound for the less symmetric cases.

We have calculated the phonon spectra of the structures relaxed at the quantum level with the SSCHA both at the harmonic level and the anharmonic level. The electron-phonon interaction is also estimated at the harmonic and at the SSCHA levels for these structures. The main results from this analysis are the Eliashberg function and the effective electron-phonon coupling, computed as in section 1.5. The Hamiltonian entering the electron-phonon coupling in the Eliashberg function as well as the harmonic phonon frequencies have been calculated within density-functional perturbation theory (DFPT) [Baroni et al., 2001] in a

$2 \times 2 \times 2$ **q**-point grid of the 16 atoms supercell. The harmonic $\alpha^2F(\omega)$ [Giustino, 2017b] has been obtained with a $30 \times 30 \times 30$ **k**-point grid for the Brillouin zone integrals on the electronic states, and a 0.01 Ry Gaussian smearing for the double Dirac delta on the Fermi surface. The convergence of the **q**- and **k**-point grids was carefully studied, and the parameters used are consistent with those used for the primitive cell of PdH with full octahedral occupation [Errea et al., 2013]. We have checked the convergence of the **q**- and **k**-point grids by computing λ in the full octahedral system as a function of the smearing parameter for various grids, and we report the results of this analysis in figure 3.1. In order to obtain the anharmonic $\alpha^2F(\omega)$ in the same $2 \times 2 \times 2$ **q**-point grid of the 16 atom supercell, we interpolate the difference between the Γ point SSCHA auxiliary dynamical matrix and the harmonic result at this point to the finer $2 \times 2 \times 2$ grid. Adding the harmonic result back to the interpolated result, we have obtained the anharmonic phonons in the $2 \times 2 \times 2$ grid. The anharmonic $\alpha^2F(\omega)$ is obtained by combining the calculated deformation potential with the eigenvalues and eigenfrequencies of the dynamical matrix defined by the SSCHA auxiliary force constants. The superconducting critical temperature was obtained by solving the Allen-Dynes modified equation (1.5.22) with different values of μ^*.

3.2 Results

We start our analysis of possible metastable states with partial tetrahedral sites occupation by creating configurations in the $2\times2\times2$ supercell randomly occupying tetrahedral and octahedral interstitial sites in the fcc Pd lattice, assuming a lattice parameter of 7.814 a_0, the equilibrium lattice parameter obtained in the Born-Oppenheimer classical energy surface for PdH with full octahedral occupation within PBE and without considering the zero point motion. For each initial number of atoms in octahedral sites, we create 10 random structures. As shown in Fig. 3.2, these structure have a wide range of Born-Oppenheimer energies, with differences up to almost 0.4 eV per PdH. This shows that arranging H atoms at different interstitial sites can considerably change the total energy of the system, showing that H-H and Pd-H interactions are strongly dependent on the site of hydrogen atoms. For this lattice parameter (7.814 a_0), the structure with lowest Born-Oppenheimer energy is the one with full octahedral occupation ($n = 8$). It is interesting to remark that, as illustrated in the bottom panel of Fig. 3.2, these

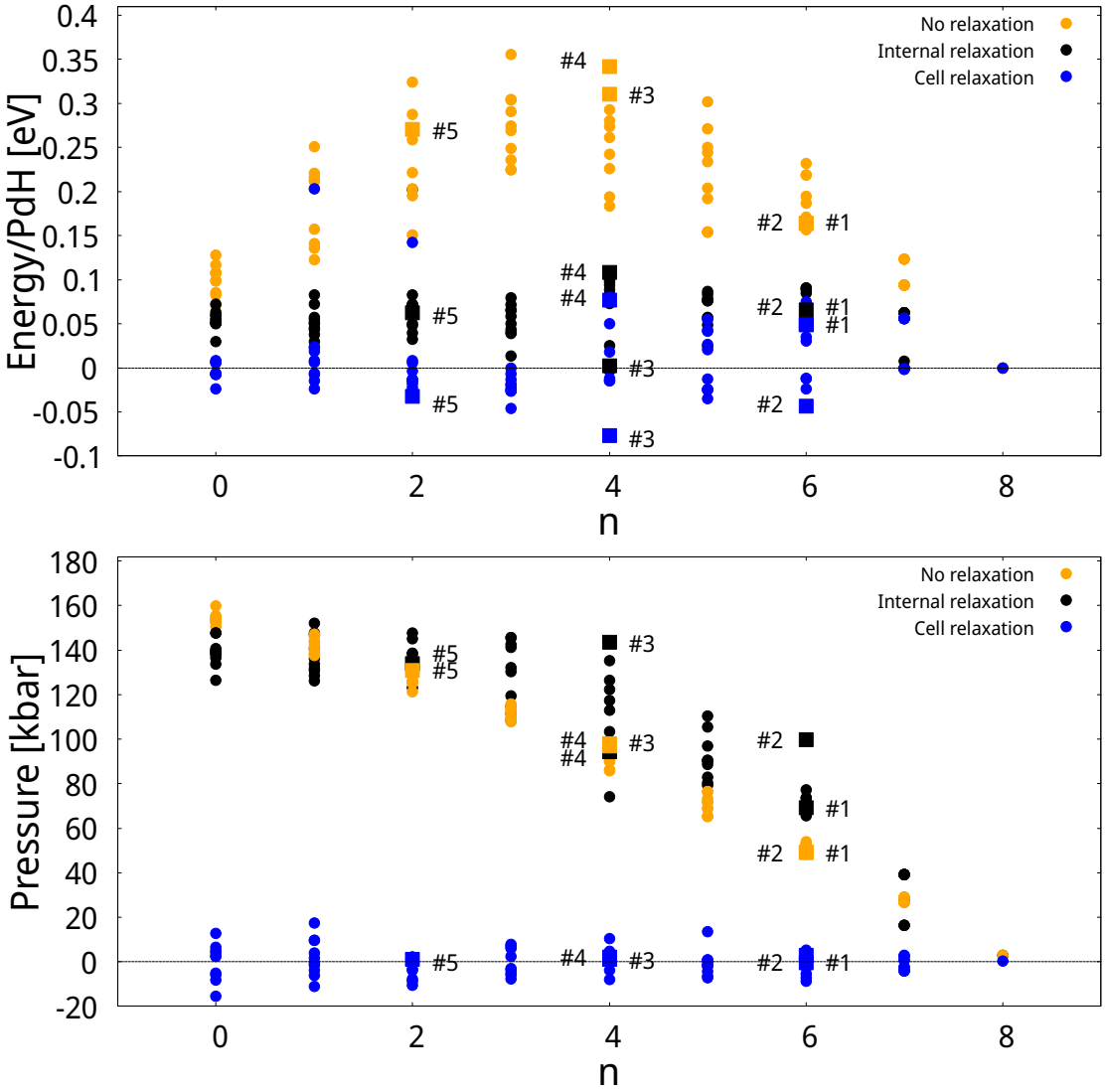

Figure 3.2: Born-Oppenheimer energies (top panel) and pressures (bottom panel) for structures with hydrogen atoms at random interstitial sites. The structures are classified according to the number of occupied octahedral sites at the beginning of the calculation, n. The data in orange refers to the initial non-relaxed structures, while in black we show the data for the internal relaxed structures (internal relaxation) keeping the unit cell unchanged. The data in blue corresponds to the classical relaxation in which the unit cell is allowed to change (cell relaxation). In each class of data, we have marked with numbers the energies and pressures of the structures that we study with the SSCHA method *a posteriori*, which are marked with a square and not a dot. The energies are measured from the energy of the structure with full octahedral occupation, $n = 8$.

random structures have a very different pressure, which increases with the number of H atoms occupying tetrahedral sites, reaching a pressure of 160 kbar for the fully tetrahedral structure ($n = 0$). Thus, structures with tetrahedral sites occupied have a larger lattice parameter.

As mentioned above, once tetrahedral interstitial sites start being occupied, the symmetry of the crystal is reduced and atoms are not fixed to their sites by symmetry anymore. We first relax these structures to the Born-Oppenheimer energy minima only modifying the internal positions, without modifying the fcc primitive lattice vectors and keeping the 7.814 a_0 lattice parameter. These reduces considerably the energies of the structures with tetrahedral sites occupied ($n < 8$) with respect to the full octahedral occupation, but still the full octahedral site structure remains the lowest energy one. However, considering that the $n < 8$ structures still are subject to a positive pressure with this unit cell, the energy is not the appropriate thermodynamic quantity for the comparison. We thus fully relax these structures to the Born-Oppenheimer minima with a target pressure of 0 kbar, with a tolerance of about 10 kbar. Most of the cell relaxations are performed by only adjusting the length of the lattice parameters, keeping fcc lattice vectors. In order to study the possibility of symmetry breaking of the cell, we also relaxed some structures allowing full adjustment of the lattice vectors with no restrictions. After the cell relaxations the pressure of all structures is comparable and the energy becomes the right thermodynamic variable. Interestingly, structures with partial or even full tetrahedral occupation have a lower energy than the full octahedral structure, remarking that tetrahedral and octahedral occupation of interstitial sites are very competitive in energy, as previously described in the literature [Elsässer et al., 1991, Caputo and Alavi, 2003].

The evolution of the classical relaxation of some of these structures is illustrated in Fig. 3.3. The structures change strongly from their initial starting point, which addresses the shallowness of the energy barriers between different interstitial sites [Elsässer et al., 1991, Blanco-Rey et al., 2014]. Some of the calculations show that, despite departing with some H atoms at octahedral sites, the final structures only contain H atoms at tetrahedral sites, like those labeled as #2, #3, and #5. Structures #1, #3, #4, and #5 were relaxed keeping the fcc cell vectors and the lattice parameters increased between a 1.5% and 2.5% depending on the case. The structural modifications mainly involve hydrogen atoms in these cases, as Pd atoms remain with an arrangement that is not far from the perfect fcc. Consid-

Structure	No rel	Internal rel	Cell rel	SSCHA rel
#1	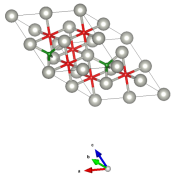	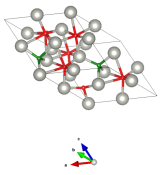	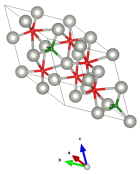	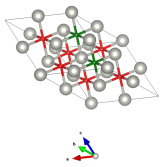
#2	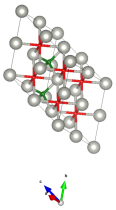	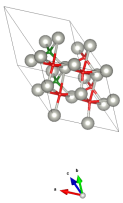	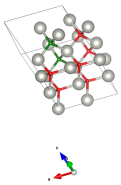	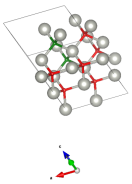
#3	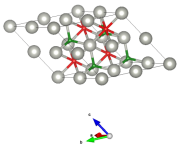	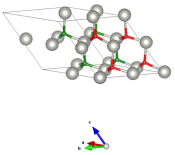	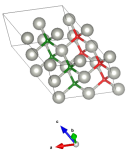	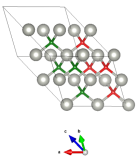
#4	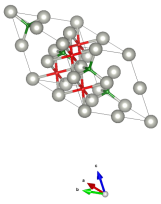	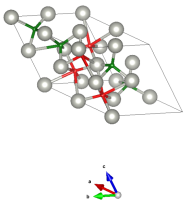	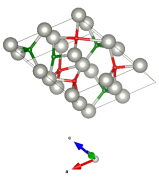	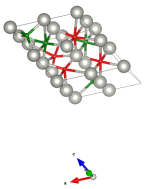
#5	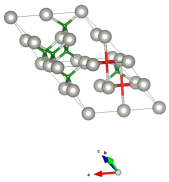	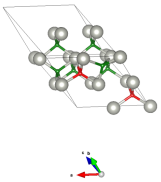	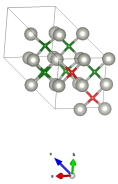	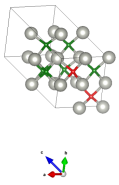

Figure 3.3: Graphical visualization of the structures, ordered from structure #1 to #5. For every structure, we present from left to right the non-relaxed starting structure (No rel), the relaxed structure without modifications of the cell (Internal rel), the relaxed structure obtained by also relaxing the unit cell (Cell rel), and the structure obtained with the quantum relaxation given by the SSCHA (SSCHA rel). We mark in red the hydrogen atoms in octahedral sites at the beginning of the calculation and in green the ones in tetrahedral sites. The atoms keep their initial color for the other relaxations. The bonds plotted have a cutoff distance of $\sim 4.7a_0$.

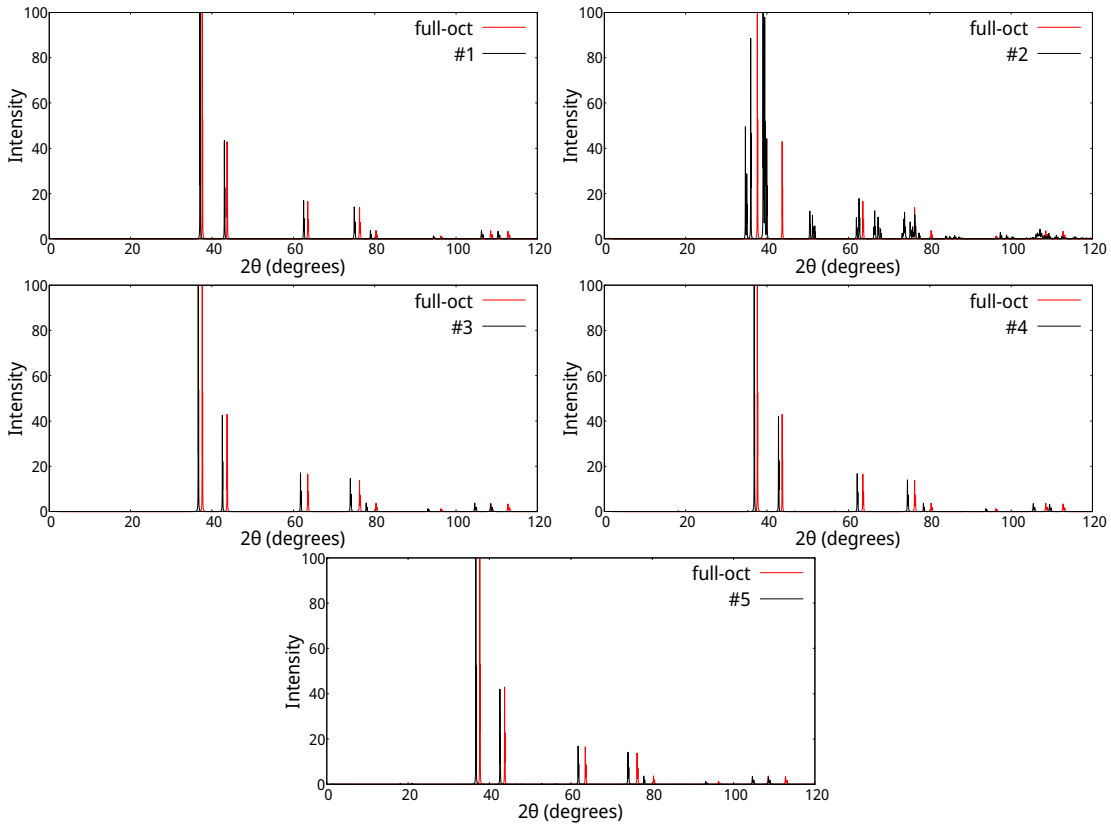

Figure 3.4: Diffraction patterns for the selected structures (black), compared with the full octahedral structure (red). Due to the fact that the Pd atoms move little between structures, we can only see shifts and not significantly different peaks, with the exception of structure #2.

ering that H atoms are invisible to x-ray diffraction experiments, distinguishing these structures from the full octahedral configuration would be difficult by x-ray, only an expansion of the lattice should be detected for those cases with occupied tetrahedral sites. For structure #2 the situation is different, as the unit cell vectors are allowed to fully change: at the end of the classical cell relaxation a monoclinic lattice is obtained, with two lattice vectors that dilate by factors of 1.4% and 2.4%, respectively, and the other vector that contracts by a factor of 0.5%. The angles shift to 59°, 74° and 60° between the relaxed unit cell vectors. We tabulate in table 3.1 the shapes of the structures before and after the relaxation. Due to the lattice change, the structure should be distinguishable from the $Fm\bar{3}m$ structure by x-ray diffraction. In figure 3.4, we report the relevant diffraction patterns, compared with the full octahedral structure.

Str. #1	a (Å)	b (Å)	c (Å)	α (°)	β (°)	γ (°)
Non relaxed	5.84776	5.84776	5.84776	60.00	60.00	60.00
Internal relaxation	5.84776	5.84776	5.84776	60.00	60.00	60.00
Cell relaxation	5.93594	5.93594	5.93594	60.00	60.00	60.00
SSCHA relaxation	5.93594	5.93594	5.93594	60.00	60.00	60.00

Str. #2	a (Å)	b (Å)	c (Å)	α (°)	β (°)	γ (°)
Non relaxed	5.84776	5.84776	5.84776	60.00	60.00	60.00
Internal relaxation	5.84776	5.84776	5.84776	60.00	60.00	60.00
Cell relaxation	5.93070	5.98525	5.81636	59.03	73.92	59.70
SSCHA relaxation	5.93070	5.98525	5.81636	59.03	73.92	59.70

Str. #3	a (Å)	b (Å)	c (Å)	α (°)	β (°)	γ (°)
Non relaxed	5.84776	5.84776	5.84776	60.00	60.00	60.00
Internal relaxation	5.84776	5.84776	5.84776	60.00	60.00	60.00
Cell relaxation	6.00204	6.00204	6.00204	60.00	60.00	60.00
SSCHA relaxation	6.00204	6.00204	6.00204	60.00	60.00	60.00

Str. #4	a (Å)	b (Å)	c (Å)	α (°)	β (°)	γ (°)
Non relaxed	5.84776	5.84776	5.84776	60.00	60.00	60.00
Internal relaxation	5.84776	5.84776	5.84776	60.00	60.00	60.00
Cell relaxation	5.96786	5.96786	5.96786	60.00	60.00	60.00
SSCHA relaxation	5.96786	5.96786	5.96786	60.00	60.00	60.00

Str. #5	a (Å)	b (Å)	c (Å)	α (°)	β (°)	γ (°)
Non relaxed	5.84776	5.84776	5.84776	60.00	60.00	60.00
Internal relaxation	5.84776	5.84776	5.84776	60.00	60.00	60.00
Cell relaxation	6.00064	6.00064	6.00064	60.00	60.00	60.00
SSCHA relaxation	6.00064	6.00064	6.00064	60.00	60.00	60.00

Table 3.1: Length of the lattice vectors of the supercell and angles between them of the structures #1 to #5, before and after the various relaxations. As it can be seen, only structure #2 is allowed to modify the shape of the lattice.

Considering the large anharmonicity at play in PdH, at least in the fully octahedral configuration [Errea et al., 2013], we further relax some of the structures obtained after the cell Born-Oppenheimer classical relaxation considering

Structure	Pressure (GPa)
#1	-3.1±0.1
#2	3.6±0.1
#3	3.2±0.1
#4	-0.7±0.1
#5	3.0±0.1

Table 3.2: Pressures calculated including quantum anharmonic effects with the SSCHA for the various structures, from #1 to #5. The pressures are expressed in GPa.

ionic quantum effects and anharmonicity within the SSCHA. Due to the large computational effort to structurally relax in the quantum energy landscape these structures that lack symmetry, we limit ourselves to relax the five representative structures labeled from #1 to #5 in all figures. Despite ionic quantum effects and anharmonicity can impact the cell parameters [Errea et al., 2020, Monacelli et al., 2018, Hou et al., 2021a, Hou et al., 2021b], considering the additional large computational effort required to relax the cell parameters for these systems with no symmetry, here we do not relax the unit cell further and just relax the internal centroid positions $\boldsymbol{\mathcal{R}}$ in the quantum energy landscape. However, the stress tensor calculated including ionic quantum effects [Monacelli et al., 2018] in these structures shows that there is a weak anisotropy in the stress tensor for any of the five structures, irrespective of whether the cell remains fcc-like or not. This suggests that fcc lattices can be realized in this system even if the symmetry is broken by the interstitial sites occupied by hydrogen, supporting the treatment given to the cell relaxation. We report the pressures for the various structures in table 3.2.

The impact of ionic quantum effects on the centroid positions is structure dependent. While some structures are radically changed by quantum effects, others do not exhibit drastic changes (see Fig. 3.3). Structure #1, which starts with 6 H atoms in octahedral sites and 2 in tetrahedral sites, deforms considerably in the classical relaxation with fixed cell and relaxing the cell, but still keeps hydrogens at the same interstitial sites. This is changed by the quantum SSCHA relaxation, which shifts the atoms in tetrahedral sites to octahedral sites, recovering the full octahedral configuration. Structure #2, which also starts with 6 octahedral and 2 tetrahedral sites, keeps those occupations after the classical internal relaxation, but the cell relaxation pushes all atoms into tetrahedral sites. The posterior quan-

tum SSCHA relaxation barely affects the structure, keeping all the H atoms at tetrahedral sites. Structure #3, starting with four octahedral and four tetrahedral sites, already with the first internal classical relaxation transforms into a full tetrahedral occupation, which does not evolve further after the classical cell and the quantum SSCHA relaxations. Structure #4, which start as well with an equal occupation of octahedral and tetrahedral sites, is particularly interesting as each relaxation induces a large change in the position of hydrogen atoms. Remarkably, ionic quantum effects stabilize a structure with mixed occupation of tetrahedral and octahedral sites. Finally, structure #5, which starts with the occupation of 6 tetrahedral and 2 octahedral sites, is similar to structure #2 since already at the internal relaxation all H atoms shift to a tetrahedral site and remain unaltered by the subsequent relaxations. All these calculations show that the quantum energy landscape in the PdH system is complex and many possible metastable states are possible, also when the zero point energy and anharmonicity are considered in the calculations. Regardless of the initial occupation of interstitial sites, our calculations show that stable or metastable states with full tetrahedral or octahedral occupations, as well as with mixed occupation of these sites, are possible.

Our SSCHA calculations can also analyze which of these states is the ground state structure once the ionic zero point energy and anharmonicity are considered in the calculations. As shown in Fig. 3.5, despite structures #2, #3, and #5 have a lower Born-Oppenheimer energy than the high-symmetry full octahedral structure, after the SSCHA relaxations the energy including ionic quantum anharmonic effects of these structures becomes larger. Consistently, structure #1, which evolves into the full octahedral occupation, reaches the same energy as the high symmetry $n = 8$ case. Thus, our calculations suggest that the structure with full occupation of octahedral sites is the ground state, as reported experimentally [Worsham Jr et al., 1957], thanks to lattice quantum effects and anharmonicity. However, metastable states with full or partial occupation of tetrahedral sites exist within 0.1 eV per PdH.

The reason why quantum effects affect one structure more than others is reflected in the phonon spectra shown in Fig. 3.6. For the final structure obtained after the SSCHA relaxation we calculate the phonon spectra in the harmonic approximation and from the SSCHA auxiliary dynamical matrices. Structures #2, #3, and #5 are barely affected by anharmonicity, while structures #1 and #4 are strongly anharmonic. This is consistent with the fact that the latter struc-

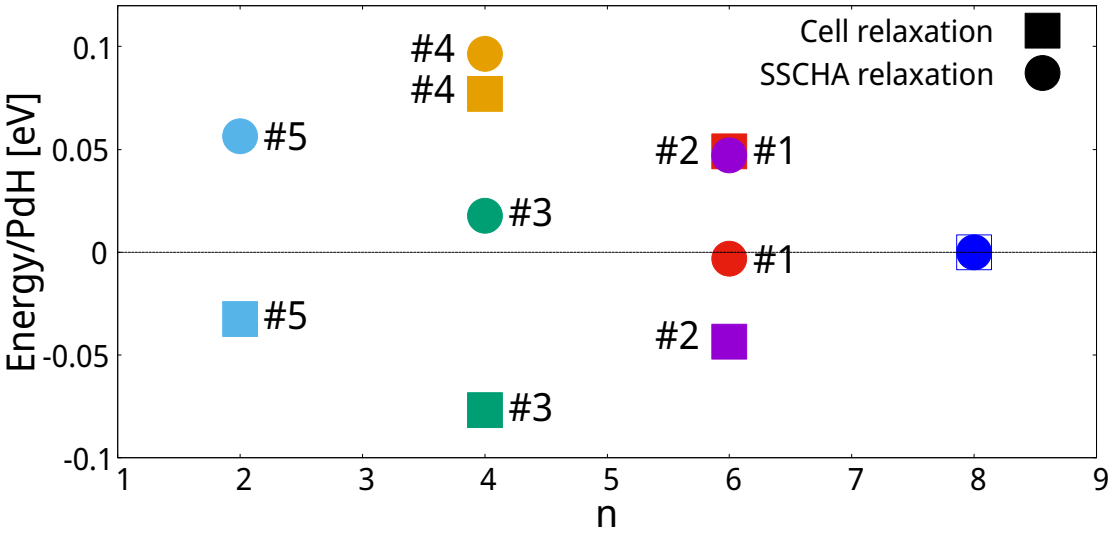

Figure 3.5: Comparison between the energies obtained with the classical relaxation including the unit cell (Cell relaxation) and with the quantum relaxation within the SSCHA (SSCHA relaxation) for the five selected structures. The zero of the energy is taken to be the energy of the structure with 8 occupied octahedral sites. The number on the right of each data point indicates the structure. The structures are characterized by n, the initial number of occupied octahedral sites.

Str.	Harmonic T_c (K)		SSCHA T_c (K)		Initial	Final
	$\mu^* = 0.085$	$\mu^* = 0.130$	$\mu^* = 0.085$	$\mu^* = 0.130$	oct.	oct.
#1	×	×	17.4	11.4	6	8
#2	3.3	1.6	2.8	1.3	6	0
#3	4.5	2.3	5.2	2.8	4	0
#4	×	×	8.3	5.5	4	Mixed
#5	2.2	0.7	1.5	0.4	2	0

Table 3.3: Superconducting critical temperatures calculated with different number of μ^* for the selected structures after the quantum SSCHA relaxation, computed with harmonic dynamical matrices and SSCHA auxiliary dynamical matrices. We also note the number of octahedral occupied positions before any relaxation and after the final SSCHA relaxation. Structures #1 and #4 do not have a harmonic value of T_c due to the presence of imaginary phonon frequencies at this level of theory.

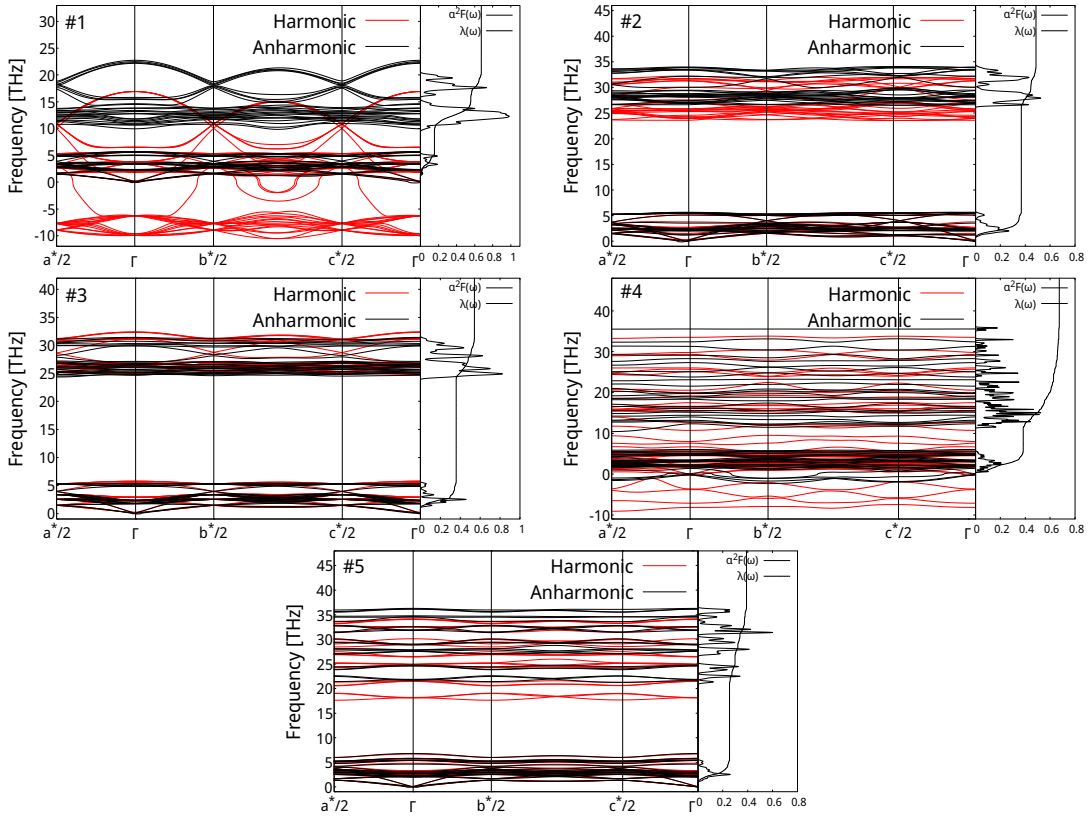

Figure 3.6: On the left, phonon spectra obtained in the harmonic and anharmonic calculations for the five selected structures in the structure obtained with the SSCHA relaxation. The a^*, b^*, and c^* parameters are the lengths of the reciprocal cell lattice vectors. On the right, Eliashberg function $\alpha^2F(\omega)$ and integrated electron-phonon coupling constants $\lambda(\omega)$ for the five selected structures in the structure obtained with the SSCHA relaxation. Anharmonic phonons are used in this calculation.

.

tures are the only ones that are considerably modified by quantum anharmonic effects. Interestingly, structure #1 has large imaginary phonon modes in the harmonic approximation, as it has previously been described for the high-symmetry $Fm\bar{3}m$ structure [Errea et al., 2013]. The same occurs to structure #4, which also has H atoms in octahedral sites. The analysis of the phonon spectra clearly indicates thus that anharmonicity is related to octahedral sites and not so much to tetrahedral sites, for which the potential seems rather harmonic. Hydrogen vibrations in tetrahedral sites are much harder, with energies above approximately

25 THz, while hydrogen atoms in octahedral sites vibrate with energies between approximately 10 and 20 THz. This is the reason why the structure with mixed octahedral and tetrahedral occupation (#4) has the broadest range of phonon frequencies. The differences between the structures and the lack of degeneracies in the phonon spectra are a consequence that all structures are not identical as no symmetries have been imposed.

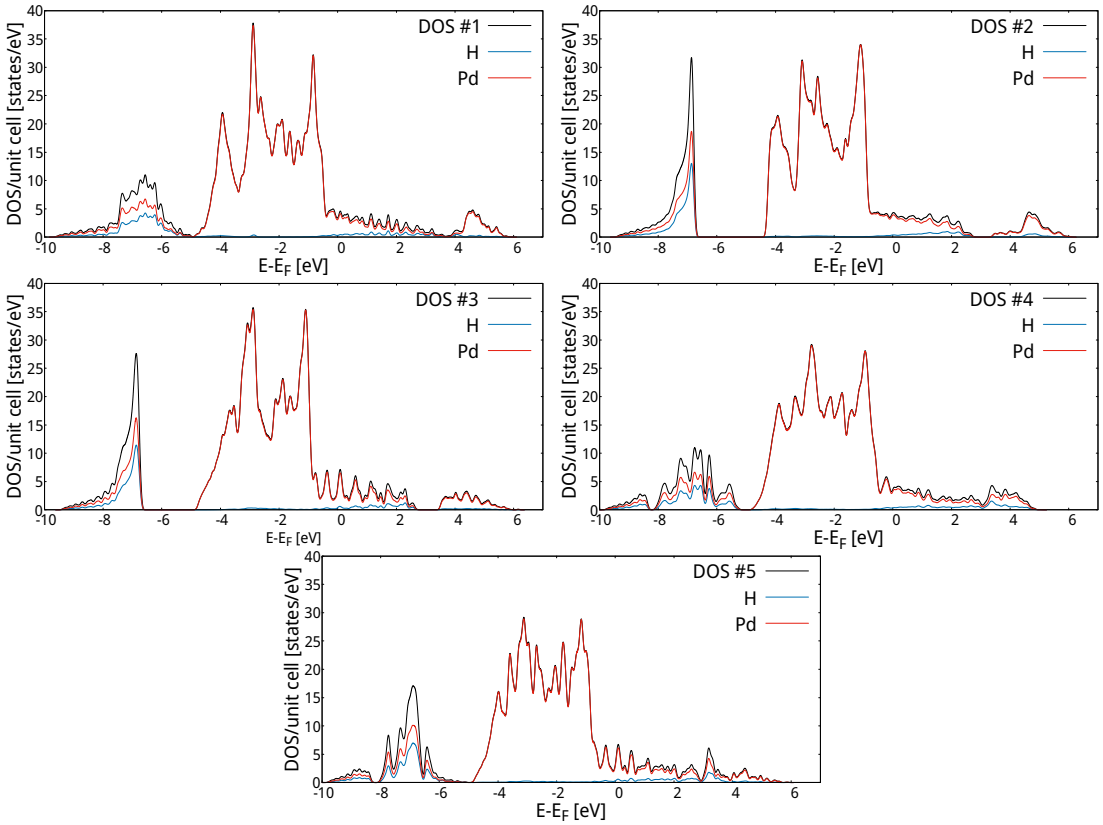

Figure 3.7: Density of states for the five selected structures in the structure obtained with the SSCHA relaxation. We plot the total DOS in black, the contributions from Pd to it in red, and the contribution from H in blue.

The existence of metastable states with full and partial occupation of tetrahedral sites suggests that it may be possible to synthesize these structures with fast-cooling techniques, as suggested by Syed et al. [Syed et al., 2016]. It has to be seen, however, whether these structures do increase the superconducting critical temperature with respect to the stable full octahedral configuration, as hypothesized in Ref. [Syed et al., 2016]. We calculate here the electron-phonon interaction and the T_c for the five structures analyzed previously, with the aim to address

this important point. Fig. 3.6 shows the Eliashberg function, $\alpha^2F(\omega)$, and the integrated electron-phonon coupling constant, $\lambda(\omega)$, for the anharmonic SSCHA calculation. From the figures we can deduce that the contribution of the high-energy H-character modes to the electron-phonon coupling constant is only sizable when octahedral sites are occupied, such as in structures #1 and #4. It is thus not surprising that the largest calculated T_c among these structures is the one with full octahedral occupation (#1), with T_c around 11.4 K with $\mu^* = 0.13$, followed by the one with mixed occupation (#4), with T_c around 5.5 K for the same value of the Coulomb pseudopotential (see Table 3.3). With the same parameters, the structures with full tetrahedral occupation have a lower critical temperature, between 0.4 and 2.8 K. This shows that the metastable occupation of tetrahedral sites is not beneficial for superconductivity and that the highest critical temperature is attained with the stable structure with full octahedral occupation.

The critical temperature calculated for the full octahedral configuration here is overestimated with respect to previous calculations also including anharmonic effects [Errea et al., 2013]. We attribute these differences to the fact that the lattice vectors here have not been relaxed in the quantum energy landscape, so that the lattice parameters in the calculations are different; a different exchange-correlation functional is used here; and the calculation here is performed in a non-symmetrized structure, not exactly with the $Fm\bar{3}m$ symmetry, in a 2×2×2 supercell. The previous calculations, thus, are performed in a more controlled way and are thus more reliable with respect to the absolute value of the calculated T_c, but the result obtained here is solid: full or partial metastable occupation of tetrahedral sites reduces the critical temperature.

In order to deepen on the origin of why tetrahedral sites occupation suppresses the electron-phonon coupling constant, we have calculated the density of states (DOS) and its projection onto Pd and H atoms. As shown in Fig. 3.7, irrespective of where hydrogen atoms sit, the DOS at the Fermi level is always dominated by Pd electrons. In other words, hydrogen plays no role in the bonding here, and consequently all these PdH phases can be categorized as *isolated* systems according to the classification of hydrogen-based superconductors introduced in Ref. [Belli et al., 2021]. In fact, this is the reason why the T_c of these compounds is small in comparison to other high-T_c hydrides [Belli et al., 2021]. Due to the lack of H-character electrons in the Fermi surface, the deformation potential is similar for all the studied structures and the dependence of T_c on the occupation

of tetrahedral sites is dominated by the phonon frequencies. As λ scales with the phonon frequencies as ω^{-2}, the harder phonon frequencies of tetrahedral sites lead to a lower coupling constant.

3.3 Conclusions

By analyzing many possible occupations of interstitial sites in palladium hydrides within DFT including ionic quantum and anharmonic effects, we conclude that, despite the configuration with all hydrogen atoms in octahedral sites is the ground state, partial and full tetrahedral sites can be occupied metastably. This opens the door to synthesizing structures with partial or full tetrahedral occupation, as suggested by recent experiments [Syed et al., 2016, Pitt and Gray, 2003, McLennan et al., 2008]. However, contrary to the hypothesis presented in [Syed et al., 2016], we demonstrate here that the occupation of tetrahedral sites does not increase the critical temperature of PdH, it suppresses it. Our results underline that quantum effects and anharmonicity are crucial in the thermodynamical (meta)stability of PdH structures, specially with respect to vibrations around the octahedral sites. The experiment measuring T_c values above 50 K in metastable PdH phases [Syed et al., 2016] is questioned by our theoretical calculations.

Chapter 4

Hydrogen Boride monolayer

We now focus on the second system that we analyse, hydrogen boride (HB). HB is a good candidate for superconductivity for two main reasons: enhancement of superconductivity by hydrogen absorption and similarities to MgB_2.

The enhancement of superconductivity by hydrogen absorption is a well known phenomenon, and notable examples are given by palladium hydrides (studied in the previous chapter). As we have mentioned, in the PdH_x compound a non zero T_c appears for x above 0.80, and rises as x is increased. The role of hydrogen in enhancing the T_c has been further studied in the context of monolayers at ambient pressures. In previous theoretical works based on first principles calculations, it has been shown that a MgB_2 monolayer, which has a critical temperature of 39 K in the bulk [Nagamatsu et al., 2001], can reach a T_c of 69 K after hydrogenation [Bekaert et al., 2019], and that p-doped graphane, a hydrogenated graphene monolayer, reaches a critical temperature of around 80 K even if graphene itself is not superconducting [Savini et al., 2010]. Hydrogenated monolayers offer thus a promising platform to synthesize high-T_c hydrogen-based compounds at ambient pressures, overcoming the limits of high-pressure superhydrides.

HB can be synthesised from MgB_2 [Nishino et al., 2017], a high temperature superconductor. In its structure, HB is similar to MgB_2, as it is believed to adopt a quasi-hexagonal structure with a boron honeycomb layer reminiscent of the structure of MgB_2, with H atoms out of plane [Nishino et al., 2017, Kawamura et al., 2019, Tateishi et al., 2019]. The structure of HB observed experimentally

seems to adopt a *Cmmm* space group as anticipated by *ab initio* crystal structure prediction calculations [Jiao et al., 2016]. More recently, different polymorphs of hydrogen and boron have been synthesized in the two-dimensional limit [Li et al., 2021], showing the potential of "borophane" to form different stable compounds at the nanoscale and broaden its applications in nanodevices.

Despite its semimetallic character [Tateishi et al., 2019], *Cmmm* HB is a good superconducting candidate for several reasons. Mainly because several parent "borophene" monolayers have been predicted to have T_c's of around 20 K [Gao et al., 2017] and hydrogenation, as mentioned above, is expected to enhance it. Also, because the bonding nature of boron in *Cmmm* HB is reminiscent of the sp^2 bonding in MgB_2, which is crucial for its large T_c, even if hydrogen has a large impact on the band structure of the compound [Tateishi et al., 2019]. The goal of the present work is to determine the potential superconductivity of *Cmmm* HB through first principles calculations based on the DFT techniques described in subsection 1.2.1. We have also analyzed the possibility of enhancing the critical temperature of the system by doping.

Our goal in this chapter is to study the HB monolayer as a possible candidate for high temperature superconductivity. We will analyse the compound using DFT, observing the electron bands and the electron-phonon interaction. As established in chapter 1, due to the importance of the Fermi surface in superconductivity, we will pay particular attention to the Fermi surface. After the observation of the standard system, we will analyse the superconductive properties after doping.

4.1 Methods and computational details

All computations have been performed using DFT within the Quantum ESPRESSO package [Giannozzi et al., 2009, Giannozzi et al., 2017], making use of the Perdew-Burke-Ernzerhof (PBE) parametrization of the exchange-correlation functional [Perdew et al., 1996]. The electron-ion interaction has been modeled making use of ultrasoft pseudopotentials, including $2s^2$ and $2p^1$ electrons of boron in the valence. The self-consistent DFT computation has been performed with a grid of $42\times42\times1$ $\mathbf{k}$ points for the integrals over the Brillouin zone and a Methfessel-Paxton first-order spreading smearing of 0.02 Ry [Methfessel and Paxton, 1989]. A kinetic energy cutoff of 50 Ry has been used for the plane-wave basis and a

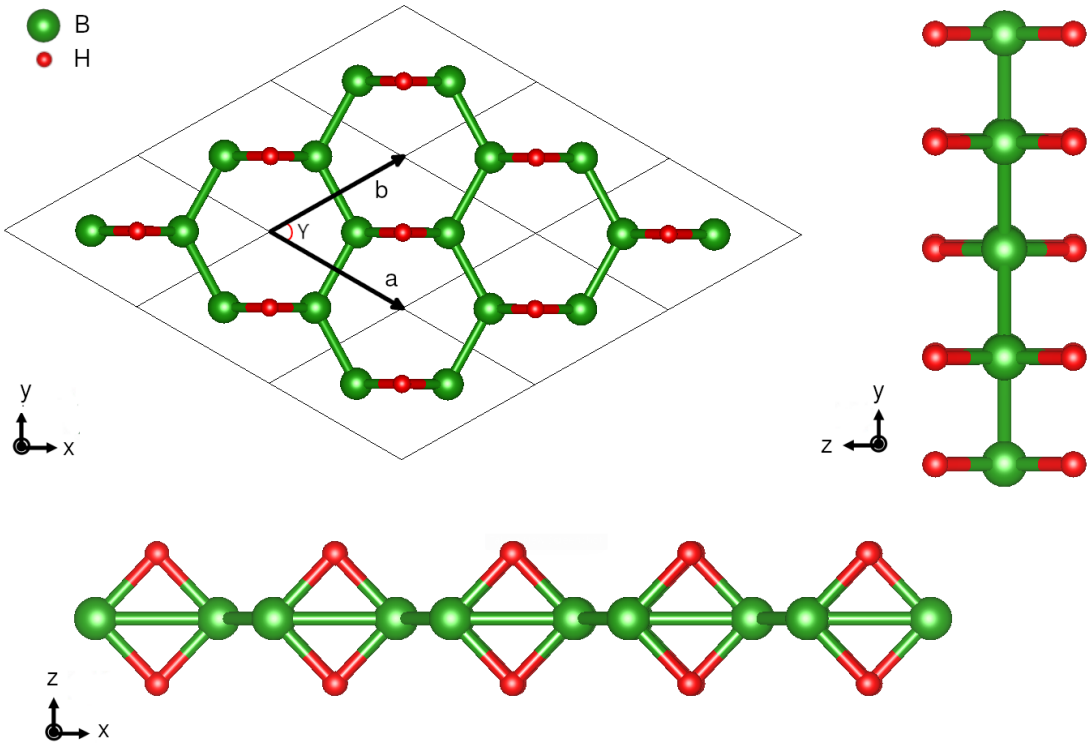

Figure 4.1: Different views of the crystal structure of the hydrogen boride (HB) monolayer in the *Cmmm* phase. The lattice parameters are indicated, together with the γ angle

500 Ry cutoff for the charge density. In order to avoid spurious interactions, we have left a vacuum between monolayer replicas of 35 a_0. Phonon frequencies have been computed in the harmonic approximation within DFPT [Baroni et al., 1987, Baroni et al., 2001]. Dynamical matrices have been calculated explicitly in an 8×8×1 grid of **q** points, and we have used Fourier interpolation to obtain the phonon spectrum. We have then estimated T_c by solving the Allen-Dynes equations [Eliashberg, 1960, Allen and Mitrović, 1983, Allen and Dynes, 1975], choosing the effective Coulomb potential μ^* between 0.08 and 0.12.

The calculation of the electron-phonon properties has been done by making use in Eq. (1.5.15) of a 60×60×1 grid of **k** points and an 8×8×1 grid of **q** points in Eq. (1.5.16). To approximate the delta functions in Eq. (1.5.15), we have used Gaussians with a broadening of 0.002 Ry. The **k**-point grid yielded converged λ values (where λ is the electron-phonon coupling constant (1.5.13)) even with such

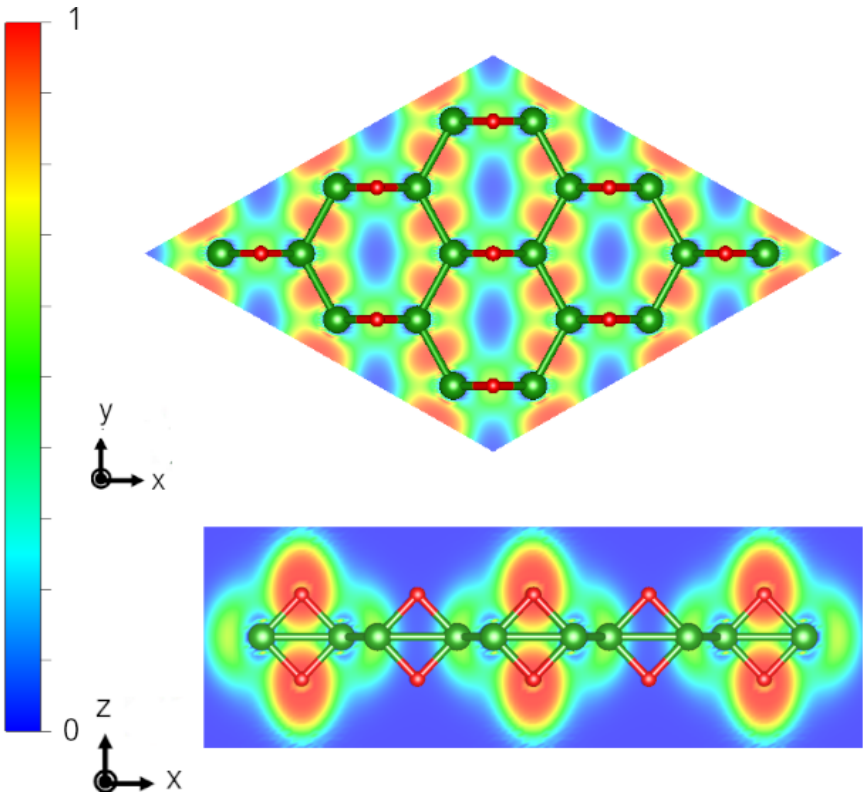

Figure 4.2: Electron localization function (ELF) for the non doped HB monolayer. In the top panel the $z = 0$ plane is represented, while in the bottom panel the $y = 0$ plane (putting the origin of coordinates at the position where the lattice vectors in Fig. 4.1 start).

a small broadening of the Delta funcitons.

As stated in the introduction, we have also studied the possibility of enhancing superconductivity by doping the system. We have doped the system by directly inserting or removing electrons and solving the Kohn-Sham equations, or including an external electric field in the calculations as it corresponds to a field effect transistor (FET) doping setup [Brumme et al., 2014, Brumme et al., 2015]. After doping, the crystal structure has been relaxed again until the forces and the strain tensor vanish. We have repeated the procedure subtracting electrons from the system. We have recomputed the electron and phonon bands, as well as the electron-phonon coupling with the inclusion of extra electrons or holes. The inclusion of the electric field in the calculations gave electronic band structures in agreement with those obtained with direct inclusion of electrons, validating the

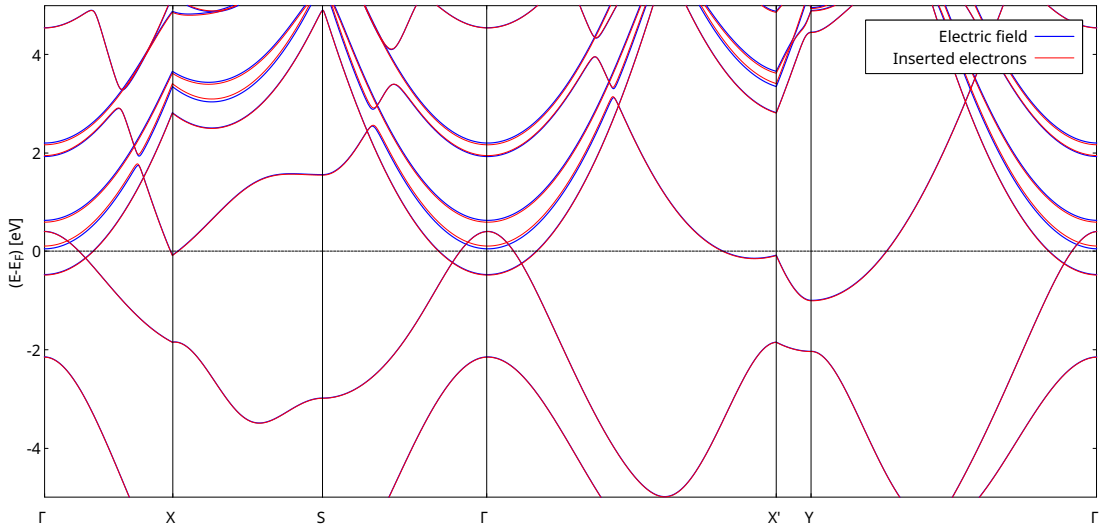

Figure 4.3: Comparison between the different types of doping. In red we have the electronic band structure for the insertion of 0.30 electrons per unit cell, while in blue we have the electronic band structure for the doping via an external electric field inducing a charge of 0.30 electrons per unit cell, corresponding to the previous doping. As it can be seen, we have almost perfectly superposed band structures, so the two different types of doping give the same results.

simpler approach. Therefore, here we report exclusively the results obtained by direct addition and subtraction of electrons. In figure 4.3 we compare the electronic band structure with the two different types of doping.

4.2 Results

4.2.1 Structural and electronic properties

We describe the centered rectangular lattice of $Cmmm$ hydrogen boride in the primitive cell as shown in Fig. 4.1, which includes two boron and two hydrogen atoms. In this description the two basis vectors **a** and **b** have the same length, which according to our DFT relaxations have a value of $a = b = 5.739a_0$. The angle between them is $\gamma = 59.33°$. All boron atoms form a quasihexagonal honeycomb-like lattice and the hydrogen atoms sit at a distance d from the boron plane.

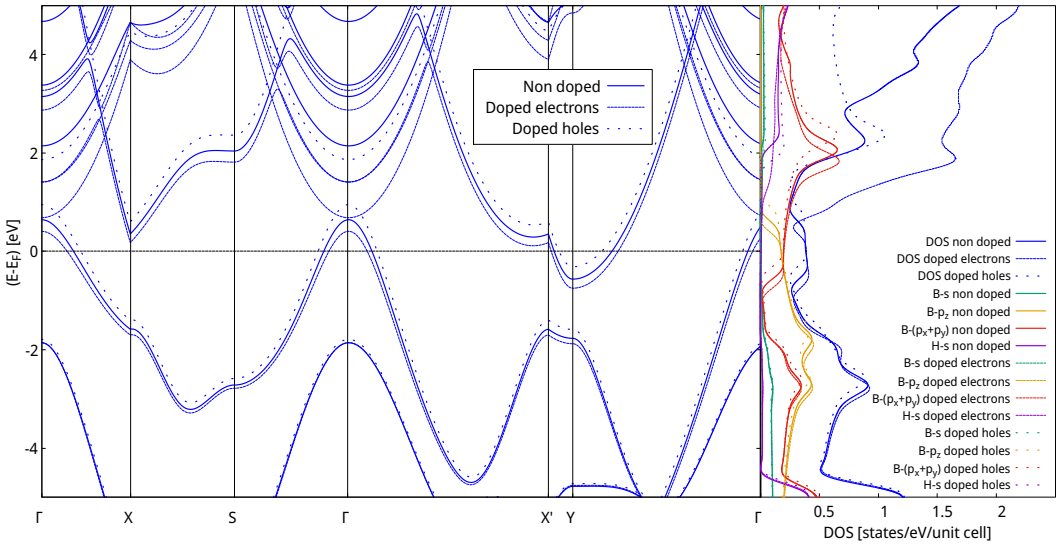

Figure 4.4: Electronic band structure (left panel) and density of states (DOS) (right panel) for *Cmmm* hydrogen boride. The bands and DOS are also plotted with electron and hole doping. The projection of the DOS onto atomic orbitals is also included.

More precisely the boron atoms are at $\alpha(\boldsymbol{a}+\boldsymbol{b})$ and $(1-\alpha)(\boldsymbol{a}+\boldsymbol{b})$, while the hydrogen atoms sit at $1/2(\boldsymbol{a}+\boldsymbol{b}) \pm d\hat{\boldsymbol{k}}$, where $\hat{\boldsymbol{k}}$ is the unitary vector in the out-of-plane direction. According to our calculations $\alpha = 0.328$ and $d = 1.828a_0$. All the parameters that determine the structure are summarized in Table 4.1. The obtained structural parameters are in agreement with previous calculations [Kawamura et al., 2019, Tateishi et al., 2019].

As illustrated by the calculated electron localization function (ELF) presented in Fig. 4.2, the presence of hydrogen affects the B-B bonding significantly. In a system like MgB_2, where the B layer is perfectly hexagonal, all boron atoms are covalently bonded at a distance of 3.34 a_0 [Tateishi et al., 2019]. The presence of hydrogen, however, changes the bonding pattern by shortening the B-B covalent bond that does not have a hydrogen atom above and below, while increasing the B-B length in the other bond due to the creation of a bridging B-H-B bond [Tominaka et al., 2020]. In fact, the presence of hydrogen destroys the covalent bond between the boron atoms by creating this bridging bonding. The B-B distances in the covalent bond are 3.25 a_0 while 3.44 a_0 between those affected by the B-H-B bonding.

	a (a_0)	α	γ	d (a_0)
Non doped	5.739	0.328	59.33°	1.828
Doped electrons	5.739	0.326	59.36°	1.810
Doped holes	5.739	0.330	59.27°	1.838

Table 4.1: Structural parameters of $Cmmm$ HB in the non doped and doped cases.

The band structure and the density of states (DOS) projected onto atomic orbitals are plotted in Fig. 4.4. The bands, which are in agreement with previous DFT and tight-binding results [Tateishi et al., 2019,Kawamura et al., 2019], show a semimetallic character, with a hole pocket at Γ and an electron pocket at Y, with two distinct bands crossing the Fermi level. The character of these two bands is mainly associated to the boron p orbitals. The hole pocket at Γ is coming from in-plane p_x and p_y orbitals, while the Y pocket from boron p_z [Tateishi et al., 2019].

The contribution of hydrogen to these bands that cross the Fermi level is scarce. Looking at the DOS projected onto atomic orbitals, we can see that hydrogen contributes to the DOS at the Fermi level only a 1.6%. The DOS at the Fermi level is thus dominated by boron p orbitals. Bands above approximately 2 eV above the Fermi level at Γ do have, on the contrary, some considerable H character.

The hole pocket centered at Γ and the electron pocket centered at Y are evident in the Fermi surface of Fig. 4.5. Both pockets are ellipsoidal, but, due to the semimetallic character of HB, the area enclosed by the pockets is small. Indeed, the system is not far from an insulating state, as it has been suggested that a gap can be opened with a small strain [Mortazavi et al., 2018].

4.2.2 Phonon spectra and the electron-phonon interaction

We have calculated the phonon bands and the phonon DOS (PDOS), as well as the projection of the PDOS onto boron and hydrogen atoms (see Fig. 3.6). As expected for a 2D material [Katsnelson and Fasolino, 2013], the flexural out-of-plane acoustic mode has a quadratic dispersion due to rotational symmetry. The phonon spectrum has three distinctive regions. Below ∼700 cm^{-1} there are

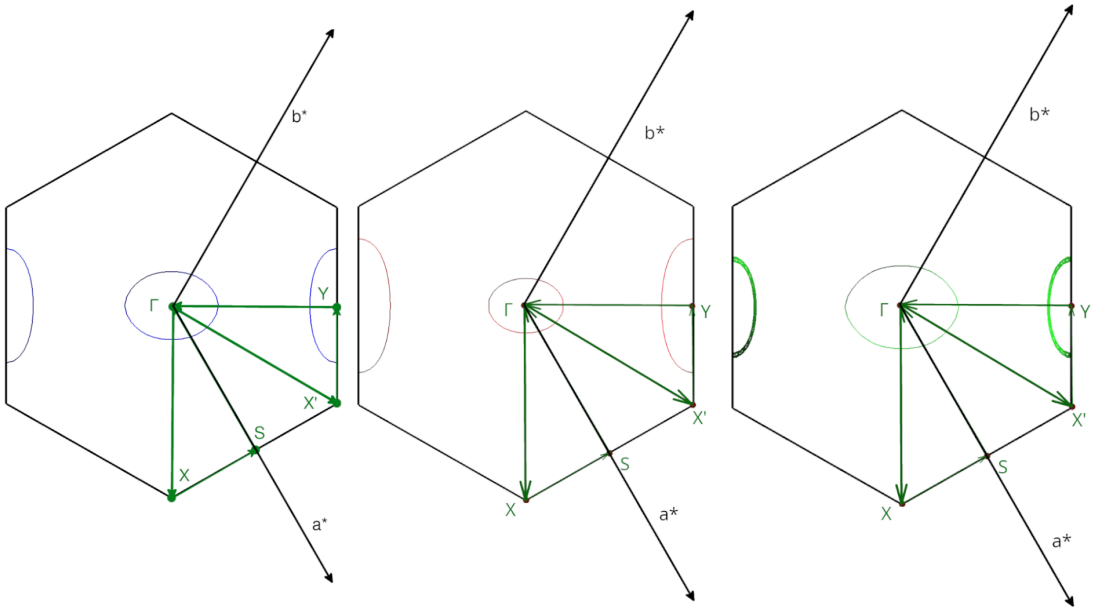

Figure 4.5: Fermi surfaces for the non doped system (left), the one doped with electrons (center), and the one with holes (right) for $Cmmm$ HB. High-symmetry points are marked in green. Reciprocal lattice vectors $\mathbf{a}^*$ and $\mathbf{b}^*$ are included as well. The path used for the calculation of the electronic bands and phonon spectra is illustrated.

three acoustic and another three optical modes. These modes show, in general, a mixed character between hydrogen and boron. The hydrogen character of these low-energy modes comes from the vibrations of H atoms along the y direction. At higher energies, between approximately 750 cm^{-1} and 1100 cm^{-1}, there are two isolated phonon bands that describe in-plane boron vibrations, reminiscent of the E_{2g} modes that are strongly coupled to the electrons in the similar MgB_2 [Choi et al., 2002,An and Pickett, 2001,Yildirim et al., 2001]. For comparison, the energy of the E_{2g} mode in MgB_2 is around 600 cm^{-1} [d'Astuto et al., 2007], smaller than the analogous modes in HB. The remaining four phonon modes appear after a large energy gap above 1500 cm^{-1} and have a dominant hydrogen character, with vibrations along the x and z directions.

As we can observe in Fig. 4.7, where the Eliashberg function $\alpha^2F(\omega)$ and the integrated electron-phonon coupling constant $\lambda(\omega)$ are shown, phonon modes with energies between 500 and 1000 cm^{-1} contribute the most to the electron-

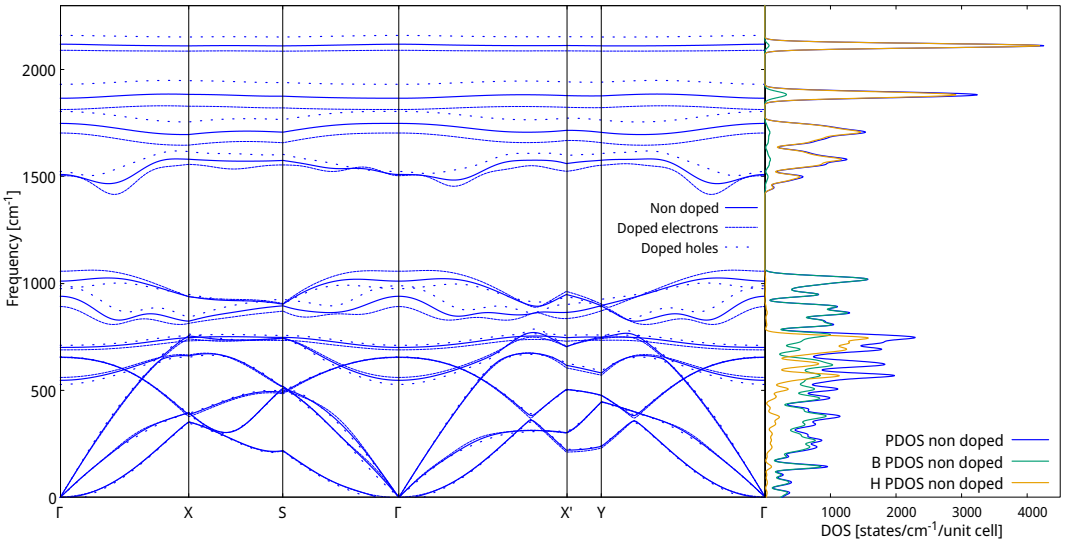

Figure 4.6: Phonon spectrum (left panel) for the non doped *Cmmm* HB, together with the doped cases with electrons and holes. The phonon density of states (PDOS) (right panel) is plotted, including also its decomposition onto different atoms, only for the non doped case. The PDOS decomposition is similar in the doped cases.

phonon coupling. The modes mainly contributing to the peaks in this energy range involve boron and hydrogen displacements, as well as the in-plane pure boron modes, analogous to the E_{2g} of MgB_2. There is another significant peak at around 1500 cm^{-1}, related to hydrogen-character modes, but, as expected, the lower frequency modes are the ones that contribute most to the electron-phonon coupling. Unfortunately, the integrated electron-phonon coupling λ reaches a very low value of approximately 0.2, which yields a very low superconducting T_c of only 11 mK with $\mu^* = 0.080$.

4.2.3 Doping

The DOS of 2D materials is energy independent in the free electron-like limit and, thus, since λ is proportional to $N(\epsilon_F)$, doping is expected not to affect the electron-phonon coupling constant. However, there are examples in the literature where electrostatic doping has been used to induce superconductivity in two-dimensional materials such as amorphous bismuth [Parendo et al., 2006] or the

$LaIO_3/SrTiO_3$ interface [Caviglia et al., 2008], in analogy to the common behavior of the cuprates [Ahn et al., 1999]. Also, this FET doping mechanism has been used to induce and tune superconductivity in transition metal dichalcogenides [Saito et al., 2016], for instance in MoS_2, where doping induces first an insulator to metal transition, and a superconducting state at further electron doping, with a T_c that can reach a value as high as 10 K [Saito et al., 2015].

Motivated by these experimental results and the possibility of FET doping two-dimensional materials in the laboratory, we have studied the effect of both electron and hole doping in the structural, electronic, phononic, and superconducting properties of *Cmmm* HB, with the hope that its low T_c may be enhanced. In the following we report the results obtained with electron and hole doping, which will be referred as the electron/holes doped cases respectively. We dope the system with 0.075 electrons(holes) per unit cell, which corresponds to a 9.39×10^{13} electrons(holes)/cm^2.

By relaxing the structure before with DFT in the doped system, we can determine how the structure and the bonding are affected when extra electrons or holes are included in the system. The modified structural parameters are summarized in Table 4.1. Doping leaves the lattice parameter a unvaried, but increases the γ angle when electrons are added and decreases it if, instead, extra holes are present. Similarly, the distance of hydrogen from the plane decreases in the electron doped case, while increases in the hole doped case. These results suggest that electron doping strengthens the B-B and B-H-B covalent bonds.

We report the electronic bands, together with the DOS, in Fig. 4.4. We observe that, as expected, the conduction bands of the electron doped case tend to go down with respect to the non doped case, while the bands of the holes doping tend to go up with respect to the non doped case. The effect is that in the electron doped case the hole pocket at Γ decreases and the electron pocket at Y increases. The opposite happens in the hole doped case. This effect is clear in the Fermi surface in Fig. 4.5. The character of the bands is barely affected by the doping and the percentage of H states in the DOS at the Fermi energy remains minimal, as in the non doped case. Indeed, with the doping values assumed, $N(\epsilon_F)$ remains practically unchanged, which is reasonable given the constant DOS in the vicinity of the Fermi level.

As we can see in Fig. 4.6, electron or hole doping barely affects the lowest

six phonon modes. The differences become more appreciable for the isolated two boron in-plane bands in the frequency range between 750 and 1100 cm^{-1}. Electron doping increases the splitting between these two modes, while hole doping decreases it. Finally, the hydrogen-dominated modes at high energies are softened in the electron doped case and hardened in the hole doped case.

Taking a look at the values of the Eliashberg function $\alpha^2F(\omega)$ and the integrated electron-phonon coupling constant $\lambda(\omega)$, plotted in Fig. 4.7, we can see that in the doped cases still the modes in the 500-1000 cm^{-1} range are those with the most important contribution to λ. However, specially the low-energy acoustic modes, are more coupled to the electrons in the hole doped case. Also the modes in the 500-1000 cm^{-1} range seem to be more prone to the electrons in the doped cases. We attribute these differences to the change in the electron-phonon coupling matrix elements and not to the shift of the phonon frequencies. The slight changes in the bonding pattern can explain a subtle change of the electron-phonon matrix elements themselves. Nevertheless, doping, either hole or electron, is not able to enhance λ sufficiently to reach a sizable critical temperature in HB. The value of T_c in the hole doped case is 21 mK with $\mu^* = 0.080$. Thus, despite the opposite is the case in other systems, doping does not seem to be an efficient strategy to increase the critical temperatures in hydrogen boride, at least, in the $Cmmm$ phase synthesized experimentally.

4.3 Conclusions

Neither the non doped nor the doped HB present a sizable superconductivity in the $Cmmm$ phase. This can be traced to a variety of reasons. It has been recently argue [Belli et al., 2021] that hydrogen-based compounds can reach a high T_c when an electronic bonding network between localized units is created. The *networking value* ϕ, which was defined as the highest value of the ELF that creates an isosurface spanning through the whole crystal in all three Cartesian directions, measures precisely that network. By multiplying the networking value with the fraction of hydrogen in the compound H_f (0.5 for HB) and with the third root of the hydrogen fraction of the total DOS at the Fermi energy H_{DOS}, i.e. defining $\Phi_{\mathrm{DOS}} = \phi H_f \sqrt[3]{H_{\mathrm{DOS}}}$, a rather good correlation was obtained between Φ_{DOS} and T_c, capable of estimating the critical temperature with the empirical [Belli et al.,

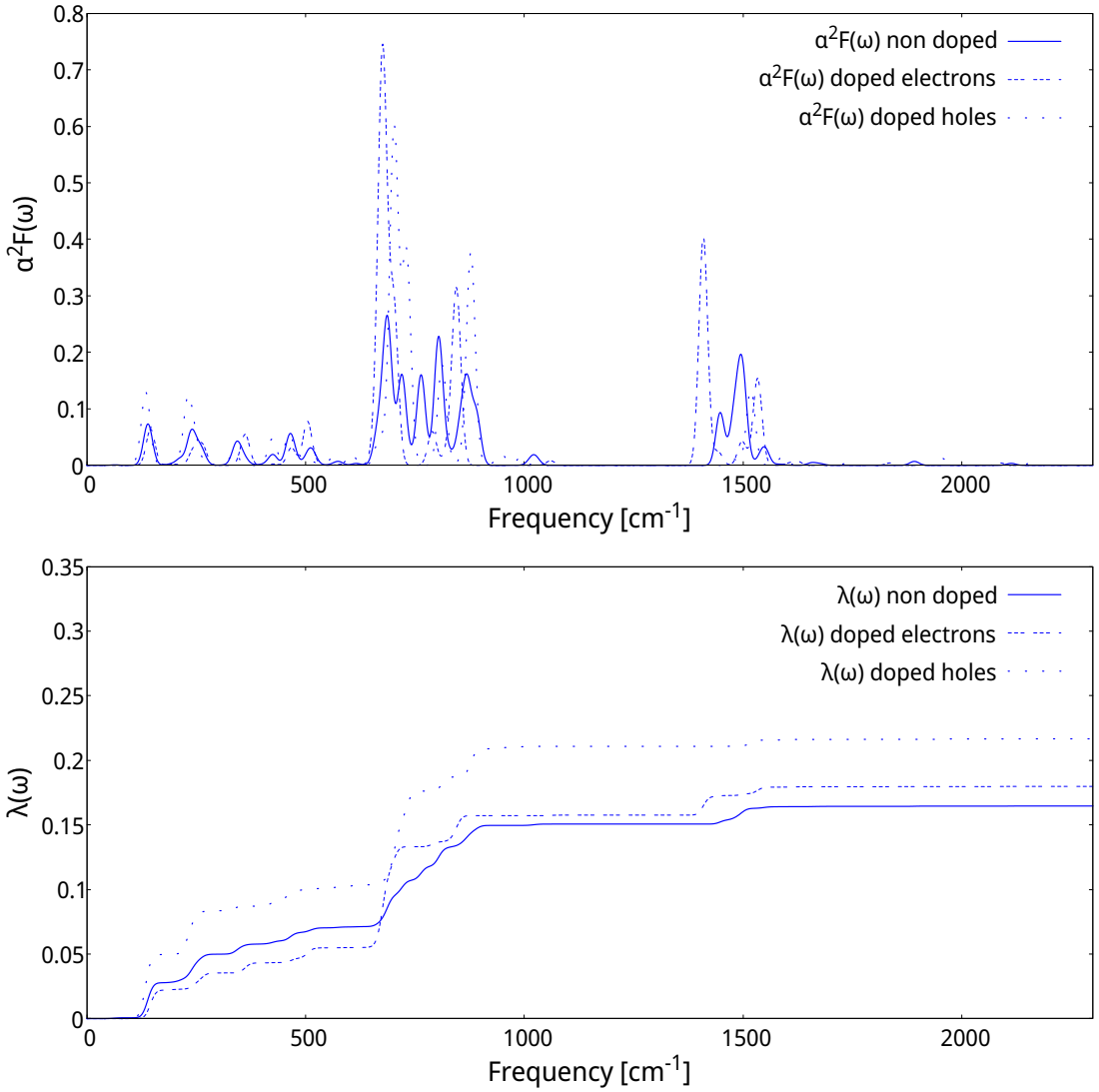

Figure 4.7: Eliashberg function $\alpha^2F(\omega)$ and integrated electron-phonon coupling constant $\lambda(\omega)$ for the non doped system, as well as the doped systems with electrons and holes.

2021]

$$T_c = (750\Phi_{\mathrm{DOS}} - 85)\mathrm{K} \tag{4.3.1}$$

equation. Here we assume that the networking value in a 2D system should be determined by the highest value of the ELF that creates an isosurface that expands in the whole crystal in the plane. With this adapted definition we obtain $\phi = 0.53$, a rather large value. However, the fact that the hydrogen fraction of the DOS at

the Fermi level is so low in this system suppresses all the T_c according to Eq. (4.3.1), both in the undoped and doped cases.

Furthermore, the presence of hydrogen alters the bonding of the boron layer creating the B-H-B bridges. This fact suppresses the electron-phonon coupling of the boron in-plane modes due to the large impact that the presence of hydrogen has in the band structure [Tateishi et al., 2019,Kawamura et al., 2019]. Therefore, the presence of hydrogen also suppresses the electron-phonon coupling in the boron layer itself. Hydrogen doping of borophene is not thus favoring the emergence of high-temperature superconductivity in hydrogen boride, it has the opposite effect at least in the $Cmmm$ phase.

From the results of our analysis we can conclude that, despite the large expectations in the literature [Tateishi et al., 2019], hydrogen boride is not a strongly coupled superconductor mainly because of the weak hydrogen character of the density of states at the Fermi level and the effect of the presence of hydrogen in the bonding of the boron layer. The T_c values are not sizable, below 1 K, even if the system is doped. Our results suggest that hydrogenated monolayers will be high-temperature superconductors, comparable in their T_c's to high-pressure superhydrides, only if the electronic states at the Fermi level have a large hydrogen character.

Chapter 5

Chain of poliacenes

The last compound that we study is an organic compound, a poliacene chain: a one dimensional chain formed by nine benzene rings, the nonacene. Organic compounds present two possible mediators for superconductivity: electron-phonon coupling and magnetic fluctuations. In this chapter, we study the structure of this chain, with particular attention to its magnetic behaviour.

The general formula for a poliacene chain with N rings is $C_{4N+2}H_{2N+4}$, and the biggest chain that has been experimentally studied is formed by 12 benzene rings. One of the main challenges for studying poliacene chains is the high sensitivity of the system, requiring high precision in numerical studies. In particular, there is a very small gap between the Highest Occupied Molecular Orbitals (HOMO) and the Lowest Unoccupied Molecular Orbitals (LUMO), of the order of 0.3 eV or 10^{-2} Ha [Tönshoff and Bettinger, 2021]. Due to this small energy difference, calculations that are not accurate enough fail to distinguish between the ground state and the first excited state of the system, and the precision needed grows with the length of the chain. Due to this reason, nowadays there are not many studies on the chains longer than six rings. A possible approach could be an open-shell method that takes into account the very tiny energy differences between HOMO and LUMO. In fact, starting from hexacene, the molecule is strongly sensitive and the results on the ground state wave function can be method dependent if the computation is not accurate enough: in particular, in [Tönshoff and Bettinger, 2021] it is stated the ground state for the nonacene is not correctly predicted by methods as Hartree-Fock and DFT, so Monte Carlo approaches can be considered to improve on this

result. In addition, in [Genovese et al., 2020] the benzene molecule was studied with quantum Monte Carlo approaches, and the results were found to be in agreement with configuration interaction (CI) results [Chakravorty et al., 1993]. For larger molecules, CI approaches are computationally too expensive, but the application of quantum Monte Carlo approaches is worth considering, given the results on the benzene molecule.

In Monte Carlo approaches a problem is the optimization of the geometry: as we have to optimize both the geometry and the wave functions in order to have a very accurate result, the computational cost can be high. This is because, if we change the geometry, then the starting wave function is not any more an eigenvector of the spin operator S^2. This can lead to a spin contamination [Tönshoff and Bettinger, 2021] and an error that is larger for extended chains as the energy difference between the singlet and the triplet increases with the dimension of the system, i.e. with the number of rings. If this kind of non physical error happens (i.e. infinite energy gap between singlet and triplet for an infinite chain), we are considering a very high contribution of static energy correlation and the approach that we are using is not correct.

Recently, in [Genovese et al., 2020] it was shown that in a benzene molecule the singlet state is the ground state of the system and that spin fluctuations are negligible. This means that the behaviour of the system is paramagnetic. Instead, for an infinite chain [Meena et al., 2022] in a zig-zag graphene configuration, we have, on the contrary, an antiferromagnetic behaviour. More generally, a spin triplet instability associated with antiferromagnetic behaviour for number of rings larger than eight has been predicted [Tönshoff and Bettinger, 2021]. This gives us another motivation to study the magnetic behaviour of nonacene, as finding an antiferromagnetic behaviour would mean that there is a length of the chain under 9 rings at which the behaviour flips from paramagnetic to antiferromagnetic.

In this chapter, we use quantum Monte Carlo methods to examine the ground state of the nonacene chain, building an appropriate wave function that can be used to describe the various properties of the system, focusing in particular on the magnetic behaviour. Our goal is to contribute to the understanding of the ground state of this potential organic superconductor.

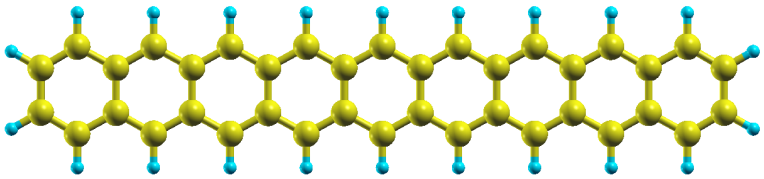

Figure 5.1: Nonacene chain, with carbon atoms in yellow and hydrogen atoms in light blue.

5.1 Methods and computational details

In our work we are focusing on zig-zag poliacene chains of nine rings, called nonacene, with formula $C_{38}H_{22}$. We picture the nonacene chain in figure 5.1. We analysed this chain within quantum Monte Carlo (QMC) methods, and particularly variational Monte Carlo (VMC) and lattice regularized diffusion Monte Carlo (LRDMC) described in section 2.2 using the software TurboRVB [Nakano et al., 2020].

We choose a basis and construct various wave functions. We can then use VMC and LRDMC to compute the energies of those wave functions, also employing the optimization procedure described in section 2.2. After comparing the energies, we take the wave function with the smallest energy as the best approximation for the ground state. We now give a summary of the wave functions that we have used: for more details, see section 2.3.

We have used the following wave functions: single determinant, (SD), antisymmetrical geminal power (AGP) and Pfaffian wave functions. We have used the SD wave function with the spin in singlet or triplet configuration, to represent respectively paramagnetic and antiferromagnetic behaviour of the system. The AGP wave function takes into account the interactions between the couples of electrons, so we can use those types of wave functions to describe paramagnetic systems and pairwise bonds with $S^2 = 0$, i.e. the singlet state. We also notice that the AGP functions contain all the possible configurations between bondings. Lastly, we have used Pfaffian wave functions. The latter is a very generic wave function that can describe bondings between parallel and antiparallel spin. As a result, the projection along the z axis of the spin S_z can be different from zero and we can have the so called spin vibrations or fluctuations [Becca and Sorella,

2017]. Obviously, computing the energy associated to Pfaffian wave functions has a higher computational cost as they are more generic compared with the previous ones. In fact, we can observe that AGP are a particular case of the Pfaffian. While the Pfaffian case admits all possible spin pairings between electrons, AGP wave functions only admit singlet pairings.

We construct the Jastrow factor (described in subsection 2.3.2) in the same manner for all the wave functions, and then we optimized it considering all the parts involved in the description of the wave function. We have denoted the wave functions with the Jastrow factor as JSD, JAGP and JPfaffian. After the construction of the Jastrow factor and SD/AGP/Pfaffian upon the chosen basis set, we can optimize the parameters in order to obtain the minimum of the energy, allowing the geometry of the system to change. Using those new parameters that minimize the energy we can obtain the optimized wave function and the new geometry of the system. At the end of this optimization procedure we can obtain the geometry, the parameters that describe the ground state wave function, and determine the ground state energy of the system.

5.2 Results

We have studied a nine rings benzene chain. We have used a JSD trial wave function, both with the spin part in a singlet and triplet configuration. We have observed that the lowest energy between those two configurations is obtained with the wave function in an antiferromagnetic configuration, i.e. triplet spin for the ground state. This has been verified at both VMC and LRDMC level.

After that we have used JAGP and JPfaffian trial wave functions. The first one, JAGP, describes the characteristic of a paramagnetic system while the second one, JPfaffian, is very generic and contains static spin fluctuations respect to the equilibrium position. For all those trials wave functions we have optimized not only the wave function itself but also the geometry of the system. This means that we have also changed the geometry parameters that enter in the construction of the wave function.

At the end, we have compared the energies obtained with those different wave functions (as it can be observed in table 5.1), and we have found that the lowest

Wavefunction	VMC energy (Ha)	σ_{VMC} (Ha)
JSD antiferromagnetic	-228.94956	0.00090
JSD paramagnetic	-228.83710	0.00067
JAGP paramagnetic	-228.85278	0.00075
JPfaffian	-228.96295	0.00067

Wavefunction	LRDMC energy (Ha)	σ_{LRDMC} (Ha)
JSD antiferromagnetic	-229.32285	0.00247
JSD paramagnetic	-229.30064	0.00316
JAGP paramagnetic	-229.30958	0.00312
JPfaffian	-229.32366	0.00245

Table 5.1: Full energies (in Hartree) and estimate of errors for the various trial wave functions that we have analysed. We have considered a chain with 38 carbon atoms.

energy is obtained using the JPfaffian wave function. This is not surprising as both AGP and SD are particular cases of the Pfaffian wave function. As an example, the AGP is obtained considering only the interactions of coupled electrons, i.e. between the $N_e/2$ electrons of spin up and $N_e/2$ with spin down (where N_e is the number of electrons). Instead SD is a particular case of AGP and Pfaffian, and it considers a single determinant built starting from molecular orbitals. Those molecular orbitals can be calculated within density functional theory or Hartree-Fock theory. In our case after calculating those orbitals with DFT we have optimized them within QMC.

We can find the results obtained in table 5.1. From the table we can see that, even if the lower energy is obtained with the JPfaffian, the JSD wave function in antiferromagnetic configuration describes very well the system, with only a 0.006% difference between them in the VMC case and 0.004% in the LRDMC case, and the computational cost of the JSD wave function is lower compared with the Pfaffian ones. This means that the behaviour of the system is antiferromagnetic.

We can analyse if there are spin fluctuations. From figure 5.2 we can observe that there are not spin fluctuations and that, consequently, the system is an antiferromagnet without spin fluctuations, with spin moments centered at the carbon atoms. Same arguments are true for the energies obtained at LRDMC level.

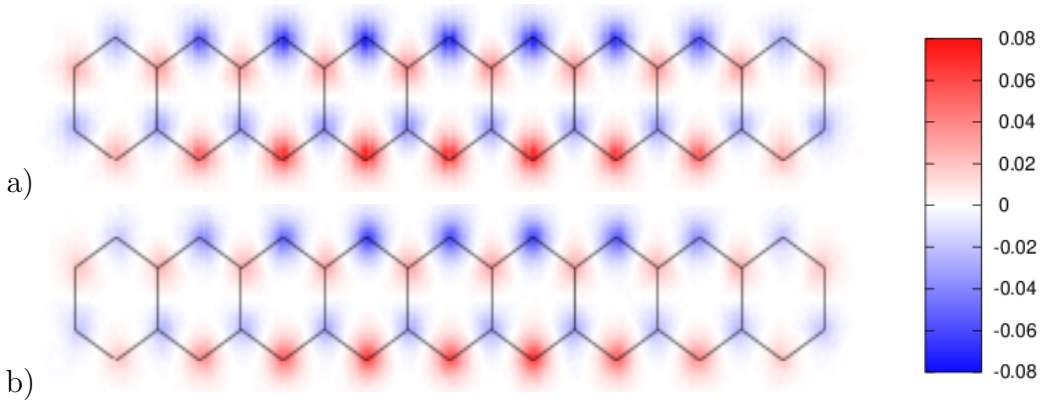

Figure 5.2: Spin density for the nonacene chain obtained with the tested wave functions. Figure a) is the spin density for the JSD antiferromagnetic wave function, figure b) is the spin density for the JPfaffian wave function.

Analysing more in details the results obtained we have that, comparing the VMC results, the difference in energy between JSD antiferromagnetic and JPfaffian is of 0.35 mHa per carbon atom, while the difference between JSD antiferromagnetic and JSD paramagnetic is of 2.96 mHa per carbon atom. The difference between JAGP paramagnetic and JPfaffian is of 2.90 mHa per carbon atom, similar to the JSD paramagnetic result. Same analysis can be done at LRDMC level, from which we obtain 0.02 mHa per carbon atom for the difference between JSD antiferromagnetic and JPfaffian, and 0.58 mHa per carbon atom for the difference between JSD antiferromagnetic and paramagnetic. Again, the difference between JAGP paramagnetic and JPfaffian is similar to the JSD paramagnetic case, with a difference of 0.37 mHa per carbon atom. Furthermore, as evident from figure 5.2, we notice the peaks of the spin density are more pronounced in the JSD antiferromagnetic case than in the JPfaffian case, but the difference is small and, other than that, the densities are similar. Given the small differences between the two descriptions, it is preferable to use the JSD antiferromagnetic wave function due to the notably smaller computational cost.

By taking the structures optimized on the different wave functions, we can observe that they do not change much. In particular, the bonds between the carbon atoms vary only by factors not exceeding 1.4%, and the bonds between carbon and hydrogen atoms vary by factors not exceeding 0.4%. We have summarized the minimum and maximum bonds in table 5.2, but as the wave functions have different variational parameters, those bonds do not give information on the quality

	C-C min distance (Bohr)	C-C max distance (Bohr)
JSD antiferromagnetic	2.56871	2.69064
JSD paramagnetic	2.54696	2.72237
JAGP paramagnetic	2.56620	2.69111
JPfaffian	2.54153	2.72849

	C-H min distance (Bohr)	C-H max distance (Bohr)
JSD antiferromagnetic	2.04077	2.04202
JSD paramagnetic	2.03729	2.04160
JAGP paramagnetic	2.04010	2.04470
JPfaffian	2.03182	2.03578

Table 5.2: Minimum and maximum C-C distances and C-H distances (in Bohr) for the wave functions.

of the wave functions themselves.

As further confirmation of the behaviour of the system we can check the differences in energy obtained using JAGP paramagnetic wave function and JSD antiferromagnetic wave functions and see that this last one has a lower energy with respect to the JAGP one of 2.55 mHa per carbon atom at VMC level and 0.35 mHa per carbon atom at LRDMC level. All these analyses are summarized in table 5.3, from which we can have a clear overview of the energy differences.

5.3 Conclusions

The first important result of this study is the computation of the energy of the nonacene chain with the different wave functions. We have compared various wave functions, describing both an antiferromagnetic and a paramagnetic system, and also comparing the results with a Pfaffian approach that generalizes the two behaviours. From our energies, we can conclude that the energy differences between the JSD antiferromagnetic and the JPfaffian wave function are of order 10^{-2} Hartree in the VMC case, and 10^{-4} Hartree in the LRDMC case. We have used the optimization procedure of section 2.2 to generate the wave functions, so we have used the same wave functions in VMC and LRDMC and the energy difference only

VMC energies (Ha)	JSD anti	JSD para	JAGP para	JPfaffian
JSD anti	×	-0.11246	-0.09678	0.01339
JSD para	0.11246	×	0.01568	0.12585
JAGP para	0.09678	-0.01568	×	0.11017

LRDMC energies (Ha)	JSD anti	JSD para	JAGP para	JPfaffian
JSD anti	×	-0.02221	-0.01327	0.00081
JSD para	0.02221	×	0.00894	0.02302
JAGP para	0.01327	-0.00894	×	0.01408

Table 5.3: Energy differences in Hartree (each entry is energy in row minus energy in column) for the various wave functions for both VMC and LRDMC.

comes from the difference in method. The VMC result is comparable with the expected order of magnitude for an HOMO-LUMO difference (10^{-2} Hartree), while the LRDMC result is smaller than that difference. In the LRDMC case, we can say that as the difference is smaller than the HOMO-LUMO order of magnitude, the two wave functions are a good approximation of the ground state of the system. On the other hand, the results from the paramagnetic wave functions are notably worse, so we can state that the system has an antiferromagnetic behaviour.

Regarding the spin fluctuations, we observe that there is a small energy difference between the JSD antiferromagnetic wave function (that does not contain spin fluctuation) and the JPfaffian wave function (that can contain spin fluctuations). We can then assume that the spin fluctuations for the ground state are small.

It is worth noting that, while we find an antiferromagnetic behaviour for the chain of nine rings, in [Genovese et al., 2020] it was found that the benzene molecule has a paramagnetic behaviour, while we find a different magnetic behaviour for our chain. We can assume that there is a certain length of the chain at which the magnetic behaviour changes, and this is a possible future line of research. This is an ulterior sign of the high sensitivity of the system, where small differences of the setup can bring to very different macroscopic behaviour.

Conclusions

In this thesis, we have studied from first principles the superconductive properties of hydrogen based compounds at ambient pressure. The work done in this thesis is a contribution to understanding the role of hydrogen in superconductivity, and constitutes a basis for further works to expand on the results that we obtained. The goal of our work is to study systems that are able to attain high temperature superconductivity at ambient pressure. The compounds that we have studied do not have this property. Nevertheless, our results can be used to understand which factors are important for high temperature superconductivity, and which factors are detrimental to it. Even if we did not manage to attain all the results that we hoped for, we have to keep in mind that this is a very challenging field, but it is a field worth studying, as it could have enormous repercussion from both scientific and technological points of view.

For the palladium hydride system, we have successfully demonstrated the existence of metastable configurations, in which hydrogen atoms can also occupy tetrahedral positions. We have also underlined the importance of anharmonic and quantum effects in constructing those structures. This result enriches the possibilities of study for this compound, as configurations different from the full octahedral one can be analysed from a theoretical and experimental perspective. We have analysed the effect of this variation in occupation in the critical temperature, showing that structures with a full octahedral configuration favour superconductivity, and tetrahedral occupation suppresses it. The compound with full octahedral occupation presents softer phonons with respect to compounds that also have tetrahedral occupation, and this is a factor contributing to the result that octahedral occupation enhances the superconducting critical temperature. Ultimately, the absence of high temperature superconductivity can be explained by the weak hydrogen character of the density of states at the Fermi level. In the future, it will

surely be interesting to analyse more structures with varied configurations.

Regarding hydrogen boride, we have found that, contrary to expectations, neither non doped nor doped hydrogen boride show high temperature superconductivity. We have explained this result by analysing the character of the bands at the Fermi level, showing that there is a prevalent boron character. Hydrogen works against the electron-phonon coupling of the boron modes, suppressing an important contribution to superconductivity. We have also interpreted this result using the electron localization function, further showing that the low concentration of hydrogen at the Fermi level is responsible for the absence of superconductivity. As we have studied the $Cmmm$ phase exclusively, it will be important for the future of this compound to study superconductive properties of other phases.

Lastly, for the nonacene chain, we have constructed a wave function that describes the ground state with a good accuracy, showing that the results obtained with a JSD antiferromagnetic wave function are very near to the results obtained with a JPfaffian wave function. This implies that the nine ring chain has an antiferromagnetic behaviour. The presence of magnetism can be relevant in superconductivity, as it can bring to spin-fluctuation driven superconductivity. As the single benzene molecule has a paramagnetic behaviour, a possible future direction would be to study the magnetic behaviour of the intermediate chains, looking for a point in which this behaviour flips from paramagnetic to antiferromagnetic character. In addition, a study of the superconductive properties of the nonacene chain can be made based on our ground state wave function, with particular attention to the effects that polyacene intercalation in crystals can have in their superconductive properties.

From our work, we can also draw some general conclusions. The analysis on palladium hydride and hydrogen boride shows that strong hydrogen character is necessary in the bands at the Fermi level in order to have high critical temperature, a characteristic that is not present in our systems. We can also point out that metal hydrides with H atoms at interstitial sites are not very promising for high temperature superconductivity at ambient pressure.

A second general conclusion is that soft phonons enhance the critical temperature in this kind of compounds. We have tried to create the conditions for soft phonons by studying and changing the characteristics of our systems. In particular, for palladium hydride we have modified the position of hydrogen atoms,

while for hydrogen boride we have used doping, but other means could be used to achieve this end.

In general, more studies on those compounds and the properties that characterise them are necessary to reach the goal of high temperature superconductivity at ambient pressure. This would give an important drive to new technologies, contributing in a decisive manner to the development of technology to all levels, from specialised to everyday applications.

List of PhD publications

1. *Absence of sizable superconductivity in hydrogen boride: A first principles study*
   Antonella Meninno, Ion Errea
   Physical Review B 106, 172501 (2022)

2. *Magnetic order in a coherent two-dimensional Kondo lattice*
   Wen Wan, Rishav Harsh, Antonella Meninno, Paul Dreher, Sandra Sajan, Ion Errea, Fernando de Juan, Miguel M. Ugeda
   arXiv preprint (2022)

3. *Ab initio study of metastable occupation of tetrahedral sites in palladium hydrides and its impact on superconductivity*
   Antonella Meninno, Ion Errea
   Physical Review B 107, 024504 (2023)

Acknowledgments

First of all I have to thank my supervisor, Ion Errea, with whom I worked in these years. My heartfelt gratitude also goes to Michele Casula, who was my tutor during my internship in Paris, and I would also like to acknowledge his indirect help in writing my master thesis. I would not have done it without his papers and his manuals on how to use TurboRVB. I would also like to express my gratitude towards Sandro Sorella who encouraged me to take this road, and unfortunately is among us no more.

Another thank you goes to the a person to whom everyone in the scientific community should be grateful, Aleksandra Asanovna Ėlbakjan.

I find it very difficult to acknowledge the support of every person that I have known during these years, as I would surely forget someone.

I would like to start with a part of my PhD that was small in time but surely very important for my growth. I appreciate all the people that I have met in Paris, in particular for all the beers on Friday nights in Jussieu along the Seine, for all the conversations and for the fantastic party that you organized for my birthday. Thank you, you made this experience wonderful.

I would like to thank my friends in Donostia, as without them my life here would surely have been different. I am grateful to all the persons with which I have had the pleasure of having breakfast together, for the walks on the seafront or around CFM, those moments have been precious. I would also like to say something to the persons with whom I have shared countless coffees, lunches and all the conversations that sprang from them: you all enriched me. My appreciation also go to my friends for the various afternoons on Saturday spent discussing religion, philosophy and love, you opened me up to a world of joy. Last but not

least, I am indebted to persons with whom I have spent nights out, in cider houses and on the beaches, in festivals and theatre performances, you gave me emotions that I will always bring with me.

I would like to state my appreciation towards my family. My mother who always supported me from afar, and my father who taught me to go onwards in every circumstance. Many thanks to Palma who showed me different points of view, and to my nephews Pasquale and Diego who gave me joy and happiness. A particular thank you goes to my brother who always encouraged me and supported me during difficult moments. Last, I would thank Salvatore for our twelve years of friendship, in which we have developed the same ideas and values.

Bibliography

[Ahn et al., 1999] Ahn, C., Gariglio, S., Paruch, P., Tybell, T., Antognazza, L., and Triscone, J.-M. (1999). Electrostatic modulation of superconductivity in ultrathin gdba2cu3o7-x films. *Science*, 284(5417):1152–1155. 96

[Alefeld and Völkl, 1978] Alefeld, G. and Völkl, J. (1978). Hydrogen in metals i-basic properties. *Berlin and New York*, 28. 69

[Allen and Dynes, 1975] Allen, P. B. and Dynes, R. (1975). Transition temperature of strong-coupled superconductors reanalyzed. *Physical Review B*, 12(3):905. 33, 89

[Allen and Mitrović, 1983] Allen, P. B. and Mitrović, B. (1983). Theory of superconducting tc. In *Solid state physics*, volume 37, pages 1–92. Elsevier. 33, 89

[An and Pickett, 2001] An, J. and Pickett, W. (2001). Superconductivity of mgb 2: covalent bonds driven metallic. *Physical Review Letters*, 86(19):4366. 94

[Ashcroft, 1966] Ashcroft, N. (1966). Electron-ion pseudopotentials in metals. *Physics Letters*, 23(1):48–50. 23

[Bardeen et al., 1957] Bardeen, J., Cooper, L. N., and Schrieffer, J. R. (1957). Theory of superconductivity. *Physical review*, 108(5):1175. 8

[Baroni et al., 2001] Baroni, S., de Gironcoli, S., Dal Corso, A., and Giannozzi, P. (2001). Phonons and related crystal properties from density-functional perturbation theory. *Rev. Mod. Phys.*, 73(2):515–562. 72, 89

[Baroni et al., 1987] Baroni, S., Giannozzi, P., and Testa, A. (1987). Green's-function approach to linear response in solids. *Physical review letters*, 58(18):1861. 89

[Becca and Sorella, 2017] Becca, F. and Sorella, S. (2017). *Quantum Monte Carlo approaches for correlated systems*. Cambridge University Press. 40, 45, 54, 103

[Bekaert et al., 2019] Bekaert, J., Petrov, M., Aperis, A., Oppeneer, P. M., and Milošević, M. (2019). Hydrogen-induced high-temperature superconductivity in two-dimensional materials: the example of hydrogenated monolayer mgb 2. *Physical review letters*, 123(7):077001. 3, 9, 87

[Belli et al., 2021] Belli, F., Novoa, T., Contreras-García, J., and Errea, I. (2021). Strong correlation between electronic bonding network and critical temperature in hydrogen-based superconductors. *Nature Communications*, 12(1):1–11. 84, 97

[Belov et al., 2015] Belov, M., Syzdykova, A., Vekilov, Y. K., and Abrikosov, I. (2015). Hydrogen in palladium: Anharmonicity of lattice dynamics from first principles. *Physics of the solid state*, 57(2):260–265. 2, 9

[Bianco et al., 2017] Bianco, R., Errea, I., Paulatto, L., Calandra, M., and Mauri, F. (2017). Second-order structural phase transitions, free energy curvature, and temperature-dependent anharmonic phonons in the self-consistent harmonic approximation: Theory and stochastic implementation. *Physical Review B*, 96(1):014111. 63, 66, 68

[Blanco-Rey et al., 2014] Blanco-Rey, M., Juaristi, J., Muiño, R. D., Busnengo, H. F., Kroes, G.-J., and Alducin, M. (2014). Electronic friction dominates hydrogen hot-atom relaxation on pd (100). *Physical review letters*, 112(10):103203. 75

[Bloch, 1929] Bloch, F. (1929). Über die quantenmechanik der elektronen in kristallgittern. *Zeitschrift für physik*, 52(7):555–600. 20

[Born and Heisenberg, 1985] Born, M. and Heisenberg, W. (1985). Zur quantentheorie der molekeln. In *Original Scientific Papers Wissenschaftliche Originalarbeiten*, pages 216–246. Springer. 12

[Brumme et al., 2014] Brumme, T., Calandra, M., and Mauri, F. (2014). Electrochemical doping of few-layer zrncl from first principles: Electronic and structural properties in field-effect configuration. *Physical Review B*, 89(24):245406. 90

[Brumme et al., 2015] Brumme, T., Calandra, M., and Mauri, F. (2015). First-principles theory of field-effect doping in transition-metal dichalcogenides:

Structural properties, electronic structure, hall coefficient, and electrical conductivity. *Physical Review B*, 91(15):155436. 90

[Caputo and Alavi, 2003] Caputo, R. and Alavi, A. (2003). Where do the h atoms reside in pdh x systems? *Molecular Physics*, 101(11):1781–1787. 75

[Carbotte, 1990] Carbotte, J. (1990). Properties of boson-exchange superconductors. *Reviews of Modern Physics*, 62(4):1027. 33

[Casula et al., 2011] Casula, M., Calandra, M., Profeta, G., and Mauri, F. (2011). Intercalant and intermolecular phonon assisted superconductivity in k-doped picene. *Physical Review Letters*, 107(13):137006. 3, 10

[Casula et al., 2005] Casula, M., Filippi, C., and Sorella, S. (2005). Diffusion monte carlo method with lattice regularization. *Physical review letters*, 95(10):100201. 54, 56

[Casula and Sorella, 2003] Casula, M. and Sorella, S. (2003). Geminal wave functions with jastrow correlation: A first application to atoms. *The Journal of Chemical Physics*, 119(13):6500–6511. 59

[Caviglia et al., 2008] Caviglia, A., Gariglio, S., Reyren, N., Jaccard, D., Schneider, T., Gabay, M., Thiel, S., Hammerl, G., Mannhart, J., and Triscone, J.-M. (2008). Electric field control of the laalo 3/srtio 3 interface ground state. *Nature*, 456(7222):624–627. 96

[Ceperley et al., 1981] Ceperley, D., Kalos, M., and Lebowitz, J. L. (1981). Computer simulation of the static and dynamic properties of a polymer chain. *Macromolecules*, 14(5):1472–1479. 54

[Ceperley and Alder, 1980] Ceperley, D. M. and Alder, B. J. (1980). Ground state of the electron gas by a stochastic method. *Physical review letters*, 45(7):566. 49

[Ceperley and Kalos, 1979] Ceperley, D. M. and Kalos, M. (1979). Monte carlo methods in statistical physics. *Topics in current physics*, 7:145. 53

[Chakravorty et al., 1993] Chakravorty, S. J., Gwaltney, S. R., Davidson, E. R., Parpia, F. A., and p Fischer, C. F. (1993). Ground-state correlation energies for atomic ions with 3 to 18 electrons. *Physical Review A*, 47(5):3649. 102

[Choi et al., 2002] Choi, H. J., Roundy, D., Sun, H., Cohen, M. L., and Louie, S. G. (2002). The origin of the anomalous superconducting properties of mgb2. *Nature*, 418(6899):758–760. 94

[Chowdhury and Ross, 1973] Chowdhury, M. and Ross, D. (1973). A neutron scattering study of the vibrational modes of hydrogen in the β-phases of pd-h, pd-10ag-h and pd-20ag-h. *Solid State Communications*, 13(2):229–234. 2, 9, 70

[Dal Corso, 2014] Dal Corso, A. (2014). Pseudopotentials periodic table: From h to pu. *Computational Materials Science*, 95:337–350. 71

[d'Astuto et al., 2007] d'Astuto, M., Calandra, M., Reich, S., Shukla, A., Lazzeri, M., Mauri, F., Karpinski, J., Zhigadlo, N. D., Bossak, A., and Krisch, M. (2007). Weak anharmonic effects in Mgb_2: A comparative inelastic x-ray scattering and raman study. *Phys. Rev. B*, 75:174508. 94

[Drozdov et al., 2015] Drozdov, A., Eremets, M., Troyan, I., Ksenofontov, V., and Shylin, S. I. (2015). Conventional superconductivity at 203 kelvin at high pressures in the sulfur hydride system. *Nature*, 525(7567):73–76. 1, 8

[Drozdov et al., 2019] Drozdov, A., Kong, P., Minkov, V., Besedin, S., Kuzovnikov, M., Mozaffari, S., Balicas, L., Balakirev, F., Graf, D., Prakapenka, V., et al. (2019). Superconductivity at 250 k in lanthanum hydride under high pressures. *Nature*, 569(7757):528–531. 1, 8

[Eichler et al., 1975] Eichler, A., Wühl, H., and Stritzker, B. (1975). Tunneling experiments on superconducting palladium-deuterium alloys. *Solid State Communications*, 17(2):213–216. 2, 9

[Eliashberg, 1960] Eliashberg, G. (1960). Interactions between electrons and lattice vibrations in a superconductor. *Sov. Phys. JETP*, 11(3):696–702. 8, 31, 89

[Elsässer et al., 1991] Elsässer, C., Ho, K., Chan, C., and Fähnle, M. (1991). Vibrational states for hydrogen in palladium. *Physical Review B*, 44(18):10377. 70, 75

[Errea et al., 2020] Errea, I., Belli, F., Monacelli, L., Sanna, A., Koretsune, T., Tadano, T., Bianco, R., Calandra, M., Arita, R., Mauri, F., et al. (2020).

Quantum crystal structure in the 250-kelvin superconducting lanthanum hydride. *Nature*, 578(7793):66–69. 79

[Errea et al., 2013] Errea, I., Calandra, M., and Mauri, F. (2013). First-principles theory of anharmonicity and the inverse isotope effect in superconducting palladium-hydride compounds. *Physical review letters*, 111(17):177002. 2, 9, 63, 70, 73, 78, 82, 84

[Errea et al., 2014] Errea, I., Calandra, M., and Mauri, F. (2014). Anharmonic free energies and phonon dispersions from the stochastic self-consistent harmonic approximation: Application to platinum and palladium hydrides. *Phys. Rev. B*, 89:064302. 63

[Feynman, 1939] Feynman, R. (1939). Phys rev 56: 340 https://doi. org/10.1103. 28

[Filippi and Umrigar, 1996] Filippi, C. and Umrigar, C. J. (1996). Multiconfiguration wave functions for quantum monte carlo calculations of first-row diatomic molecules. *The Journal of Chemical Physics*, 105(1):213–226. 45

[Foulkes et al., 2001] Foulkes, W., Mitas, L., Needs, R., and Rajagopal, G. (2001). Quantum monte carlo simulations of solids. *Reviews of Modern Physics*, 73(1):33. 46, 49, 52, 53

[Fukai, 2006] Fukai, Y. (2006). *The metal-hydrogen system: basic bulk properties*, volume 21. Springer Science & Business Media. 69

[Gao et al., 2017] Gao, M., Li, Q.-Z., Yan, X.-W., and Wang, J. (2017). Prediction of phonon-mediated superconductivity in borophene. *Phys. Rev. B*, 95:024505. 88

[Genovese et al., 2020] Genovese, C., Shirakawa, T., Nakano, K., and Sorella, S. (2020). General correlated geminal ansatz for electronic structure calculations: Exploiting pfaffians in place of determinants. *Journal of Chemical Theory and Computation*, 16(10):6114–6131. 62, 102, 108

[Giannozzi et al., 2017] Giannozzi, P., Andreussi, O., Brumme, T., Bunau, O., Nardelli, M. B., Calandra, M., Car, R., Cavazzoni, C., Ceresoli, D., Cococcioni, M., et al. (2017). Advanced capabilities for materials modelling with quantum espresso. *Journal of Physics: Condensed Matter*, 29(46):465901. 71, 88

[Giannozzi et al., 2009] Giannozzi, P., Baroni, S., Bonini, N., Calandra, M., Car, R., Cavazzoni, C., Ceresoli, D., Chiarotti, G. L., Cococcioni, M., Dabo, I., et al. (2009). Quantum espresso: a modular and open-source software project for quantum simulations of materials. *Journal of physics: Condensed matter*, 21(39):395502. 71, 88

[Gilbert, 1975] Gilbert, T. L. (1975). Hohenberg-kohn theorem for nonlocal external potentials. *Physical Review B*, 12(6):2111. 17

[Giustino, 2017a] Giustino, F. (2017a). Electron-phonon interactions from first principles. *Reviews of Modern Physics*, 89(1):015003. 31

[Giustino, 2017b] Giustino, F. (2017b). Electron-phonon interactions from first principles. *Rev. Mod. Phys.*, 89:015003. 73

[Gor'kov, 1959] Gor'kov, L. P. (1959). Microscopic derivation of the ginzburg-landau equations in the theory of superconductivity. *Sov. Phys. JETP*, 9(6):1364–1367. 8

[Graham, 1869] Graham, T. (1869). On the relation of hydrogen to palladium. *Proceedings of the Royal Society of London*, (17):212–220. 69

[Grimm and Storer, 1971] Grimm, R. and Storer, R. (1971). Monte-carlo solution of schrödinger's equation. *Journal of Computational Physics*, 7(1):134–156. 53

[Grimwall, 1980] Grimwall, G. (1980). The electron-phonon interaction in metals. 14

[Grosso and Parravicini, 2013] Grosso, G. and Parravicini, G. P. (2013). *Solid state physics*. Academic press. 15, 35

[Hamann et al., 1979] Hamann, D., Schlüter, M., and Chiang, C. (1979). Norm-conserving pseudopotentials. *Physical Review Letters*, 43(20):1494. 23

[Hellmann et al., 1937] Hellmann, H. et al. (1937). Einfuhrung in die quantenchemie. 28

[Hohenberg and Kohn, 1964] Hohenberg, P. and Kohn, W. (1964). Inhomogeneous electron gas. *Physical review*, 136(3B):B864. 16, 17

[Hou et al., 2021a] Hou, P., Belli, F., Bianco, R., and Errea, I. (2021a). Quantum anharmonic enhancement of superconductivity in p 63/mmc sch6 at high pressures: A first-principles study. *Journal of Applied Physics*, 130(17):175902. 79

[Hou et al., 2021b] Hou, P., Belli, F., Bianco, R., and Errea, I. (2021b). Strong anharmonic and quantum effects in p m 3^{-} n alh 3 under high pressure: A first-principles study. *Physical Review B*, 103(13):134305. 79

[Isihara, 1968] Isihara, A. (1968). The gibbs-bogoliubov inequality dagger. *Journal of Physics A: General Physics*, 1(5):539. 64

[Jiao et al., 2016] Jiao, Y., Ma, F., Bell, J., Bilic, A., and Du, A. (2016). Two-dimensional boron hydride sheets: High stability, massless dirac fermions, and excellent mechanical properties. *Angewandte Chemie*, 128(35):10448–10451. 88

[Kato, 1957] Kato, T. (1957). On the eigenfunctions of many-particle systems in quantum mechanics. *Communications on Pure and Applied Mathematics*, 10(2):151–177. 58

[Katsnelson and Fasolino, 2013] Katsnelson, M. I. and Fasolino, A. (2013). Graphene as a prototype crystalline membrane. *Accounts of chemical research*, 46(1):97–105. 93

[Kawamura et al., 2019] Kawamura, R., Cuong, N. T., Fujita, T., Ishibiki, R., Hirabayashi, T., Yamaguchi, A., Matsuda, I., Okada, S., Kondo, T., and Miyauchi, M. (2019). Photoinduced hydrogen release from hydrogen boride sheets. *Nature communications*, 10(1):1–8. 87, 92, 93, 99

[Kivelson and Chapman, 1983] Kivelson, S. and Chapman, O. (1983). Polyacene and a new class of quasi-one-dimensional conductors. *Physical Review B*, 28(12):7236. 3, 10

[Kleinman and Bylander, 1982] Kleinman, L. and Bylander, D. (1982). Efficacious form for model pseudopotentials. *Physical Review Letters*, 48(20):1425. 23

[Kohn and Sham, 1965] Kohn, W. and Sham, L. J. (1965). Self-consistent equations including exchange and correlation effects. *Physical review*, 140(4A):A1133. 19

[Kolesnikov et al., 1991] Kolesnikov, A., Natkaniec, I., Antonov, V., Belash, I., Fedotov, V., Krawczyk, J., Mayer, J., and Ponyatovsky, E. (1991). Neutron spectroscopy of mnh0. 86, nih1. 05, pdh0. 99 and harmonic behaviour of their optical phonons. *Physica B: Condensed Matter*, 174(1-4):257–261. 2, 9, 70

[Kong et al., 2021] Kong, P., Minkov, V. S., Kuzovnikov, M. A., Drozdov, A. P., Besedin, S. P., Mozaffari, S., Balicas, L., Balakirev, F. F., Prakapenka, V. B., Chariton, S., et al. (2021). Superconductivity up to 243 k in the yttrium-hydrogen system under high pressure. *Nature communications*, 12(1):1–9. 1, 8

[Landau and Ginzburg, 1950] Landau, L. D. and Ginzburg, V. L. (1950). On the theory of superconductivity. *Zh. Eksp. Teor. Fiz.*, 20:1064. 8

[Lewis, 1967] Lewis, F. A. (1967). The palladium/hydrogen system. 69

[Li et al., 2021] Li, Q., Kolluru, V. S. C., Rahn, M. S., Schwenker, E., Li, S., Hennig, R. G., Darancet, P., Chan, M. K., and Hersam, M. C. (2021). Synthesis of borophane polymorphs through hydrogenation of borophene. *Science*, 371(6534):1143–1148. 88

[London and London, 1935] London, F. and London, H. (1935). The electromagnetic equations of the supraconductor. *Proceedings of the Royal Society of London. Series A-Mathematical and Physical Sciences*, 149(866):71–88. 7

[Maxwell, 1950] Maxwell, E. (1950). Isotope effect in the superconductivity of mercury. *Physical Review*, 78(4):477. 8

[McLennan et al., 2008] McLennan, K., Gray, E. M., and Dobson, J. (2008). Deuterium occupation of tetrahedral sites in palladium. *Physical Review B*, 78(1):014104. 70, 85

[McMillan, 1968] McMillan, W. (1968). Transition temperature of strong-coupled superconductors. *Physical Review*, 167(2):331. 8, 33

[Meena et al., 2022] Meena, R., Li, G., and Casula, M. (2022). Ground-state properties of the narrowest zigzag graphene nanoribbon from quantum monte carlo and comparison with density functional theory. *The Journal of Chemical Physics*, 156(8):084112. 102

[Meissner and Ochsenfeld, 1933] Meissner, W. and Ochsenfeld, R. (1933). Ein neuer effekt bei eintritt der supraleitfähigkeit. *Naturwissenschaften*, 21(44):787–788. 7

[Methfessel and Paxton, 1989] Methfessel, M. and Paxton, A. T. (1989). High-precision sampling for brillouin-zone integration in metals. *Phys. Rev. B*, 40:3616–3621. 88

[Migdal, 1958] Migdal, A. (1958). Interaction between electrons and lattice vibrations in a normal metal. *Sov. Phys. JETP*, 7(6):996–1001. 8, 31

[Monacelli et al., 2021] Monacelli, L., Bianco, R., Cherubini, M., Calandra, M., Errea, I., and Mauri, F. (2021). The stochastic self-consistent harmonic approximation: calculating vibrational properties of materials with full quantum and anharmonic effects. *Journal of Physics: Condensed Matter*, 33(36):363001. 63

[Monacelli et al., 2018] Monacelli, L., Errea, I., Calandra, M., and Mauri, F. (2018). Pressure and stress tensor of complex anharmonic crystals within the stochastic self-consistent harmonic approximation. *Phys. Rev. B*, 98:024106. 79

[Monkhorst and Pack, 1976] Monkhorst, H. J. and Pack, J. D. (1976). Special points for brillouin-zone integrations. *Physical review B*, 13(12):5188. 22

[Mortazavi et al., 2018] Mortazavi, B., Makaremi, M., Shahrokhi, M., Raeisi, M., Singh, C. V., Rabczuk, T., and Pereira, L. F. C. (2018). Borophene hydride: a stiff 2d material with high thermal conductivity and attractive optical and electronic properties. *Nanoscale*, 10(8):3759–3768. 93

[Moskowitz et al., 1982] Moskowitz, J. W., Schmidt, K., Lee, M. A., and Kalos, M. H. (1982). A new look at correlation energy in atomic and molecular systems. ii. the application of the green's function monte carlo method to lih. *The Journal of chemical physics*, 77(1):349–355. 53

[Nagamatsu et al., 2001] Nagamatsu, J., Nakagawa, N., Muranaka, T., Zenitani, Y., and Akimitsu, J. (2001). Superconductivity at 39 k in magnesium diboride. *nature*, 410(6824):63–64. 3, 9, 87

[Nakano et al., 2020] Nakano, K., Attaccalite, C., Barborini, M., Capriotti, L., Casula, M., Coccia, E., Dagrada, M., Genovese, C., Luo, Y., Mazzola, G., et al. (2020). Turborvb: A many-body toolkit for ab initio electronic simulations by quantum monte carlo. *The Journal of Chemical Physics*, 152(20):204121. 103

[Nishino et al., 2017] Nishino, H., Fujita, T., Cuong, N. T., Tominaka, S., Miyauchi, M., Iimura, S., Hirata, A., Umezawa, N., Okada, S., Nishibori, E., Fujino, A., Fujimori, T., Ito, S.-i., Nakamura, J., Hosono, H., and Kondo, T. (2017). Formation and characterization of hydrogen boride sheets derived from mgb2 by cation exchange. *Journal of the American Chemical Society*, 139(39):13761–13769. PMID: 28926230. 3, 9, 87

[Parendo et al., 2006] Parendo, K. A., Tan, K. S. B., and Goldman, A. (2006). Electrostatic and parallel-magnetic-field tuned two-dimensional superconductor-insulator transitions. *Physical Review B*, 73(17):174527. 95

[Paulatto et al., 2015] Paulatto, L., Errea, I., Calandra, M., and Mauri, F. (2015). First-principles calculations of phonon frequencies, lifetimes, and spectral functions from weak to strong anharmonicity: The example of palladium hydrides. *Physical Review B*, 91(5):054304. 35

[Perdew et al., 1996] Perdew, J. P., Burke, K., and Ernzerhof, M. (1996). Generalized gradient approximation made simple. *Physical review letters*, 77(18):3865. 19, 71, 88

[Perdew and Wang, 1992] Perdew, J. P. and Wang, Y. (1992). Accurate and simple analytic representation of the electron-gas correlation energy. *Physical review B*, 45(23):13244. 20

[Pitt and Gray, 2003] Pitt, M. and Gray, E. M. (2003). Tetrahedral occupancy in the pd-d system observed by in situ neutron powder diffraction. *EPL (Europhysics Letters)*, 64(3):344. 70, 85

[Press et al., 2007] Press, W. H., Teukolsky, S. A., Vetterling, W. T., and Flannery, B. P. (2007). *Numerical recipes 3rd edition: The art of scientific computing*. Cambridge university press. 48

[Reynolds et al., 1950] Reynolds, C., Serin, B., Wright, W., and Nesbitt, L. (1950). Superconductivity of isotopes of mercury. *Physical Review*, 78(4):487. 8

[Reynolds et al., 1982] Reynolds, P. J., Ceperley, D. M., Alder, B. J., and Lester Jr, W. A. (1982). Fixed-node quantum monte carlo for moleculesa) b). *The Journal of Chemical Physics*, 77(11):5593–5603. 51, 53, 54

[Ross et al., 1998] Ross, D. K., Antonov, V. E., Bokhenkov, E. L., Kolesnikov, A. I., Ponyatovsky, E. G., and Tomkinson, J. (1998). Strong anisotropy in the

inelastic neutron scattering from pdh at high energy transfer. *Phys. Rev. B*, 58:2591–2595. 2, 9, 70

[Rowe et al., 1986] Rowe, J. M., Rush, J. J., Schirber, J. E., and Mintz, J. M. (1986). Isotope effects in the pdh system: Lattice dynamics of $pdt_{0.7}$. *Phys. Rev. Lett.*, 57(23):2955–2958. 2, 9, 70

[Rowe et al., 1974] Rowe, J. M., Rush, J. J., Smith, H. G., Mostoller, M., and Flotow, H. E. (1974). Lattice dynamics of a single crystal of $pdd_{0.63}$. *Phys. Rev. Lett.*, 33(21):1297–1300. 2, 9, 70

[Saito et al., 2015] Saito, Y., Kasahara, Y., Ye, J., Iwasa, Y., and Nojima, T. (2015). Metallic ground state in an ion-gated two-dimensional superconductor. *Science*, 350(6259):409–413. 96

[Saito et al., 2016] Saito, Y., Nojima, T., and Iwasa, Y. (2016). Highly crystalline 2d superconductors. *Nature Reviews Materials*, 2(1):1–18. 96

[Satterthwaite and Toepke, 1970] Satterthwaite, C. and Toepke, I. (1970). Superconductivity of hydrides and deuterides of thorium. *Physical Review Letters*, 25(11):741. 69

[Savini et al., 2010] Savini, G., Ferrari, A., and Giustino, F. (2010). First-principles prediction of doped graphane as a high-temperature electron-phonon superconductor. *Physical review letters*, 105(3):037002. 3, 9, 87

[Schirber et al., 1984] Schirber, J., Mintz, J., and Wall, W. (1984). Superconductivity of palladium tritide. *Solid state communications*, 52(10):837–838. 69, 71

[Schirber and Northrup, 1974] Schirber, J. E. and Northrup, C. J. M. (1974). Concentration dependence of the superconducting transition temperature in pdh_x and pdd_x. *Phys. Rev. B*, 10(9):3818–3820. 69, 71

[Semenok et al., 2020] Semenok, D. V., Troyan, I. A., Kvashnin, A. G., Ivanova, A. G., Hanfland, M., Sadakov, A. V., Sobolevskiy, O. A., Pervakov, K. S., Gavriliuk, A. G., Lyubutin, I. S., et al. (2020). Superconductivity at 253 k in lanthanum-yttrium ternary hydrides. *arXiv preprint arXiv:2012.04787*. 1, 8

[Sherman et al., 1977] Sherman, R., Birnbaum, H., Holy, J., and Klein, M. (1977). Raman studies of hydrogen vibrational modes in palladium. *Physics Letters A*, 62(5):353–355. 2, 9, 70

[Skoskiewicz, 1972] Skoskiewicz, T. (1972). Superconductivity in the palladium-hydrogen and palladium-nickel-hydrogen systems. *physica status solidi (a)*, 11(2):K123–K126. 69, 71

[Snider et al., 2021] Snider, E., Dasenbrock-Gammon, N., McBride, R., Wang, X., Meyers, N., Lawler, K. V., Zurek, E., Salamat, A., and Dias, R. P. (2021). Synthesis of yttrium superhydride superconductor with a transition temperature up to 262 k by catalytic hydrogenation at high pressures. *Phys. Rev. Lett.*, 126:117003. 1, 8

[Somayazulu et al., 2019] Somayazulu, M., Ahart, M., Mishra, A. K., Geballe, Z. M., Baldini, M., Meng, Y., Struzhkin, V. V., and Hemley, R. J. (2019). Evidence for superconductivity above 260 k in lanthanum superhydride at megabar pressures. *Physical Review Letters*, 122(2):027001. 1, 8

[Sorella, 2001] Sorella, S. (2001). Generalized lanczos algorithm for variational quantum monte carlo. *Physical Review B*, 64(2):024512. 48

[Sternheimer, 1954] Sternheimer, R. (1954). Electronic polarizabilities of ions from the hartree-fock wave functions. *Physical Review*, 96(4):951. 29

[Stritzker and Buckel, 1972a] Stritzker, B. and Buckel, W. (1972a). Superconductivity in the palladium-hydrogen and the palladium-deuterium systems. *Zeitschrift für Physik A Hadrons and nuclei*, 257(1):1–8. 69

[Stritzker and Buckel, 1972b] Stritzker, B. and Buckel, W. (1972b). Superconductivity in the palladium-hydrogen and the palladium-deuterium systems. *Zeitschrift fÃŒr Physik*, 257(1):1–8. 71

[Syed et al., 2016] Syed, H., Gould, T., Webb, C., and Gray, E. (2016). Superconductivity in palladium hydride and deuteride at 52-61 kelvin. *arXiv preprint arXiv:1608.01774*. 2, 9, 69, 70, 71, 83, 85

[Tateishi et al., 2019] Tateishi, I., Cuong, N., Moura, C., Cameau, M., Ishibiki, R., Fujino, A., Okada, S., Yamamoto, A., Araki, M., Ito, S., et al. (2019). Semimetallicity of free-standing hydrogenated monolayer boron from mgb 2. *Physical Review Materials*, 3(2):024004. 3, 9, 87, 88, 92, 93, 99

[Tominaka et al., 2020] Tominaka, S., Ishibiki, R., Fujino, A., Kawakami, K., Ohara, K., Masuda, T., Matsuda, I., Hosono, H., and Kondo, T. (2020). Geo-

metrical frustration of b-h bonds in layered hydrogen borides accessible by soft chemistry. *Chem*, 6(2):406–418. 92

[Tönshoff and Bettinger, 2021] Tönshoff, C. and Bettinger, H. F. (2021). Pushing the limits of acene chemistry: The recent surge of large acenes. *Chemistry–A European Journal*, 27(10):3193–3212. 101, 102

[Umrigar et al., 2007] Umrigar, C., Toulouse, J., Filippi, C., Sorella, S., and Hennig, R. G. (2007). Alleviation of the fermion-sign problem by optimization of many-body wave functions. *Physical review letters*, 98(11):110201. 45

[Umrigar et al., 1988] Umrigar, C., Wilson, K., and Wilkins, J. (1988). Optimized trial wave functions for quantum monte carlo calculations. *Physical Review Letters*, 60(17):1719. 45

[Van Delft and Kes, 2010] Van Delft, D. and Kes, P. (2010). The discovery of superconductivity. *Physics today*, 63(9):38–43. 7

[Vanderbilt, 1990] Vanderbilt, D. (1990). Soft self-consistent pseudopotentials in a generalized eigenvalue formalism. *Physical review B*, 41(11):7892. 24

[Waller, 1956] Waller, I. (1956). Dynamical theory of crystal lattices by m. born and k. huang. *Acta Crystallographica*, 9(10):837–838. 14

[Worsham Jr et al., 1957] Worsham Jr, J., Wilkinson, M., and Shull, C. (1957). Neutron-diffraction observations on the palladium-hydrogen and palladium-deuterium systems. *Journal of Physics and Chemistry of Solids*, 3(3-4):303–310. 2, 9, 70, 80

[Yildirim et al., 2001] Yildirim, T., Gülseren, O., Lynn, J. W., Brown, C. M., Udovic, T. J., Huang, Q., Rogado, N., Regan, K. A., Hayward, M. A., Slusky, J. S., He, T., Haas, M. K., Khalifah, P., Inumaru, K., and Cava, R. J. (2001). Giant anharmonicity and nonlinear electron-phonon coupling in mgb_2: A combined first-principles calculation and neutron scattering study. *Phys. Rev. Lett.*, 87:037001. 94

[Yussouff et al., 1995] Yussouff, M., Rao, B., and Jena, P. (1995). Reverse isotope effect on the superconductivity of pdh, pdd, and pdt. *Solid state communications*, 94(7):549–553. 2, 9